High Spin Spectroscopic Studies of ^{156}Ho: Shape Changes and Band Termination

Thesis submitted in accordance with the requirements of the
University of Liverpool for the degree of
Doctor of Philosophy

by

Peter Jeffrey Terence Hampson

2014

UNIVERSITY OF
LIVERPOOL

Abstract

High spin states in $^{156}_{67}Ho_{89}$ have been populated through the ^{124}Sn(^{37}Cl, 5n)^{156}Ho reaction at 177 MeV as part of an experiment performed at the ATLAS facility of Argonne National Laboratory. A high statistics, high-fold γ-ray coincidence data set was collected with the GAMMASPHERE spectrometer array.

Following a coincidence analysis 138 new transitions have been observed alongside a further 14 tentative transitions. A level scheme has been constructed building on previous work [1], which has been revised and considerably extended. A review of cranked shell model calculations, rotational alignments and B(M1)/B(E2) ratios of reduced transition probabilities has indicated that this nucleus is considerably soft with respect to triaxial deformation, which has facilitated in a reinterpretation of the configurations of four of the known bands.

A further four new band structures have been identified, three of which exhibit behaviour characteristic of terminating bands. Within these structures two terminating states have been identified and valence-space interpretations have been associated with them that are consistent with known terminating bands in neighbouring nuclei. A third terminating configuration has been proposed but a corresponding terminating state has not yet been observed.

An unusual backbend has been identified in a revised band structure. Following a review of nearby odd-odd nuclei it has been found that this behaviour may be systematic for odd-odd nuclei in the mass $\sim$160 region, however as of yet it defies a clear explanation, and therefore two possible interpretations have been presented.

"Sometimes, the best answer is a more interesting question."

The Science of Discworld

Terry Pratchett, Ian Stewart and Jack Cohen

Acknowledgements

While I can without refrain state that I am proud of having achieved this Doctorate, it is by no means something I completed alone. Along the way there have been many people who have encouraged and supported me, people to whom I am immeasurably grateful.

First and foremost, for all their incredible guidance and patience, I would like to thank Prof. John Simpson, Dr Eddie Paul and of course, my supervisor Prof. Paul Nolan. I would also like to thank the rest of the department staff as well as Peter Mason, James Ollier and Marc Labiche of Daresbury Laboratories for always having the time to help me through any problem I would approach them with.

My gratitude also goes to Aila Gengelbach and Prof. Johan Nyberg of Uppsala university for their kind hospitality and advice during the times we worked together.

Thanks to all the students in the department, as well as the postdocs, with whom I shared many good times throughout the years at the various experiments, conferences, classes and pubs that we travelled to along the way. I would like to especially acknowledge my fellow students of spin, Joe Rees and John Revill for helping prevent high-spin studies from making my head spin too much.

Further thanks to my close friends Daniel Cox, Joe McKenna, Peter Wigg, Richard Calland and Simon Leary who ensured that there never was a dull moment.

I thank my mother, father and sister, Kirsty for all the love, support and encouragement they have given me over the years, I could not have done it without you.

Finally, I am truly grateful to my long suffering wife, Christina for making it all so much easier.

Contents

List of Figures

LIST OF FIGURES

Chapter 1

Introduction

As with all of science, the history of nuclear physics is a testimony to the creative ingenuity of mankind. It may be said that the true beginning for this field was roughly 2400 years ago, when the Greek philosopher, Democritus, posed the question: *"If you break a piece of matter in half, and then break it in half again, how many breaks will you have to make before you can break it no further?"*. From this Democritus posited that there must come a point where matter can no longer be divided and one is left with the smallest possible pieces. As the Greek word for indivisible is *atomos*, he called these constituent pieces from which all matter is formed *"atoms"*. Unfortunately the atomic idea was deemed worthless by Aristotle and lost favour to his hypothesis that the nature of time, motion and space were that of a set of continua, and thus infinitely divisible.

It was to be more than 2000 years before Democritus's hypothesis would be vindicated. In the early 19th century the idea of atoms was brought back to life by the observations of John Dalton regarding the discrete nature of chemical reactions [19], marking the beginning of a shift in focus towards exploring the finite limits seen at the microscopic scale. By the early 20th century the foundations of what would become modern nuclear physics had been set down by discoveries [20][21][22] that revealed the quantal nature of the atom, showing each one to consist of a cloud of electrons in orbit about a tiny dense core, dubbed the atomic nucleus.

Today there are around 3000 nuclei that have been observed, and a further $\sim$4000 possible nuclei are estimated to exist. Of the known nuclei only $\sim$300 are stable.

Each of these nuclei may be described as an aggregation of two different types of fermions: protons and neutrons. They are typically denoted in the form ${}^{A}_{Z}X_{N}$ (or simply ${}^{A}X$) where X is the chemical element label, Z and N are respectively the number of protons and neutrons, and the mass number A is the sum of Z and N. The interplay of these nucleons presents a many-body problem which becomes exponentially more complex as more nucleons are added.

Such is the complexity of these systems that with the computational power currently available to us, a fully comprehensive "bottom up" approach is still not feasible for anything but the very lightest of nuclei. For heavier nuclei it is therefore necessary to employ models that describe the phenomena observed in terms that allow for significant simplifications to be made. In these models the behaviour of a nucleus is often expressed in terms of the collective macroscopic degrees of freedom experienced by the bulk of the nucleus and the individual motion of specific nucleons within that body.

The earliest of such models naturally sought to explain the properties observed in nuclei close to stability, as technological limitations restricted access to the short-lived isotopes far removed from stability. Over time the continuing improvements to accelerator and detector technology have pushed these boundaries back, revealing an astoundingly rich landscape where the addition of even a single proton or neutron can introduce large changes in the systematic behaviour of the nucleus.

It is this complex richness that makes understanding the nucleus such a fascinating challenge and currently no single model encapsulates the entirety of this enigma. Sometimes a model which performs wonderfully under certain conditions may no longer remain an accurate representation of the nucleus when those conditions change.

Therefore we continue to explore the nuclear system, often subjecting a nucleus to stresses and observing how the system changes with time. Under conditions such as extreme spin, mass or neutron excess new phenomena may emerge, phenomena radically different from the systematics seen on more familiar ground, and it is here the our models are most rigorously tested.

The chart of nuclides, also known as the Segrè chart, is a plot of Z against N for all the known nuclei, as shown in Fig. 1.1. The line of stability runs along

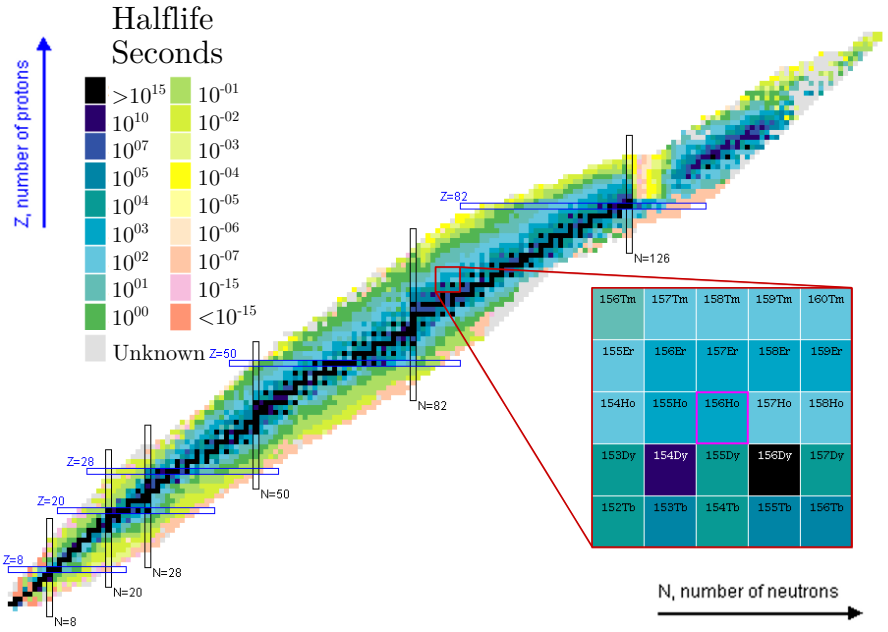

Figure 1.1: The Segrè chart [2] with the known nuclei differentiated in accordance to their halflives. ^{156}Ho, and those nuclei in the immediate vicinity of ^{156}Ho have been highlighted.

the black curve, with the heavier stable nuclei possessing a greater number of neutrons than protons, a result of the interplay between the short ranged nuclear force and the infinite ranged Coulomb force. As one proceeds away from the line of stability along an isotope or isotone chain, the stability of the nucleonic configurations lessen and the halflives decrease rapidly.

Marked on the Segrè chart are the so-called *"magic numbers"*, which correspond to multiples of protons or neutrons (when N or Z = 2, 8, 20, 28, 50, 82 and 126) where nuclei exhibits particularly high stability relative to those around them. These points were early proof of the underlying shell structure of these nuclei, and led to the development of the nuclear shell model. Akin to the atomic shell model, the magic numbers highlight the points of shell closure.

Finer variations in the observed stability of nuclei with differing Z and N may also be seen in the Segrè chart when tracing the pattern sketched out by the line of stability. Those nuclei with the longest halflives are found to almost always to be characterised by possession of even Z and N values. This trend is yet another indicator of the quantal nature of the nucleons within the nucleus, highlighting

the tendency of these nucleons to form into pairs. Due to these pairings nuclei that contain an even number of protons and neutrons are more tightly bound than those that do not, and thus are more stable.

As mentioned earlier, the behaviour of nuclei can change considerably with the addition of one or two more nucleons and the changes seen in the step from an even-even nucleus to an odd-odd nucleus are a fine example of this. One of the definitive traits of even-even nuclei is the so-called *pairing gap*, which corresponds to the energy required to break the first nucleon pair and excite these nuclei from their ground state. As a result even-even nuclei tend to possess a low number of discrete states at low spins. Conversely, because odd-odd nuclei do not require such a breaking of nucleon pairs, the level densities at low spins can be very high. This increased complexity, coupled to the rarity of odd-odd nuclei relative to even-even and even-odd nuclei has meant they have not been studied as much, and to date they remain poorly understood.

The focus of this thesis is one such nuclei, the odd-odd rare earth nucleus ^{156}Ho, which has been highlighted in Fig. 1.1. Following this introduction, the experimental methods used to produce and observe this nuclei shall be discussed in chapter 2. Chapter 3 will introduce the theoretical framework relevant to the interpretation of what is seen. In chapter 4 the results of the experiment have been documented and interpreted with concluding remarks given in chapter 5.

Chapter 2

Experimental methods

2.1 Introduction

There are many challenges to be faced in order to observe the form and behaviour of atomic nuclei. A nucleus' size alone prevents us from being able to observe it directly, necessitating the development of technologies and methods through which this hindrance can be overcome. A common means of achieving such endeavours is to seek to observe the manner in which a system changes when change is forced upon it. To that end in nuclear structure research, the use of accelerators such as the Argonne Tandem Linac Accelerator System (ATLAS) at Argonne National Laboratory have been crucial in providing a means of creating highly excited populations of nuclei through reactions between beam and target nuclides. The entropic decays back to the ground state of these newly formed and perturbed shortlived nuclei may be observed with advanced spectroscopic detector technology, giving us insights into the underlying systematics of the nucleons within as they interact with one another.
In this chapter the technologies and processes involved in such research shall be discussed.

2.2 Reaction Mechanisms

2.2.1 Fusion Evaporation

The reaction mechanism used in a study of high-spin states should be determined by how effectively it will produce large yields of the desired nuclei at the highest possible angular momentum. Desired qualities for which fusion-evaporation reactions have shown considerable success in achieving, albeit with certain limitations.

Traditionally, this process has involved the fusion of a stable beam ion and stable target nuclei to produce a new highly excited composite particle. The first challenge here lies in endowing enough energy to the accelerated ion to breach the Coulomb barrier of the target without being fully deflected by Coulomb repulsion before fusion takes place, with the Coulomb barrier being defined as

$$V_{Cb} = \frac{1}{4\pi\epsilon_0}\frac{Z_0 Z_1}{R}, \tag{2.1}$$

where ϵ_0 is the permittivity of free space, Z_0 and Z_1 are the atomic number of the beam and target nuclei, respectively and R is the interaction radius, best represented in the rare earth region by

$$R = [1.36(A_b^{1/3} + A_t^{1/3}) + 0.5]fm, \tag{2.2}$$

where A_b and A_t represent the atomic mass of the beam and target. Head on collision are unlikely as the repulsive Coulomb force between the beam and target isotopes will deflect the path of the incident beam ions away from the target nuclei. As such any compound nucleus formed from an interaction that takes place will in all likelihood be not only very hot, but also rapidly rotating with very high angular momentum. The magnitude of angular momentum acquired by the compound nucleus is dependent on the momentum of the beam ions and how far the collisions deviate from head on.

Following fusion the compound nucleus will seek to dissipate its energy. As the contributing energy from the beam ions is distributed between the angular momentum of the compound nucleus and the individual energies of the nucleons

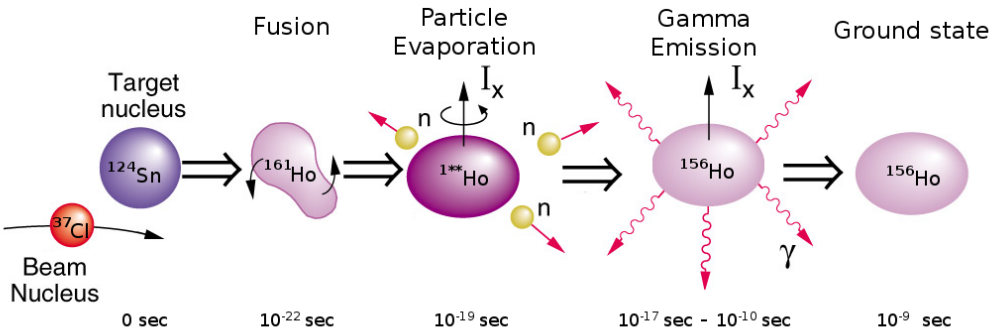

Figure 2.1: Diagram of the fusion evaporation sequence. Immediately following a collision the nucleus will be rapidly rotating and very hot. Particle evaporation reduces the initial excitation energy of the compound, leaving a residual nucleus that then proceeds to remove energy and angular momentum through the emission of γ-rays until the groundstate is reached.

within it, the first stage of decay often occurs through particle evaporation, whereby energy is carried away by neutrons, protons and α particles.
This evaporation occurs relatively quickly, within 10^{-19}s [23], and has been found to favour the emission of specific nucleons depending on the systematics of the initial nuclei involved. In the rare earth region the Coulomb barrier is sufficiently large as to greatly hinder the emission of charged particles. For this reason the majority of evaporating particles around A $\approx$ 160 will be neutrons. Each evaporating particle carries off a large amount of excitation energy but very little angular momentum, cooling the source nucleus considerably but leaving it with most of the initial post fusion angular momentum.
Once the excitation energy of the system is below that of the separation energy of a nucleon, de-excitation will continue via the emission of γ-radiation over the next 10^{-17}s to 10^{-9}s. Initially through this period of γ emission the overall excitation energy of the nucleus is still notably above the yrast states, which is to say that the nucleus still retains some heat. Due to this the first γ-rays emitted will be the so-called statistical γ-rays that make up the γ-ray continuum. Once enough energy has been released the states close to the yrast line are reached and decay begins to proceed through spin-stretched transitions between discrete states that are relatively few in number, in contrast to the cascade that came before.

It is this reduction of the available states and the resultant emergence of regular patterns in the energies of the radiation emitted from a population of excited nuclei that affords us the opportunity to study the underlying mechanisms at play in these nuclei through the methods that will be detailed later in this work. There is a limitation with respect to which compound nuclei can be produced through fusion-evaporation, imposed by the non-linear relationship between proton and neutron number for stable nuclei as one goes to higher mass regions, with lighter nuclei possessing a lower N/Z ratio than those of higher mass. As a result, the heavy compound nuclei tends to the neutron-deficient side of the valley of stability. This limitation is exacerbated by the highly favoured status of neutron evaporation over charged-particle emission in the rare earth region, further accentuating this neutron deficiency.

These factors make fusion evaporation an ideal method in the push to explore the properties of rare-earth nuclei that exist on the proton rich side of the valley of stability, however the need for stable beam and target chemical elements has limited these attempts to explore new unknowns. With the advent of radioactive beam facilities utilizing methods such as ISOL (isotope separation on line) and in-flight separation the opportunity to expand this exploration further has been vastly expanded.

2.2.2 Reaction Channels and Target Selection

Typically a principal objective in the experimental study of high-spin states is to generate substantial populations of the nuclei of interest and endow them with the highest achievable angular momentum. These goals largely dictate the combination of beam and target to be chosen, however it is important to consider additional factors that would have a detrimental effect on the desired population yields, such as the probability of fission. To facilitate in this choice statistical model calculations are popular.

Programs such as the Monte Carlo based PACE (Projected Angular momentum Coupled Evaporation) code [24], which is part of the LISE++ package, can be used to calculate expected cross-section values for fusion evaporation reactions across a range of beam energies, as demonstrated in Fig. 2.2. The computed

results presented in this figure are for the 3n, 4n and 5n reaction channels across a range of beam energies with a ^{37}Cl beam incident onto a self supporting ^{124}Sn thin target of 1.1 mg/cm^2 thickness.

Once within the target foil and prior to collision, the beam ions will typically experience a varying degree of deceleration from Coulomb interactions between the positively charged beam ions and the electrons surrounding the target nuclei. The highest population yields for Holmium isotopes can be seen for energies between ∼150 MeV and ∼170 MeV. From this, a beam energy of 177 MeV was chosen as a balance between optimum population and angular momentum yields. The reaction channels are typically denoted in the form ${}^{A_T}T({}^{A_B}B,xn\ yp\ z\alpha){}^{A_P}P$,

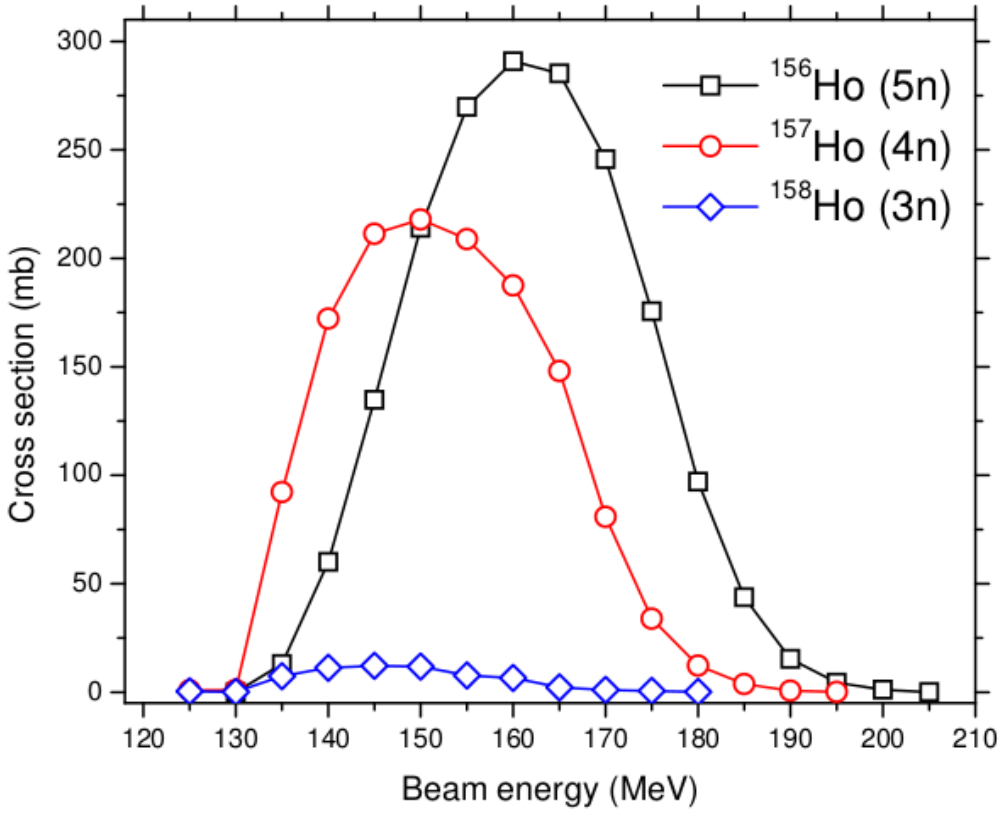

Figure 2.2: PACE calculations of cross sections as a function of beam energy for the 3n (blue diamond), 4n (red circle) and 5n (black square) channels of the reaction ^{124}Sn(^{37}Cl,xn). Reprinted from [3].

where ${}^{A_T}T$ and ${}^{A_B}B$ stand for the target and beam nuclei respectively, x, y and

z correspond to the number of neutrons, protons and/or α particles evaporated and ${}^{A_P}P$ represents the reaction product. The nucleus discussed in this work was populated through the ^{124}Sn(^{37}Cl, 5n)^{156}Ho channel.

Generally the targets used in these experiments tend to fall into one of two categories: thick targets and thin targets. With a thick target a thin foil of the target material is mounted on a backing of high-density material such as lead or gold ($\sim$10 mg/cm^2). The purpose of such a backing is to decelerate the recoiling nuclei and, if the rate of deceleration is known, can allow for the lifetime of a given state to be measured. Such backings do however invoke a necessity for caution with respect to the beam energy. Should the beam be of sufficient energy to overcome the Coulomb barrier of the backing material the recorded data will become contaminated.

For a thin target there is no backing material, and the target foil is instead self supporting within an aluminium frame. Here the fusion product will recoil into the vacuum with any Doppler shift incurred corrected for in the ensuing analysis. This is further discussed in section 2.3.9

2.3 Gamma Ray Detection

2.3.1 Interactions With Matter

Gamma-ray spectroscopy has been made possible through recognising how to exploit the various manners in which γ radiation transfers energy to another system. Principally there are three ways in which such a transference can take place [25]. The following section will briefly detail the nature of these interactions.

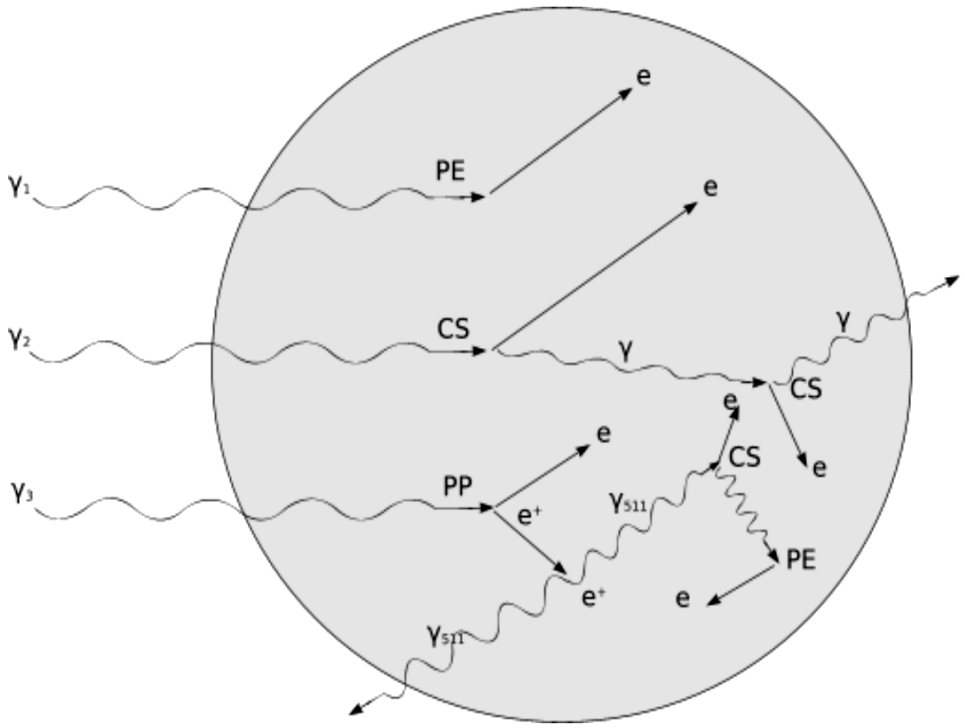

Figure 2.3: A representation of the three main modes of interaction between photons and matter. In this diagram PE is the photoelectric effect, CS is Compton scattering and PP is pair production. Reprinted from [4].

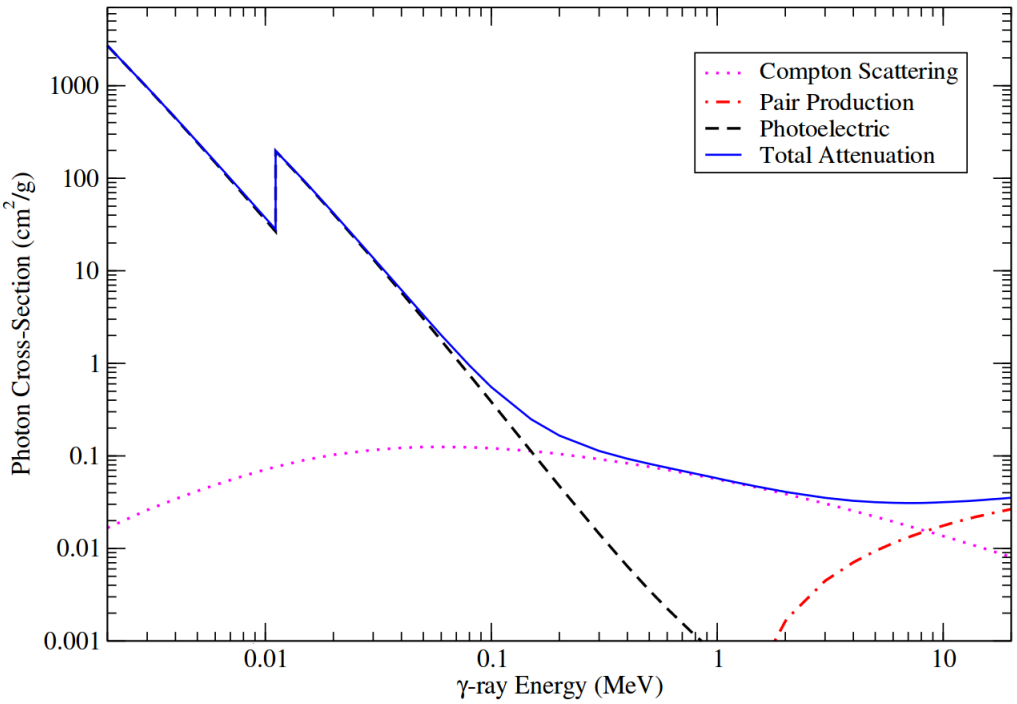

Figure 2.4: Mass attenuation as a function of photon energy for Germanium. Reprinted from [5].

2.3.2 The Photoelectric Effect

The photoelectric effect is dominant throughout the relatively low energy range below ~200 keV. Should the energy carried by a photon incident on a bound atomic electron exceed a certain *threshold frequency*, which is defined by the properties of the material, then this photon may be absorbed and it's energy transferred to the electron. This electron will then eject from its orbital with a kinetic energy given by the relation

$$KE_{electron} \approx h\upsilon - \phi, \tag{2.3}$$

where $h\upsilon$ is the energy carried by the photon and ϕ is the energy required to free an electron from its orbit, also known as it's *binding energy*.

The kinetic energy of this ejected electron (now labelled a *photo-electron*) will disperse into the surrounding material through Coulomb interactions with other

bound electrons, which may also be liberated from their respective atoms. The yield of the resultant cascade of electrons (known as *charge-carriers* [4] [5]) is a material dependent property important to the energy resolution of a detector and will be discussed further in section 2.3.5.
Following the ejection of an electron, the atom from which it was ejected will be left in an excited state and naturally will seek to remove the excess energy. It is possible for this to take place through an electron from a higher energy orbital dropping into the orbital previously occupied by the ejected photo-electron, in the process emitting an X-ray photon. This is known as X-ray fluorescence [5].
In all likelihood the emitted X-ray will be reabsorbed by the material, producing another photo-electron that goes on to contribute to the overall charge gathered, however in the event that the X-ray escapes the detecting medium the measured energy of the initial γ-ray will be slightly reduced.
As can be seen in figure 2.4, where the cross sections for the various interactions of EM radiation with Ge are depicted as a function of γ energy, E_γ, the probability of the photoelectric effect taking place rapidly decreases as E_γ increases and is superseded at $\sim$200 keV by Compton scattering as the dominant mode of interaction. The process has been found to also depend on the atomic number Z, with the probability of the photoelectric effect taking place at a certain energy increasing as Z goes to higher values.

2.3.3 Compton Scattering

Much as with the photo-electric effect, Compton scattering involves the ejection of an electron from it's atomic orbit, however only part of the photons energy is absorbed in the process with the remainder carried off by the scattered photon (γ') whose energy E'_γ is given by the relation

$$E'_\gamma = \frac{E_\gamma}{(1 + \frac{E\gamma}{m_0 c^2}(1 - cos\theta)}, \tag{2.4}$$

where E_γ represents the energy of the the incident photon, $m_0 c^2$ is the rest mass energy of the electron, 0.511 MeV, and θ is the scattering angle.

The energy of the ejected electron is simply

$$E_e = E_\gamma - E'_\gamma. \tag{2.5}$$

A scattered photon may go on to scatter again or even be fully absorbed through the photoelectric effect, in which case the full energy of the γ-ray will be recorded, however it is also very possible that the scattered photon will escape the detecting medium. Such partial depositions are troublesome since only the recoil energy will be recorded leaving an inaccurate representation of the full energy of the γ-ray it interacted with.
As the strength of the interaction is heavily dependent on the scattering angle the energy recorded in the event of a photon scattering out of the detector can vary greatly. This results in a continuum of background noise (The so-called *Compton continuum*) throughout the recorded spectra.
Compton scattering remains the dominant interaction mode across ∼200 keV to 7 MeV, which covers the intermediate γ-ray energies expected to be well represented in the emissions of a decaying nucleus. Due to this the accumulation of departing scattered photons can have a considerable impact on the quality of the data collected. This has led to the development of Compton suppression shields, which are detailed in section 2.3.7.

2.3.4 Pair Production

The third major form of interaction for γ radiation, this process is known to occur within the field of a nucleus where the photons energy may be converted into a positron-electron pair. Pair production can only take place when the energy carried by the photon exceeds the combined rest energy of a positron electron pair (1.022 MeV). Any energy carried by the photon in excess of this is divided between the positron and electron as kinetic energy thus

$$E_e^{kin} + E_p^{kin} \approx E_\gamma - 2m_0c^2, \tag{2.6}$$

where E_e^{kin} and E_p^{kin} are the kinetic energy of the electron and positron, respectively, E_γ is the energy of the absorbed photon and m_0c^2 is the rest energy of the

electron and positron.

The two emitted particles will subsequently deposit their excess kinetic energy into the surrounding medium. In the case of the electron this proceeds exactly as with any other photo-electron, however the situation for the positron is a little more complicated. Once the total energy of the positron has cooled to close to it's rest energy it will annihilate with a nearby electron, converting all of the mass into two 511 keV γ-ray photons emitted in opposing directions. Depending on the size and shape of the detector, as well as the point at which the annihilation event occurred, there is a probability one or both of these photons may escape the medium rather than be absorbed. If both are absorbed then, owing to the relatively short time scale in which the above process takes place, the full energy of the initial γ-ray prior to pair production is accurately recorded. However, as with Compton scattering, each photon that escapes the detecting medium will lead to an inaccurately recorded γ-ray energy. In this case the departing photons will each carry off 0.511 MeV, potentially leading to relatively small single and double escape peaks at 0.511 MeV and 1.022 MeV below significantly represented full energy photopeaks, contaminating the spectra.

2.3.5 Semiconductor Detector Principles

Certain semiconducting materials, such as germanium (Ge) and silicon (Si) have been found to possess excellent energy resolution for the purpose of γ-ray spectroscopy, making them a valuable tool in the pursuit of charting the sometimes profoundly finite distinctions found within the atomic nucleus.
Towards understanding why this is the case, it is helpful to consider the description put forward in the band gap theory [26] [5]. In this formalism the conductive properties of a material are defined through separating the states of the electrons in that material into two bands; the conduction band and the valence band. The so-called *forbidden zone*, also known as the electrical band gap in this case, is the difference in energy between the two. An idealised representation of the band gap theory is shown in figure 2.5.

The magnitude of this energy gap (E_g) can be a defining difference between

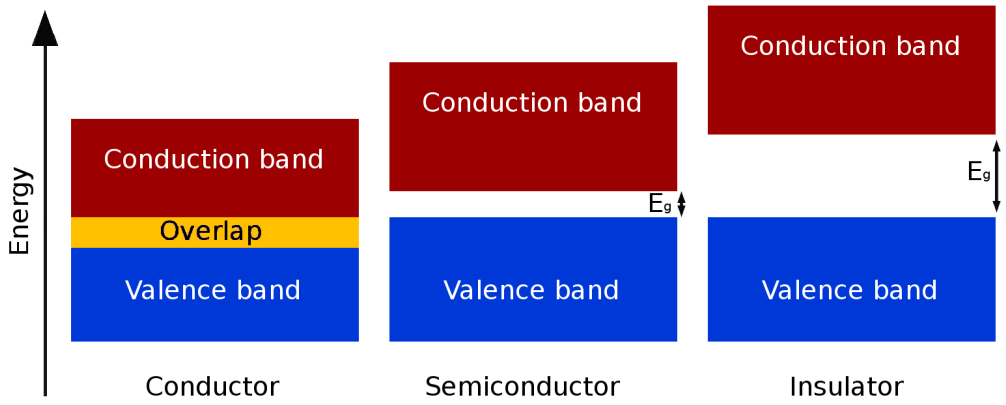

Figure 2.5: Idealised representation of the band gap for the individual material categories, E_g is the energy gap across which an electron must travel to reach the neighbouring band.

insulators, semiconductors and conductors where typical values of E_g for an insulator may be ∼5eV as opposed to ∼1eV (∼0.7eV for Ge) for a semiconductor. Recalling that an ejected photo-electron will carry an energy excess which will disperse into the surrounding medium through Coulomb interactions with other electrons, a single photo-electron will often lead to a cascade of charge carriers. The relationship between the energy gap and the charge carrier yield of a material

is dependent on E_g; the larger the gap the greater the energy necessary for an electron to excite into the conduction band. This relationship may be described in terms of an electric pulse generated by the cascade of a number of electrons, n, that become unbound

$$n \propto \frac{E_{abs}}{\phi}, \tag{2.7}$$

where E_{abs} is the photon energy absorbed by the first electron to be ejected and ϕ is the energy required to liberate an electron from its atomic orbit (2.96eV for Ge), which is directly related to the materials band gap.

As a reduction in the quantity of charge carriers will increase the magnitude of statistical fluctuations in the recorded energy, a material with a large band gap will inevitably exhibit poorer energy resolution than one that possess a small band gap. Therefore, at least "on paper" so to speak, it is desirable to achieve as small a band gap as possible. However as E_g is reduced the problem of thermal ionisation will become increasingly pronounced, with the temperature dependence of a material defined by the ratio of the band gap to the temperature, with the probability per unit time of an electron thermally exciting across the band gap into the conduction band given by

$$P(T) \propto T^{3/2} e^{(E_g/2k}$$

$_b$T), (2.8)

where k_b is the Boltzmann constant and T is the absolute temperature.

As the temperature rises an increasing number of electrons will migrate from the valence band to the conduction band, leading to a background of thermal noise in the collected data. So in the interest of spectroscopic fidelity detectors made from materials with a low E_g detectors will need to be operated at a low temperature. The clarity of the recorded data can be further improved by deliberately adding impurities to the crystal in a process known as doping. There are two types of doping available; n-type (donors) and p-type (acceptors).

As an example of this: Germanium and silicon are valence 4 elements, aka quadrivalent crystals, with each atom sharing four electrons with their neighbouring

atoms. When another element of a different valence group is integrated into the crystal formation there will be an imbalance in the shared electrons as shown in figure 2.6, where a representation of the covalent bonds between silicon and two doping elements is displayed. In (a) the silicon has been doped with arsenic, a pentavalent element which in this instance represents an n-type dopant, and in (b) the silicon has received p-type doping with boron, a tetravalent element [26]. In example (a) the five covalently available electrons around an arsenic atom are shared with the surrounding silicon, leaving one electron bound to the As atom only. This weakly bound electron can be described as occupying an energy state just below the conduction band edge. Conversely for (b) the electron hole formed by the relative valence electron deficiency in boron will occupy an energy level just above the valence band edge, allowing for easier excitation of the electrons in the valence band.

Since doping introduces active energy states within the forbidden band gap,

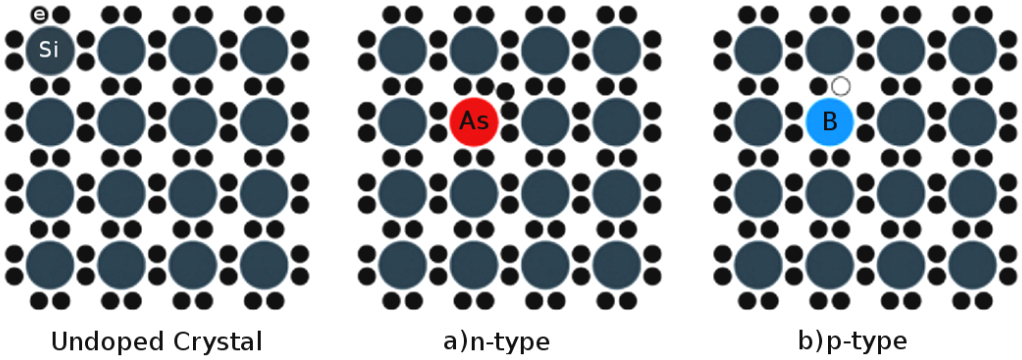

Figure 2.6: A simple depiction of the concept of doping in a silicon lattice. Each small black dot represents an electron within the lattice. In a) n-type silicon doping with Arsenic is shown with an additional electron attached to the impurity. For b) p-type silicon doping with boron is shown. In this case there is an electron vacancy (or *hole*).

the temperature required for thermal ionisation in a crystal permeated with such dopants is further reduced. As a result thermal excitation in doped Ge can easily happen even at temperatures as low as 77K, necessitating the use of coolants such as liquid nitrogen to maintain an operational temperature.

Despite this, the benefit of doping a material is made apparent when n-type

and p-type materials are brought into contact with one another creating what is known as a p-n junction. The weakly bound donor electrons of the n-type material will move to the electron holes of the p-type material, leaving the n-type partially ionized (negatively charged) near the boundary and the p-type with an electron surplus (positively charged). This build up of ions (depicted in Fig. 2.7) introduces a repulsive Coulomb force at the junction that will grow until the repulsion is strong enough to prevent any further electron migrations between the materials. At this point the material is functioning as a diode in a reverse-bias mode with a depletion region within the medium where no free charge carriers exist while the system remains unperturbed.

By applying a forward voltage bias across the junction the electrons can be assisted in overcoming the Coulomb barrier in the depletion region and a current will flow. Conversely, applying a reverse bias will drive the electrons away from the junction, increasing the physical volume of the depletion region and thereby expanding the charge carrier free zone ideal for the detection of gamma rays. The thickness of this region is given by the relation

$$d \approx \sqrt{\frac{2\epsilon V}{eN}}, \tag{2.9}$$

where ϵ is the dielectric constant of of the material, V is the bias voltage, $e = 1.6\text{x}10^{-19}\text{C}$ and N is the dopant concentration.

Ideally the depletion region should be large enough to allow for absorption of the γ-rays that travel through it. In other words, greater than the mean free path of the photons. A γ-rays mean free path in a medium is dependent on the initial energy of the photon and the atomic number of the material the photon is travelling through. For Si and Ge the mean free path of photons possessing energies typical for γ-rays emitted from a decaying nucleus can be of the order of several cm, as shown in figure 2.8.

While there are many geometries that may be produced, for the purpose of this work the coxial form is most relevant. Depicted in figure 2.9, this form often consists of a cylindrical detector medium with a partially hollowed core. The example in the diagram is that of a mildly n-type doped Ge crystal as used in the Gammasphere array [27]. The crystal is coated internally with a layer of heavily

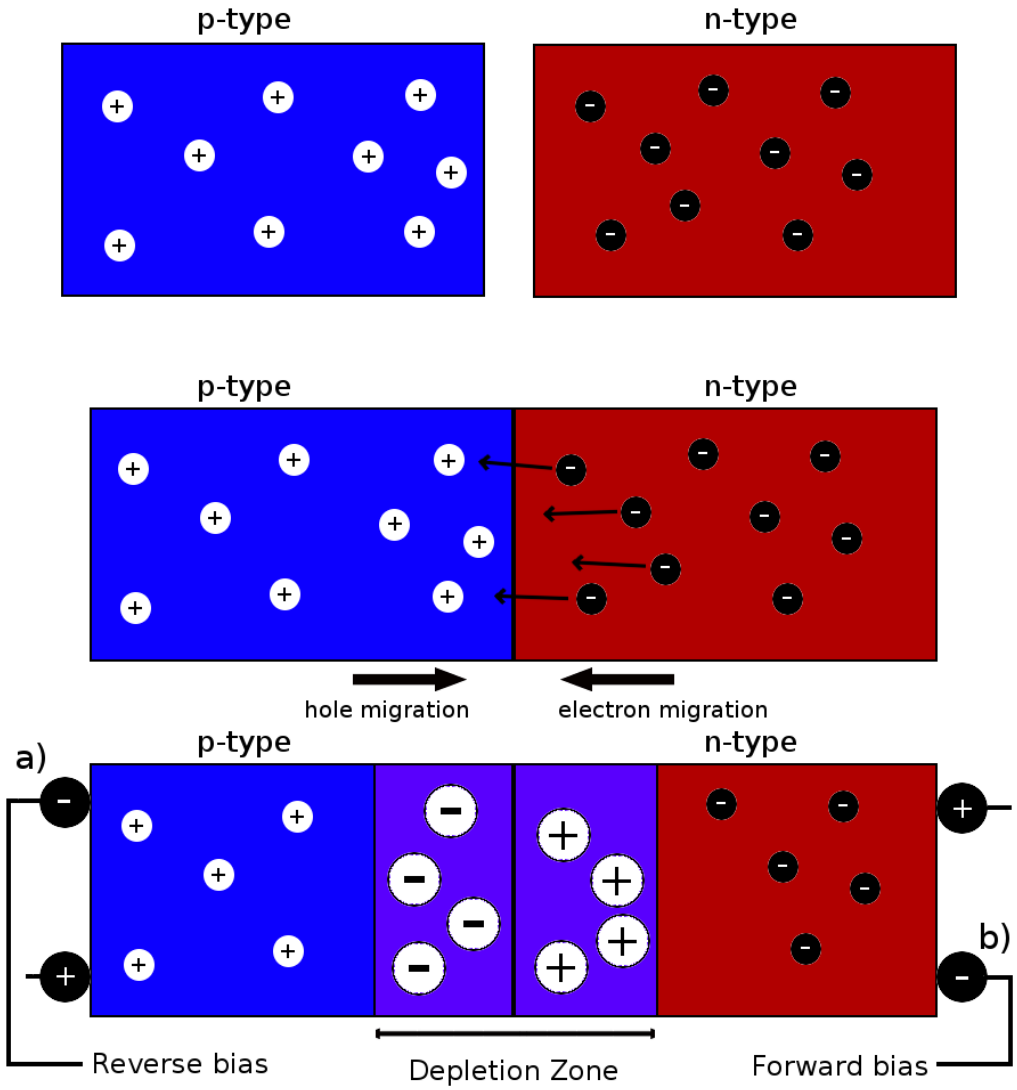

Figure 2.7: Top: p-type and n-type materials with an excess of positive and negative charge respectively. Middle: When brought into contact electrons will migrate from the n-type to the acceptor holes of the p-type material. Bottom: The build up of positive and negative charge forms a depletion zone around the point of contact.

n-type doped material, dubbed an n+ contact and externally with an opposing p+ contact. This geometry has been found to be ideal for generating as large a physical volume for the depletion zone as possible, thereby maximising the likelihood of absorption of an photon.

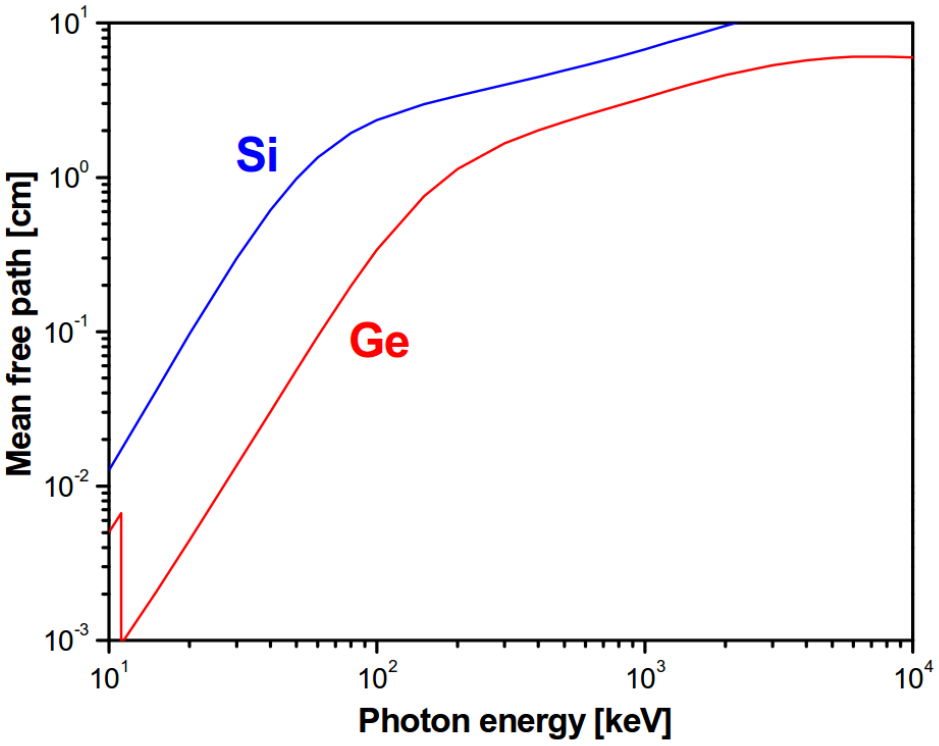

Figure 2.8: Mean free path as a function of photon energy for silicon and germanium. Reprinted from [6].

Often the energy dependent nature of the γ-ray mean free path and the different modes of interaction that take place is simply expressed in terms of the detectors efficiency.

This simplification of the energy dependence of the material allows for easy corrections to the relative measured intensities of the photopeaks, a necessary accommodation for certain analysis techniques. To this end an efficiency calibration is almost invariably performed for each experiment using radioactive sources for which the energies and intensities of the emitted γ-rays are well known.

The intensities that are recorded for these γ-rays may then be normalised and fitted to an efficiency curve in order to extract a empirically derived expression of the detectors efficiency, $\epsilon(E_\gamma)$, which is described through the relation

$$\epsilon(E_\gamma) = e^{[(A+Bx+Cx^2)^{-G}+(D+Ey+Fy^2)^{-G}]^{-1/G}}, \tag{2.10}$$

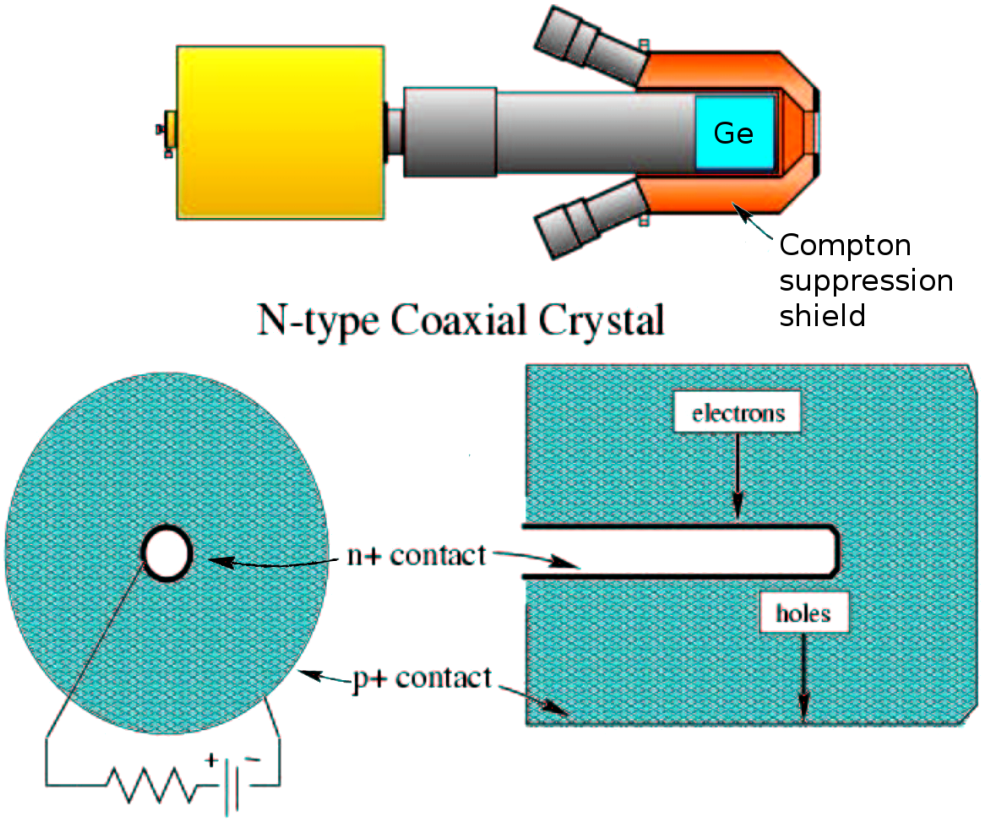

Figure 2.9: Plot of the mean free path as a function of photon energy for silicon and germanium. Reprinted from [7].

where A, B and C describe the low energy efficiency, D, E and F describe the efficiency at high energies, $x = ln(E_\gamma/100)$, $y = ln(E_\gamma/1000)$ and G is the interaction parameter between the low and high energy regions.
Fig. 2.10 shows the fitted calibration curve for the GAMMASPHERE array, where the sources ^{56}Co, ^{152}Eu, ^{182}Ta and ^{243}Am were used to obtain a broad spread of energies against which to perform the fit.

2.3.6 Scintillation Detectors

Another group of solid state detectors which see common use in modern day nuclear structure experiments are scintillation detectors. Unlike semiconductors, with which we relate the absorbed γ radiation directly to the electric current

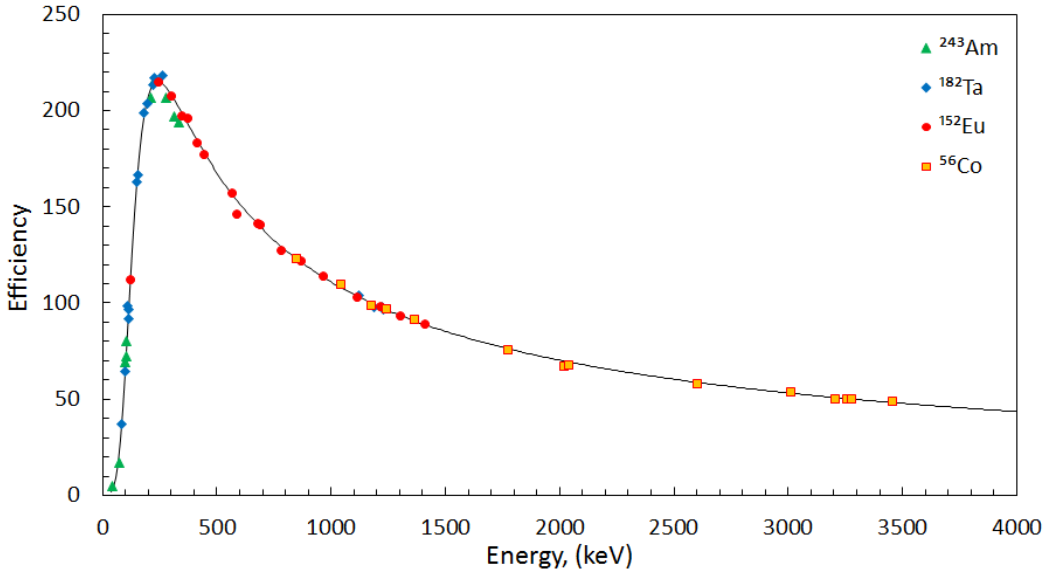

Figure 2.10: Fitted efficiency curve for the GAMMASPHERE detector array.

produced by the γ-ray, scintillation detectors function on the property of *luminescence*, whereby the energy from ionizing radiation absorbed by the material is released in the form of light [5]. In terms of a materials band structure, after a cascade of electrons have been excited from the valence band to the conduction band by the absorption of a γ-ray there is a chance that some of the excited electrons will de-excite back down to the valence band, in the process emitting the energy they were carrying in the form of a photon of light.

The light emitted by the scintillation material is often then converted back into an electric current through a *photomultiplier tube* (PMT), within which a photoelectron induced from a photocathode is multiplied and shaped into an output electric signal that possesses an amplitude proportional to the γ-ray energy.

An advantage to scintillation detectors over semiconducting detectors lies in the availability of relatively high Z materials that may be used in this capacity. As a high Z reduces the mean free path of a photon within a material, detectors formed from high Z materials are more efficient. So while these detectors do not possess the high energy resolution of Ge, with typical energy required to liberate a photoelectron in a scintillation detector being $\sim$250 eV as compared with $\sim$3 eV for germanium, they can be useful in a situation where only detector efficiency

matters. For this reason scintillation detectors are often in conjunction with Ge detectors as Compton suppression shields.

2.3.7 Compton Suppression

As noted earlier in this work, for a detector of only a few centimeters radius and depth Compton scattering can be a troublesome problem. Given the typical meanfree path for a photon at these scales (Fig. 2.8) a considerable percentage of scattered photons will escape the detector medium.

To help reduce the detrimental effect this loss will have on the quality of the recorded data it is useful to have a means of removing any such partially recorded events. To this end Compton suppression shields were devised. Such shields are themselves guard detectors designed to function as ancillary to a primary detector. When a photon event is recorded in the guard detector any coinciding event recorded by the corresponding principle detector is vetoed electronically. Ideal qualities for a guard detector are a high detection efficiency to capture the escaped photons and a small size to minimise the impact on the net array efficiency [5].

The first such suppression shields used were the Sodium Iodide (NaI) scintillation detectors of the TESSA array. While NaI provided considerable improvements to the quality of γ spectroscopy, the usage of the NaI for suppression shielding later lost favour to Bismuth Germanate (BGO). The mean free path within BGO detectors is much shorter due to their greater density (7.13g/cc as opposed to 3.67g/cc) and greater average Z number. This allows for a smaller detector to achieve the same detection efficiency.

The scattering probabilities of the γ-rays tends to favour forward scatters [28][5] with little energy loss, furthermore the photons that do backscatter will possess a lower relative energy. As such, the need for efficiency is greater in the forward position than backwards since the higher energy of the forward scattered photons will result in a higher mean free path. This need is catered for by increasing the physical volume at these points, as shown in the cross section slice of a GAMMASPHERE detector seen in figure 2.11.

Figure 2.11: Cross slice of detectors from the GAMMASPHERE array. Reprinted from ref.[8].

2.3.8 GAMMASPHERE Spectrometer

The GAMMASPHERE array (Shown in Fig. 2.12) has been a fantastic asset in the quest to expand our understanding of the basic building blocks of existence. Composed of 110 Compton suppressed high-purity Germanium (HPGe) detectors, each measuring 7 cm in diameter and 7.5 cm in length, the array covers 46% of

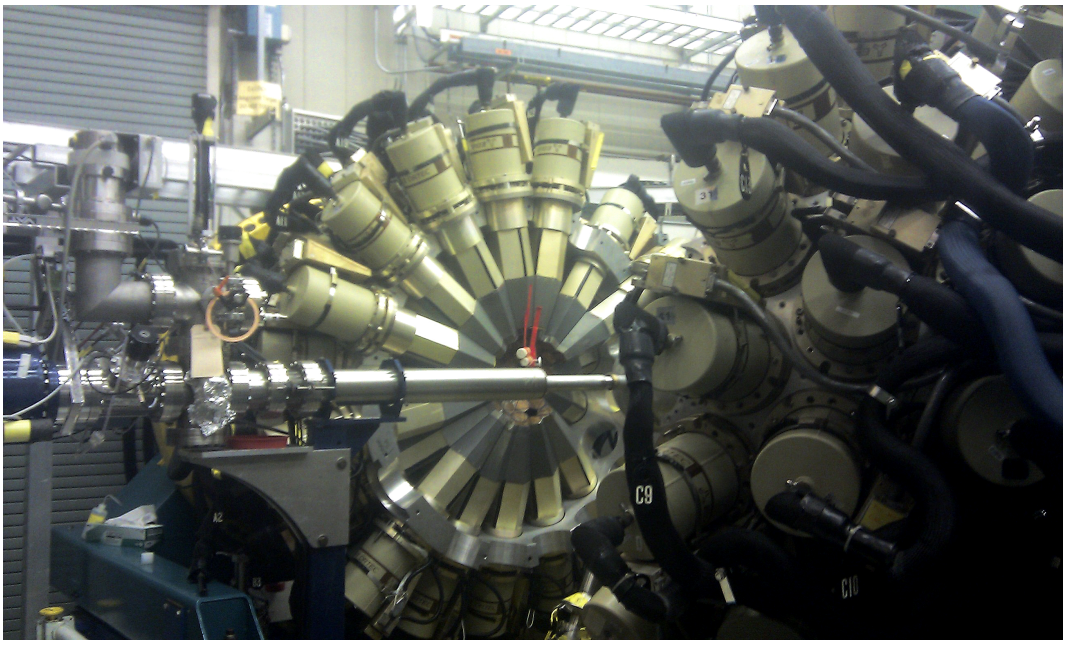

Figure 2.12: The opened GAMMASPHERE array.

4π and is structured such that the detectors point radially inwards, encasing the reaction chamber set into the beamline. The segmentation of the inner sphere is broken down into the form of a polyhedron with 122 elements comprising 110 hexagonal and 12 pentagonal faces [27].

Given this structured arrangement, the detectors may be effectively divided into 17 'rings' allowing for the separation of what is observed into independent spectra consisting of only what is seen at a given angle. These angles of observation are at 17.3°, 31.7°, 37.4°, 50.1°, 58.3°, 69.8°, 79.2°, 80.7°, 90.0°, 99.3°, 100.8°, 110.2°, 121.7°, 129.9°, 142.6°, 148.3°, 162.7° about an axis perpendicular to the beam direction. Being able to divide the array in this manner thus provides the opportunity to determine the multipolarity of the emitted γ radiation, which is useful in the modeling of the underlying structure to a nucleus as will be detailed in section 2.4.2.

The ring at 17.3° was not available throughout the GSFMA269 experiment as it had been removed to provide room for the Fragment Mass Analyzer (FMA). This reduced the total number of detectors utilized in the array to 101, giving a diminished coverage of 42% of 4π.

2.3.9 Doppler Correction

As the targets for experiment GSFMA269 were thin self supporting foils, the post-fusion products were not stopped in a backing medium prior to the final stage of de-excitation and instead were still travelling through the vacuum at 2% of c during this period of time. Due to this the emitted γ-rays will be Doppler shifted, resulting in an angular dependence on the energies recorded given by the relation

$$E'_\gamma = E_\gamma(1 + \beta cos\theta), \tag{2.11}$$

where E'_γ is the measured energy, E_γ is the unshifted energy of the emitted photon, β is the velocity of the recoiling nucleus relative to the speed of light (v/c) and θ is the angle that the γ-ray is emitted relative to the direction in which the nucleus of origin is travelling.
Clearly the detectors in the forward direction of the moving nucleus will observe photons that are shifted to higher energies and vice versa for detectors in the backward direction. This was rectified using the known angles of the GAMMASPHERE rings. Prior to the sorting and analysis of the data unmodified spectra of what was observed at each ring were produced and a value for β ($\beta = 0.0206$) was extracted by comparing the energy positioning of photopeaks corresponding to a given decay transition. This value was then used to correct the energies to what was seen at the 90° angle.

2.4 Coincidence Data Collection

The short timescale for the radiative cascades of γ-rays emitted by a decaying nucleus relative to the typical time resolution of HPGe detectors (10^{-8} s) [6] means that the de-excitations of a nucleus is effectively observed as a single flash of emitted radiation. With a single detector the accumulated statistics will produce what is known as a *singles spectrum*, with which it is not possible to deduce much about the how the excited states of the nucleus relate to one another. However with the addition of more detectors the many transitions emitted during the "flash" can begin to be meaningfully distinguished through prompt coincidence. Photon absorptions that take place in multiple detectors about a reaction point

within a certain time-gate (∼70 ns for GSFMA269) are treated as a single event, with the number of γ-rays detected in that time window known as the events *fold*. For example, five detectors firing in coincidence would be a fold = 5 event. Such coincidental detection events are likely to involve information from only a single nucleus as it decays to the ground state. Still, overlaps between two or more nuclei decaying at the same time do occur. This is not uncommon and will lead to unwanted background in the form of random coincidences.
On top of this the existence of long lived states can make association between a perceived band structure and it's specific nuclei of origin difficult as the longer decay time for these states will prevent them from being observed within the same time-gate as other decays from that nucleus.

2.4.1 Offline Analysis

Owing to the magnitude of coincidence data generated in these experiments and the complex manner in which the quantum states of the nuclear system proceeds to high excitation energies, it is helpful to sort the data into an analysis friendly structure that is easily manipulated. One of the more basic of these formats is that of a two dimensional histogram known as a matrix. The manner in which this works can be easily understood by considering the simplest scenario of a two detector setup (A maximum of two fold events). Each event will involve a pair of recorded energies; E_γ^1 and E_γ^2 for detectors one and two respectively. This relation allows us to plot coincidence spectra against E_γ for both detectors simultaneously. By setting a energy window (known as a *gate* or a *slice*) on a photopeak seen in the E_γ^1 spectrum (x-axis) we can project every E_γ^2 value that was seen in coincidence with the events encased by the gate set on E_γ^1 as a one dimensional histogram on the y-axis.
With the addition of more detectors and higher fold events this process can be extended to three or four dimensions (known as *cubes* and *hypercubes* respectively), allowing for projections from gates set on two or even three axis. Doing so improves discrimination against random coincidences and thus allows for a greater degree of certainty in the relationships between transitions. However, each further gate will greatly reduce the net statistical output in the projected

spectrum. It is down to the analyst to determine the optimum balance between discrimination and statistical yield.

In a manner not unlike solving a jigsaw puzzle, the appearances and disappearances of photopeaks in the projected spectra from sequences of gates are used to piece together a level scheme, from which a great deal of useful information about the nucleus can be gleaned. To provide an example of this four triple gate spectra of transitions in bands 1a, 1b, 2a and 2b alongside the portion of the level scheme corresponding to these bands have been presented in figure 2.13. Each state may decay to another state via one or more transitions which may involve the emission of a γ-ray with energy $E\gamma$, depicted in the decay scheme as an energy value in keV.

In the case of a state that decays to multiple other states via γ transitions, setting a gate on one of these transitions will block the appearance of the others in the projected coincidence spectra. With each set of triple gates the spectra produced contributes a little more to the story of how the excitation levels relate.

The relative intensities of the photopeaks provides a parallel criterion with which to determine the placement of transitions in the level scheme. Towards the groundstate the number of available levels will decrease, reducing the feeding to fewer and fewer states, and as a result the intensities of the photopeaks will increase. This trend is ideal for identifying transitions connecting to states directly above those joined by the transition gated on as opposed to those below. This is because those that are below are decaying out towards a ground state along a path defined by the coincidence gate set, and as a result the intensities of those transitions between lower excitation energy states will be relatively large. Conversely for the states at higher excitation energies there will still be a number of decay paths feeding into the levels of the gated transition, and so the intensities will be lower.

For the purpose of generating and analyzing these multidimensional structures, the RADWARE [29][30] graphical analysis package, designed by D.C. Radford, is a favoured tool and was utilized for the analysis of the data on ^{156}Ho. The RADWARE codes for matrices, cubes and hypercubes are respectively named ESCL8R, LEVIT8R and 4DG8R. For experiment GSFMA269 a hypercube was generated by Joe Rees using 4DG8R [9] for a sister analysis into ^{155}Ho using the

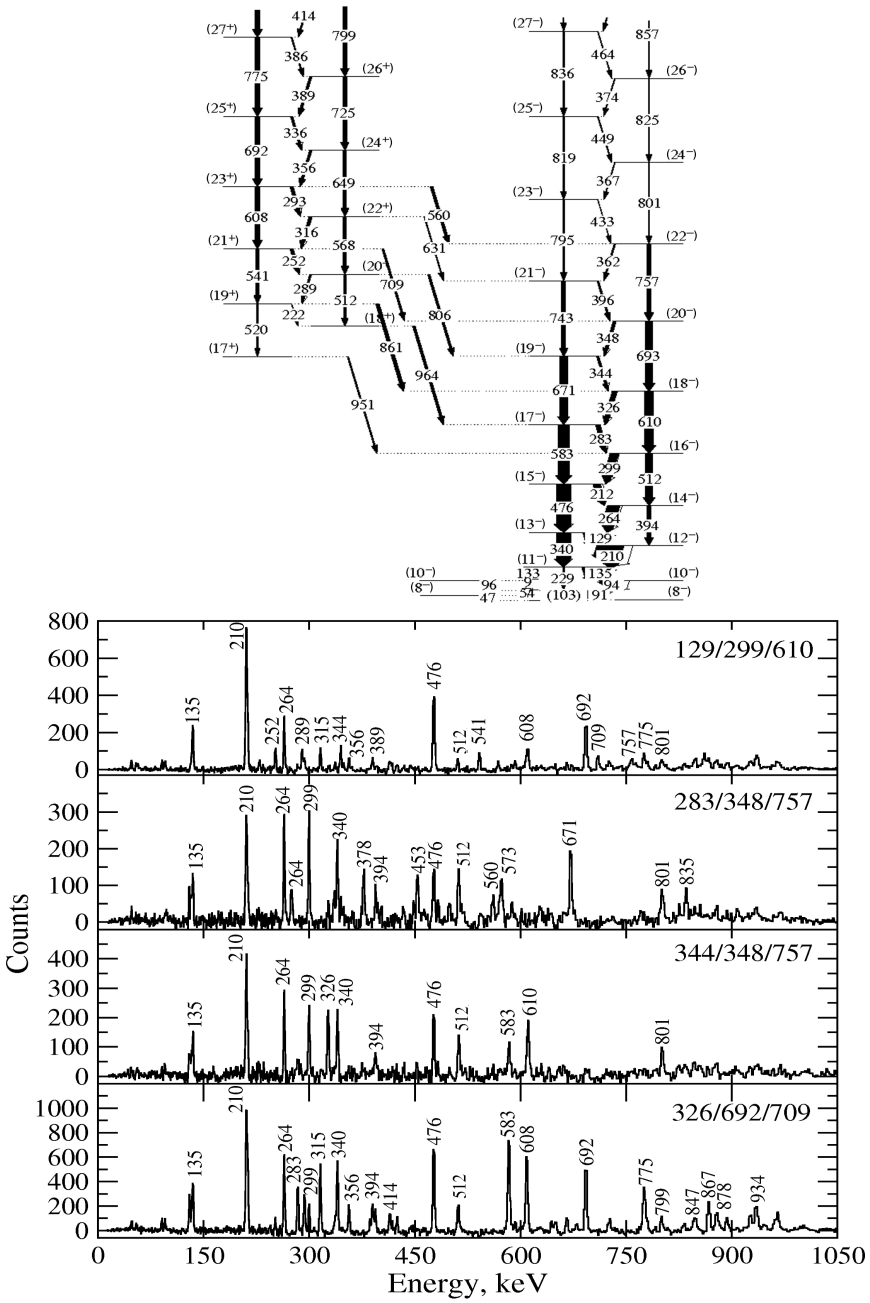

Figure 2.13: A collection of four triple gate spectra are shown beneath the corresponding section of the decay scheme. The energy values set for each triple gate is shown in the top right corner of the spectra. By altering the values set for the gates and observing the changes to what's seen in coincidence a level scheme may be constructed.

same dataset.
To create the hypercube, the raw data collected with GAMMASPHERE was first pre-sorted into the EUROGAM format [31] using the MTSort [32] sorting package to filter out information unnecessary to the analysis such as events recorded during periods when the beam was offline.

2.4.2 Angular-Distribution Analysis

While coincidence analysis is a powerful tool, alone it is not enough to fully deduce the spins and polarities of the various states that are to be mapped out in the constructed level scheme. Since the intrinsic spin and polarity of a given transition can tell us a lot about the interplay of the nucleons within a nucleus it is essential that we determine these traits.
Electromagnetic radiation can be described in terms of a multipole expansion with the defining origin taken to be the electric charge and current densities of the source nucleus. The multipoles are expanded in either electric or magnetic forms, with the emitted photons being described as El for electric or Ml for magnetic, where l is the angular momentum quantum number associated with that photon; 0,1,2,3,... [33]
The parity of these photons are given by (-1)^{l} for electric multipoles and (-1)$^{l+1}$ for magnetic multipoles, thus E0,M1,E2,... conserve parity while E1,M2,... do not.
The vast majority of transitions will consist of low multipoles, and it is often assumed that all such transitions involving the emission of a γ-ray will be E1, M1 or E2 when assigning J$^{\pi}$ values. Since a photon has an intrinsic spin of 1 and thus must carry at least 1 unit of angular momentum, E0 (electric monopole) decays cannot occur through γ emission as the charge distribution remains static and would therefore not produce the spatially varying charge required. Furthermore M0 (magnetic monopole) transitions cannot take place as magnetic monopoles do not exist.
It is the anisotropic manner in which these fields expand which allows for their type to be identified. As the beam ions will typically experience a degree of deflection from Coulomb repulsion before a fusion evaporation reaction the great

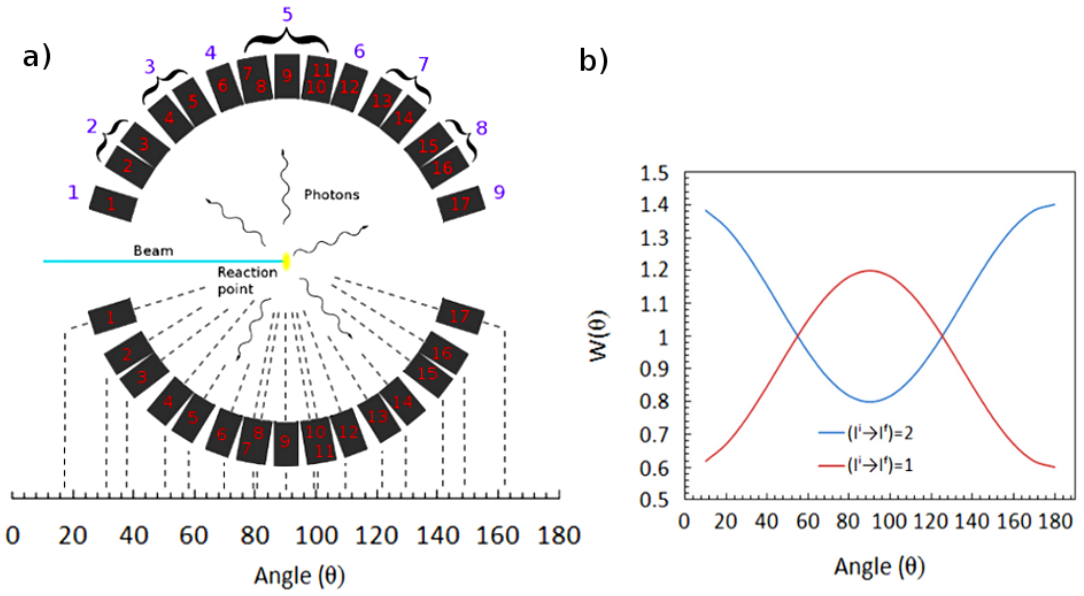

Figure 2.14: a) A sketch of the 17 rings of GAMMASPHERE and their angular positioning. The 9 angles that these rings were subdivided into for the angular distribution analysis is indicated above the array. b) The anisotropic intensity distribution for γ-radiation for dipole $I_i \rightarrow I_f$=1 (red) and quadrupole $I_i \rightarrow I_f$=2 (blue) transactions.

majority of collisions will be off centre leaving the angular momentum of the fusion products aligned about a plane perpendicular to the beam. This gives a consistent polarisation of the excited nuclei, which provides the opportunity to determine the multipolarity of a given γ-ray from the angular dependence of the emitted intensities.

Figure 2.14 shows a representation of the intensity as a function of the detector angle. The angle sensitivity to I^{π} of the emitted radiation can be described in terms of a sum of Legendre polynomials, with the full angular distribution function described through the relation

$$W(\theta) = 1 + a_2 cos^2\theta + a_4 cos^4\theta + ... + a_n cos^n\theta, \tag{2.12}$$

here, θ is the angle relative to the axis of the beamline and a_n is the angular distribution coefficients. Truthfully though the distribution is incomplete and may be sufficiently approximated by a gaussian distribution, and only the first terms

are necessary.

Clearly the method of angular distribution requires two or more detectors positioned at different angles relative to the reaction point, such as the forementioned rings of the GAMMASPHERE detector array. For experiment GSFMA269 a multifold sort was performed using the sorting code MTSort, whereby the 17 rings of GAMMASPHERE were grouped into 9 angles at 17.3°, 34.5°, 54.2°, 69.8°, 90°, 110.2°, 125.8°, 145.5° and 162.7° (also depicted in figure 2.14).
A range of spectra would then be produced for each angle, corresponding to single gate spectra(γ), double gate spectra(γ-γ), triple gate spectra(γ-γ-γ) and so on, with the gates being drawn from a gatelist defined before the data is sorted. This method offers the advantage of being able to project spectra from quadruple gates and above.
A major limitation of angular distribution measurement stems from the requirement for clean and isolated photopeaks. Too few counts and the statistical errors can become too large to meaningfully determine a transitions multipolarity, leading to a diminished effectiveness of the analysis technique at higher excitation energies. This limitation may be exacerbated by the very large quantity of excited states present in some studies such as in the case of high spin studies of nuclei in the rare earth region. Here there will in all likelihood be a large number of overlapping photopeaks from transitions that are close to one another in terms of γ-ray energy. This can easily prevent an accurate measurement of the area of a photopeak from being obtained.

Obviously it is possible to exert a degree of discrimination against overlapping photopeaks through an appropriate selection of coincidence gates, a discrimination that is refined by increasing the requirement for the number of gates in coincidence (ie, γ-γ or γ-γ-γ, etc), however as mentioned in section 2.4.1 each further gate in coincidence will reduce the statistical output of the projected spectra.
Once the spectra is produced the radware package *gf3* was used to determine the areas under a photopeak of interest at each angle. The areas were then normalised to unity to determine experimental $W(\theta)$ values for each angle. Normalisation is achieved through evaluating the percentage of the total recorded photopeaks

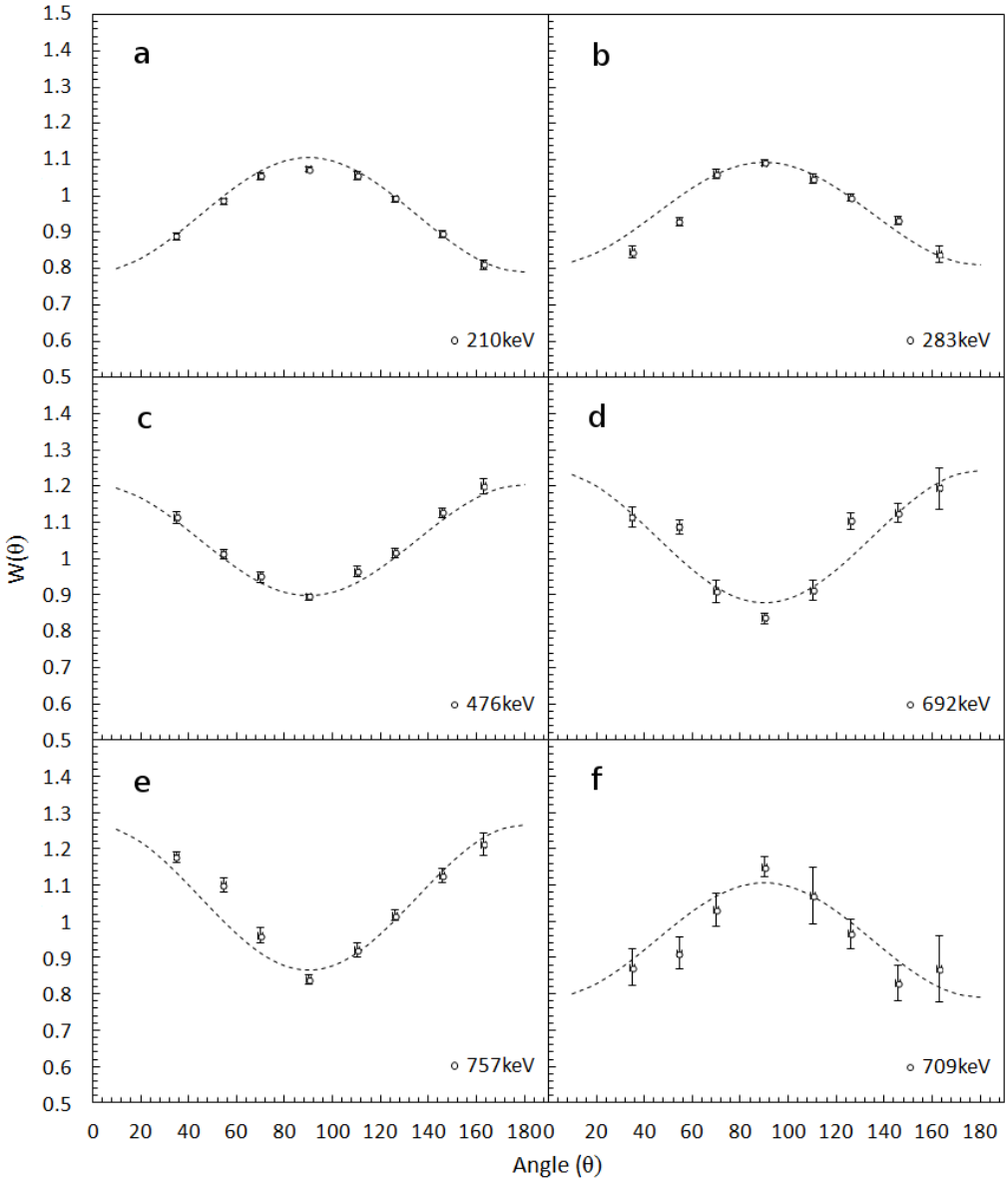

Figure 2.15: *W(θ)* as a function of detector angle for a selection of transitions relating to bands 1 and 2.

area seen at each ring and setting this over the percentage of the total ungated counts across all energies seen at each ring to give the ratio, $W_{exp}(\theta)$. These percentages have been found to provide accurate approximations of the efficiency of each ring.

From the experimentally derived *W(θ)* the angular distribution coefficient can be extracted through fitting the above distribution function to experiment data. Fig. 2.15 shows an example several the fitted angular distribution for M1 transitions, 210 keV and 283 keV, E2 transitions, 476 keV 671 keV and 692 keV and E1 transition, 709 keV.

An alternative manner of expressing an approximation of the anisotropy of a transition is to measure the ratio, R, between the normalised intensity at two different angle by using the formula

$$R = \frac{I_\gamma(\theta_1)}{I_\gamma(\theta_2)}, \tag{2.13}$$

where $I_\gamma(\theta_1)$ and $I_\gamma(\theta_2)$ are the intensities of the photopeaks associated with a given transition seen at angles θ_1 and θ_2.

Naturally it is best to compare angles that maximise the expected difference in *W(θ)*. In the case of the GAMMASPHERE array that which is seen at 90° is set as θ_2 and should ideally be set against a summation of the data collected by the rings closest to the beamline, such as the ring at 17.3,° and it's symmetry counterpart at 162.7,°. However since the ring at 17.3,° was removed for experiment GSFMA269 the low number of detectors at these angles diminishes the coverage of the emitted radiation, This negatively impacts the relative quantity of statistics accumulated and will mean that even at relatively low excitation energies there will be large errors in the measured *W(θ)* value.

Therefore the spectra associated with angles 34.5° and 145.5° were chosen, with the summed percentage of the total counts contributed by the rings corresponding to these angles being approximately the same as the percentage at 90°. Using The intensity ratio, R, for Quadrupole transitions was found to exhibit an $R\approx1.3$ while for dipole transitions the intensity ratio was typically $R\approx0.75$. By angular distribution alone it is not possible to distinguish between E1 and M1 transitions which will lead to some uncertainty, although it is sometimes possible to use the angular distribution results in concert with the alignment characteristics of bands and feeding patterns between bands built on different quasi-particle configurations to clarify the nature of a dipole transition.

Chapter 3

Nuclear Structure: Physics Background

3.1 Introduction

Much of the interpretive and predictive power of the scientific pursuits stems from the models we generate to describe how a system behaves through changing conditions.

Often a model is created as a means of simplifying a complex situation and is later expanded upon to encapsulate new information and discoveries regarding what is being described. This practice has seen considerable success in helping us understand the intricate interplay of the subatomic particles that make up the underlying structure of the nucleus, structures that provide us insights into the broad and rich scope of systematic behaviours beneath the dynamic nuclear landscape represented by the chart of nuclides.

To date no single comprehensive nuclear theory encapsulating all the observed phenomena has yet been formulated, and we instead rely on models which often provide an excellent representation of a nuclides behaviour in one set of circumstances and yet prove inadequate once the situation is changed.

In the following sections an introduction to the theoretical frameworks relevant to this work will be given.

3.1.1 The Liquid Drop Model

The story of modern nuclear structure studies of the atomic nucleus can be considered to have a beginning in the turn of the 20th century, where the works of Becquerel, Rutherford, Geiger, Chadwick and many more gave us our first glimpse of what lay at the core of the atom. By the 1930's this core had come to be seen as analogous to a drop of liquid with the Liquid Drop Model (LDM)[34] gaining favour among the early few models that had been developed by then. One of the principle observations behind the development of the LDM was that the that the nuclear density saturates, with the binding energy per nucleon initially increasing rapidly up to A $\approx$ 10-20. After this point this binding energy as a function of atomic number levels out, becoming approximately constant despite any addition of more nucleons. Owing to this saturation it was found that past A $\approx$ 20 the charge radius of the nucleus can be described in terms of its atomic mass, A, by the relationship

$$R \approx r_0 A^{1/3}, \tag{3.1}$$

where r_0 is an empirically derived constant: 1.2 fm.

This saturation arises from the limited range of the nuclear force ($R_N \sim 1$ fm) restricting the nucleon interactions via this force to only those that are closest to one another.

For nucleons on the surface this finite force distance will mean that they experience the interaction with their neighbouring nucleons in a manner that is different to a nucleon that is completely surrounded, a difference not unlike the surface tension of a drop of liquid. Continuing this liquid drop analogy, the nucleons within the nucleus are considered to be mobile and colliding with one another with a temperature dependant frequency.

The LDM was later refined into the semi-empirical mass formula (otherwise known as the Bethe-Weizsäcker formula or shortened to SEMF)[35] which remains useful for the purpose of explaining particle evaporation, and expresses the nuclear binding energy, E_B, in the form

$$E_B = \alpha_V A - \alpha_S A^{2/3} - \alpha_C \frac{Z^2}{A^{1/3}} - \alpha_A \frac{(A-2Z)^2}{A} - \delta, \tag{3.2}$$

where A and Z have their usual meaning. The right hand side comprises of five terms, the first four of which possess coefficients α_V, α_S, α_C and α_A that are derived by fitting to the empirically determined masses of the nuclei.

The first term, $\alpha_V A$, is known as the volume term and describes the binding energy contribution from the nuclear force interactions of the nucleons. Were every nucleon to interact with one another the total number of pairs available to A particles would be $\frac{A(A-1)}{2}$, however owing to the very limited R_N the number of interacting pairs is more proportional to A.

Since the volume term does not account for the differing situation between nucleons on the surface of the nucleus as opposed to within, a surface term, $\alpha_S A^{2/3}$, is introduced to correct for this. Given that the volume term is proportional to A the radius would be proportional to $A^{1/3}$, therefore giving $A^{2/3}$ as an appropriate representation of the nuclides surface.

The third term, $\alpha_C \frac{Z^2}{A^{1/3}}$, reproduces the repulsive Coulomb force between the protons present. Unlike the situation involving the short ranged nuclear force, there is no limit to range of the Coulomb interaction between charged particles and thus in the case of Z protons present, Z(Z-1) (proportional to Z^2) may be paired although the strength of the interaction is inversely proportional to the range over which it occurs, which may be represented by the radius of the nuclei, or $A^{1/3}$.

An asymmetry term, $\alpha_A \frac{(N-Z)^2}{A}$, is included to account for the fermion nature of protons and neutrons, which means they are subject to the Pauli principle. If we consider the protons and neutrons as independently filling two separate energy "wells", it becomes apparent that the stablest configuration for a nucleus is when the number of protons and neutrons is equal. A surplus of one type of fermion will mean that some of those fermions will be higher in energy than the other type, introducing an imbalance that reduces the overall binding energy. This term is most relevant in the heavier mass nuclei where the Coulomb force drives a trend towards neutron surplus that gradually increases with increasing Z.

Lastly there is a pairing term, δ, which is related to spin coupling. This is the tendency of protons and neutrons to form proton-proton and neutron-neutron pairs. The term reflects the empirically observed changes in binding energy between nuclei that have an even number of protons and neutrons and nuclei that do not.

The trend is that even-even nuclei are the most tightly bound and odd-odd are the least. This phenomena arises from the attractive short ranged component of the nuclear force working in concert with the Pauli exclusion principle, which will be discussed in more detail in 3.1.6.
While the SEMF provided a good description of the overall trends of the nucleus and was successfully employed to explain fission it was increasingly found to be inadequate to fully describe the quantal behaviours observed, such as the existence of especially stable proton and neutron configurations corresponding to what came to be called the "magic numbers". These numbers correspond to quantities of protons or neutrons, namely N or Z = 2, 8, 20 ,28, 40, 50, 82 and 126, where the the overall binding energy per nucleon experiences an increase inexplicable to the SEMF alone.

3.1.2 The Spherical Shell Model

As the body of behaviour discontinuous with the predictions of the SEMF accumulated it became apparent that a seemingly familiar tale was emerging, one which bore more than a passing resemblance to the collection of discrete orbits and shells described in the electron shell model[14].
Indeed, the decrease in binding energy associated with a build up of valence particles in surplus to a proton or neutron magic number is highly analogous to the decreased ionisation energy of electrons in orbit outside of a closed shell. A comparability rooted in the fact that in both cases the same phenomena is responsible: that of the Pauli exclusion principle. Just as how this principle dictates that each new electron added to an atom will incrementally fill shells of increasing energy via occupying available subshell states, also known as *orbits*, so too can the additions of protons and neutrons each be considered as incrementally filling their own respective shells.
Therefore it can be said that spherical shell model (SSM) was an adaptation of the already established electron shell model, to provide a description of the nuclear core, with one important distinction. While the electrons are considered to be moving in orbits established by a Coulomb potential provided by the protons within a tiny core nucleus, the force experienced by the nucleons themselves

comes from their surrounding nucleons.
This complex situation is tackled through approximating the attractive force exerted on a nucleon by those around it, and treating the nucleus as a spherically symmetric potential.
In this manner each nucleon is individually described in terms of their movement within the potential and the specific orbits that they occupy. Naturally the accuracy of this means of describing the behaviour of the nucleons depends strongly on the suitability of the potential that is chosen, with the most realistic form for the potential found to be somewhere between a square well and a simple harmonic oscillator.

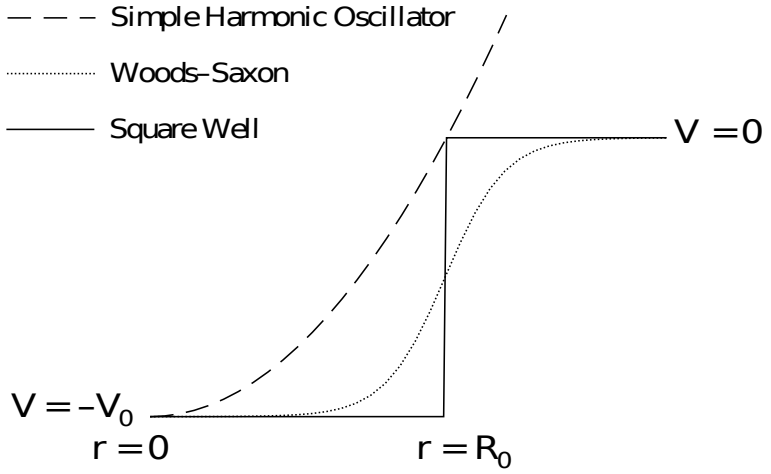

Figure 3.1: A representation of the potential wells discussed in this work. V is the potential well depth, r is the radius from the origin and R_0 is the nuclear radius. Reprinted from reference[9].

3.1.2.1 Simple Harmonic Oscillator Potential

One of the more popular and simple approximations of such a potential well is that of the Simple Harmonic Oscillator (SHO), which takes the form

$$V_{SHO} = \frac{1}{2}m\omega_0^2 r^2 - V_0, \tag{3.3}$$

where m is the mass of a nucleon, ω_0 is the oscillator frequency of the particle, r is the distance from the centre of the potential and V_0 is the potential depth.

The popularity of this potential stems from the fact that despite its simplicity, it provides very good approximate solutions to the complex situation of multiple interacting nucleons.
The energy levels of a nucleon may be determined by incorporating the expression for the potential into the Schrödinger equation

$$\hat{H}\psi = [\frac{-\hbar^2}{2m} \bigtriangledown^2 + V]\psi = E_N\psi, \tag{3.4}$$

thus giving

$$\hat{H}\psi = [\frac{-\hbar^2}{2m} \bigtriangledown^2 + \frac{1}{2}m\omega_0^2 r^2]\psi = E_N\psi, \tag{3.5}$$

where $\hat{H}$ is the Hamiltonian, $\bigtriangledown$ is the Laplacian, ψ is the wave function and E_N is the energy eigenvalues.
Solving the equation for a 3 dimensional spherically symmetric potential, the energy eigenvalues take the form

$$E_N = (N + \frac{3}{2})\hbar\omega_0 - V_0, \tag{3.6}$$

where N is the oscillator quantum number which in this instance is equal to $2(n\text{-}1)+l$. The symbols n and l are the radial and orbital quantum numbers and are 1,2,3,... 0,1,2,... respectively. Each value of N corresponds to a "shell" of nucleons and are degenerate with the maximum number of nucleons in a shell given by the expression (N+1)(N+2).
By itself the SHO potential yields magic numbers at 2, 8, 20, 40, 70 and 112. So while the SHO potential reproduces the first three magic numbers, it fails to correctly recreate any higher magic number. This is unsurprising as an infinitely increasing potential proportional to the square of r alone is a poor representation of the short ranged nuclear force, indeed it should be noted that the deviation from accuracy takes place after the point where the nuclear force is known to saturate.
To better understand this we consider the net force acting on a nucleon within a nucleus large enough that its radius is greater than the range of the nuclear force, R_N. In the case of a nucleon fully surrounded by other nucleons, the boundary

of the nucleus is beyond R_N and the net force acting on that nucleon is therefore close to zero.

If this situation were universal for all bound nucleons regardless of their intra-nucleic position then the ideal potential would be a square well. However, for a nucleon closer to the boundary there will be an asymmetric distribution of surrounding nucleons, and the nucleon will experience an attractive force towards the centre of the nucleus where the relative majority of nearby nucleons will be. The variance in the attractive force experienced by a nucleon is proportional to the nucleons orbital angular momentum. Those nucleons with the greatest angular momentum will be at the greatest distance from the centre and thus will have the most significantly asymmetric distribution of neighbouring nucleons. This forms the logical basis behind the addition of an l^2 term which serves to flatten to the SHO potential. This will reduce the degeneracy of an N shell through lowering the energy of states within that shell by differing degrees depending on their orbital angular momentum, which is depicted in Fig. 3.2.

With this term, the empirically observed magic numbers are still not yet emulated. It takes another adjustment dubbed the *spin orbit* term, which is proportional to $l{\cdot}s$, to form the correct ordering of the subshells [36][37]. This term arises from the spin-orbit coupling of the nucleons. For any nucleon the total angular momentum, $\vec{J}$, carried is a vector coupling of its spin angular momentum ($s = \pm\frac{1}{2}$) with its orbital angular momentum (l), with the resulting force experienced by the nucleon depending on whether the spin and orbital angular momentum align parallel or anti parallel. Effectively this splits any state with orbital angular momentum greater than zero, further reducing the level degeneracy. The magnitude of this splitting is dependant on l, with higher l values experiencing greater splitting as seen in the third column of Fig. 3.2.

With a sufficiently large coupling strength all of the main empirically determined magic numbers are recreated.

The final so-called Modified Harmonic Oscillator (MHO) takes the form

$$V_{MHO} = \frac{1}{2}m\omega_0^2 r^2 - \kappa\hbar\omega_0[2\hat{l}\cdot\hat{s} + \mu(\hat{l}^2 - \langle\hat{l}^2\rangle)], \tag{3.7}$$

where 2κ describes the spin orbit strength and $\kappa\mu$ the $\hat{l}^2$ orbit energy shift.

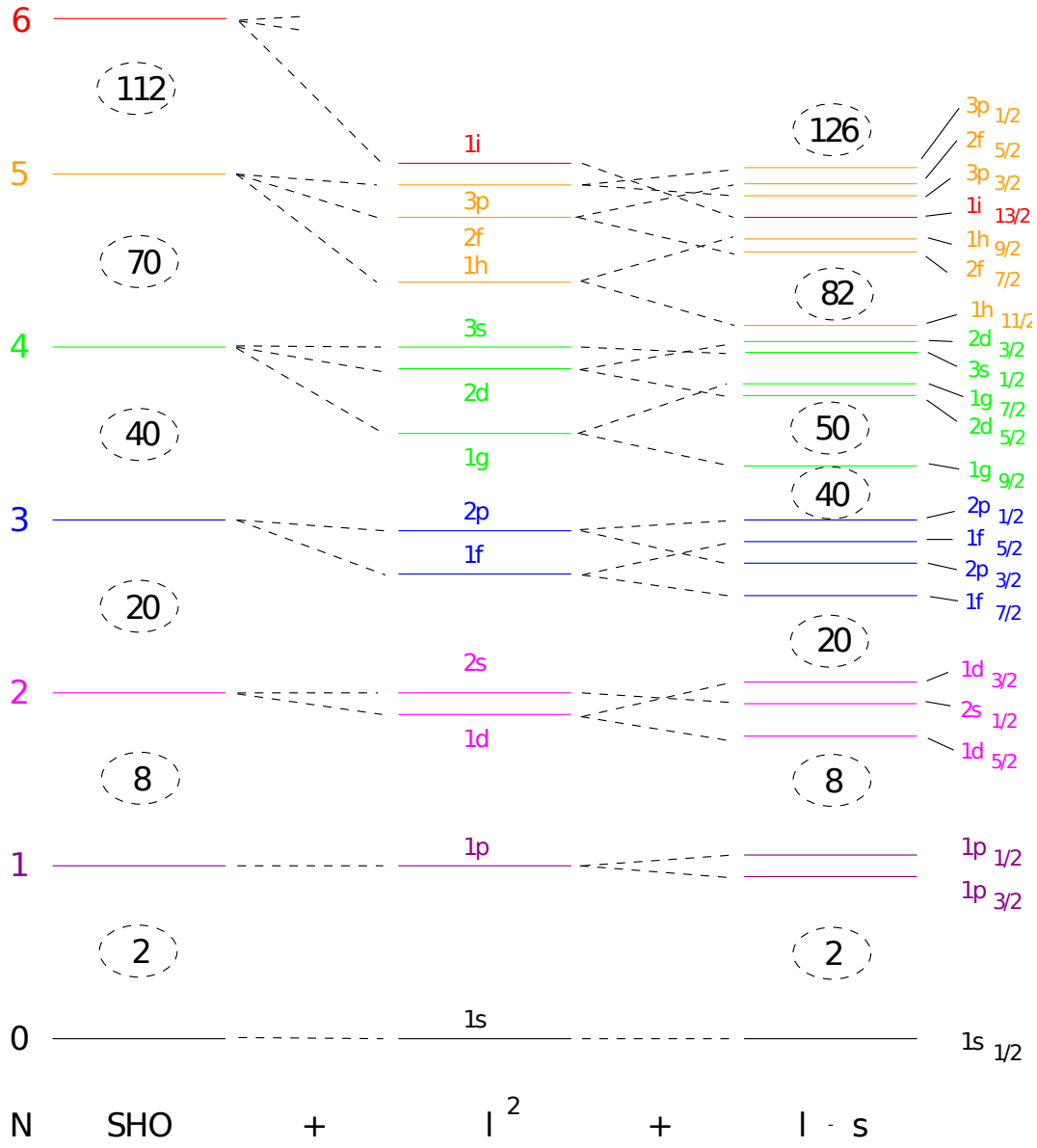

Figure 3.2: A diagram of the energy levels produced by the harmonic oscillator potential and the modifying terms. The simple harmonic oscillator levels are shown on the left. For the centre column the degeneracy of the N shells has been reduced by the addition of an l^2 term which does not yet reproduce the magic numbers. It takes another $l \cdot s$ term (column on the right) to fully reproduce the empirically observed shell structure. Adapted from reference [10].

3.1.2.2 Woods-Saxon Potential

Another potential used for the cranked shell model calculations detailed in section 3.1.5 was that of the Wood-Saxon (WS) potential [38]

$$V_{WS} = \frac{-V_0}{1 + e^{(\frac{r-R_0}{\alpha})}}, \tag{3.8}$$

where V_0 is the potential depth, r is the distance from the centre of the potential, R is the mean nuclear radius and α is the surface thickness.
Shown alongside the square well and SHO potentials in Fig. 3.1, the WS potential is a more realistic representation of the nuclear potential than the harmonic oscillator. However it is more complex expression that does not allow for analytical solutions and analysts often turn to the harmonic oscillator models as a good first approximation.

3.1.3 Nuclear Deformations

As already mentioned, no single model to date can successfully describe all of the phenomena seen across the nuclear landscape. While the treatment of the nucleus as a collection of independent particles within a spherically symmetric potential can be used to accurately portray the systematics of nuclei that exist close to the shell closures associated with the magic numbers, this treatment has been seen to rapidly deviate from experimentally observed behaviour amongst heavier nuclei, with emergent collective phenomena becoming increasingly pronounced as more valence nucleons are added. This is most apparent for nuclei in the midshell regions furthest removed from the shell gaps, ie, with mass numbers $A \approx 25$, $150 < A < 190$ and $A > 220$ [14].
The changing shape of the nucleus can be explained through consideration of the competition between the short ranged (nucleon pairing) and long ranged components of the residual interactions between nucleon pairs [39]. As nucleon pairing favours radial symmetry the nucleus tends towards a spherical form when at or close to the shell closures associated with the magic numbers, where pairing is greatest. Towards the midshell region the relative strength of the long ranged interaction becomes more pronounced, leading to a deformation of the sphere

along multipole expansions, most commonly a quadrupole expansion.
In seeking to detail this shift towards deformation Bohr and Mottelson [40] devised a formalism that treated the nucleus as a sphere like object whose deviation from sphericity is dictated in terms of spherical harmonics, $Y_{\lambda\mu}(\theta, \phi)$, and expansion coefficients $\alpha_{\lambda\mu}$ then its radius from the centre to a given point on its surface can be said to take the form

$$R(\theta\phi) = R_0(1 + \sum_{\lambda=0}^{\infty} \sum_{\mu=-\lambda}^{\lambda} \alpha_{\lambda,\mu} Y_{\lambda\mu}(\theta\phi)), \tag{3.9}$$

where R_0 is the radius of a sphere containing the total volume to be modified, λ is the multipole order of the displacement from sphericity; dipole(1), quadrupole(2), octupole(3), hexadecapole(4), etc. As mentioned earlier, of particular interest is the quadrupole deformation when $\lambda = 2$, which corresponds to the predominant Rugby ball like prolate deformation seen amongst deformed nuclei. The sum of this multipole order gives us five expansion coefficients: α_{22}, α_{21}, α_{20}, α_{2-1} and α_{2-2}.
Three of these parameters indicate the orientation of the rigid body of the nucleus; the so-called Euler angles. As the orientation conveyed by these terms is relative it is possible to simplify them by setting $\alpha_{21} = \alpha_{2-1} = 0$ and $\alpha_{22} = \alpha_{2-2}$.
This gives us two remaining variables; α_{20} and $\alpha_{22}(\alpha_{2-2})$ which may be converted into polar coordinates

$$\alpha_{20} = \beta_2 cos\gamma, \tag{3.10}$$

$$\alpha_{22(2-2)} = \frac{1}{\sqrt{2}} \beta_2 sin\gamma, \tag{3.11}$$

where β and γ are shape parameters corresponding to the magnitude of deviation from sphericity and the triaxiality of the nucleus respectively. These parameters are known as the "Lund Convention" [41] (See Fig. 3.3). In this convention values for γ between -60° (oblate) and 0° (prolate) correspond to collective rotational behaviour with the axis of rotation running perpendicular to the axis of symmetry. Within these limits the value of γ correspond to triaxiality with maximum axial asymmetry at $\gamma = 30°$. At $\gamma = 60°$ and γ = -120° the axis of rotation is the symmetry axis, where angular momentum is gained through the single particle

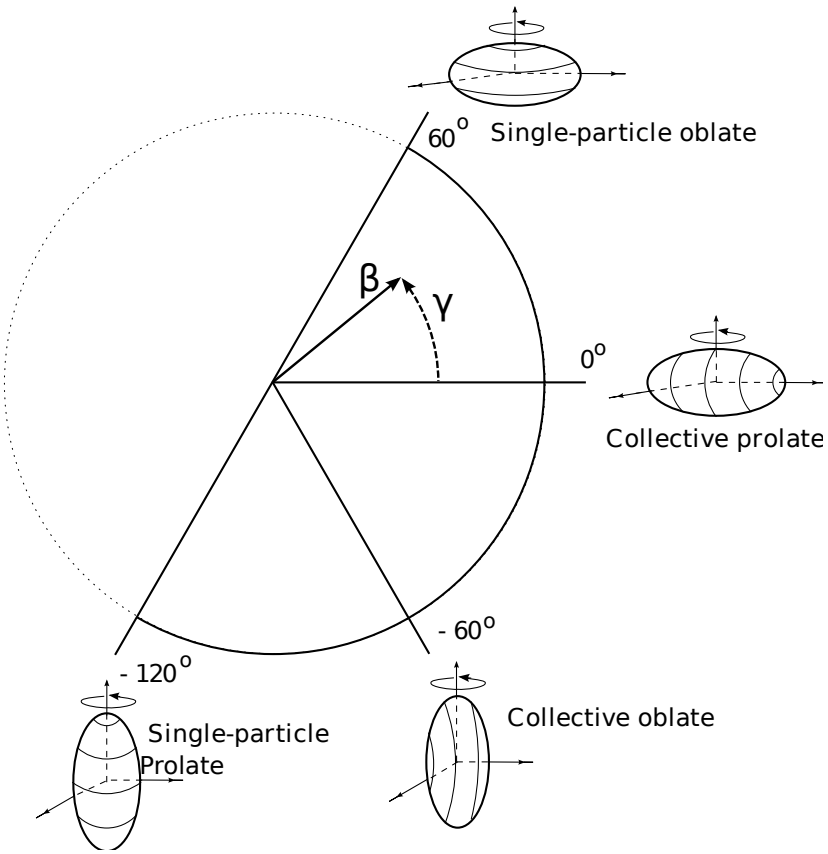

Figure 3.3: The Lund convention. Gamma relates to the specific deformation the nucleus takes relative to the rotation and symmetry axis and β dictates the magnitude of the deformation.

behaviour of the nucleons, akin to the situation of a spherically symmetric nuclei. Using the expressions for α_{20} and $\alpha_{22}(\alpha_{2-2})$ given in Eqs. 3.10 and 3.11 the change in radius along the x, y and z axis of the spherical shape may be expressed thus

$$\delta R_x = \sqrt[2]{\frac{5}{4\pi}} R_0 \beta_2 cos\Big[\gamma - \frac{2}{3}\pi\Big], \tag{3.12}$$

$$\delta R_y = \sqrt[2]{\frac{5}{4\pi}} R_0 \beta_2 cos\Big[\gamma - \frac{4}{3}\pi\Big], \tag{3.13}$$

$$\delta R_z = \sqrt[2]{\frac{5}{4\pi}} R_0 \beta_2 cos\gamma, \tag{3.14}$$

From this it is clear that for fixed $\gamma = 0^\circ$ a positive value for β_2 corresponds to a prolate deformation ($R_z > R_x = R_y$) while a negative value for β_2 corresponds to oblate deformation($R_z < R_x = R_y$).

3.1.4 Deformed Shell Model

Seeking to adapt the methodology of the hugely successful Spherical Shell model treatment of the nucleus to the deformed shapes described in the previous section, the Deformed Shell model, also known as the *Nilsson model*, was proposed by Sven G. Nilsson in 1955 [42]. This simple model has become the most commonly used model for deformed nuclei and for good reason, it manages to describe a great deal of the behaviour seen across hundreds of nuclei, and provides a basis for macroscopic degrees of freedom, such as collective rotation, without losing sight of the quantal properties of the constituent nucleons.

In what follows, two of the major distinctive properties of the Nilsson model with regards to the SSM shall be discussed. First is the obvious distinction of the shape of the nucleus and how this is described in terms of a potential. Starting from the Modified Harmonic Oscillator discussed earlier, the dimensions of the potential may be distorted to incorporate the multipole expansions of the midshell nuclei, with the common prolate (or oblate) quadrupole expansion described by the potential

$$V_{AHO} = \frac{1}{2}[\omega_x^2(x^2 + y^2) + \omega_z^2 y^2], \tag{3.15}$$

where x = y < z for prolate deformation, x = y> z for oblate deformation and ω_x, ω_y and ω_z are oscillator frequencies in the x, y and z directions.

As in the case of the Bohr and Mottelson description of the nuclear shape, the deformed potential of the Nilsson model may also be conveniently expressed in terms of a nuclear deformation parameter, which is related to the oscillator frequencies thus

$$\omega_x = \omega_0(1 - \frac{2}{3}\epsilon_2 cos(\gamma + \frac{2\pi}{3})), \tag{3.16}$$

$$\omega_y = \omega_0(1 - \frac{2}{3}\epsilon_2 cos(\gamma - \frac{2\pi}{3})), \tag{3.17}$$

$$\omega_z = \omega_0(1 - \frac{2}{3}\epsilon_2 cos\gamma), \tag{3.18}$$

where ϵ_2 is the magnitude of the quadrupole nuclear deformation and ω_0 is the spherical oscillator frequency ($\hbar\omega_0 = 41\mathrm{A}^{-1/3}$ when $\epsilon_2 = 0$).
It should be noted that the quadrupole deformation parameter, ϵ_2, is almost identical to the β_2 parameter mentioned earlier, and for small deformations the two values are related by

$$\epsilon_2 \approx \frac{3}{2}(\frac{5}{4\pi})^{1/2}\beta_2 \approx 0.95\beta_2, \tag{3.19}$$

As with the β_2 deformation parameter a positive ϵ_2 corresponds to prolate deformation (x = y < z) whereas a negative value corresponds to oblate deformation (x = y > z).
Now that a deformed potential has been established it is a good time to reflect on the situation of a particle in orbit about the potential. Consider Fig. 3.4, here

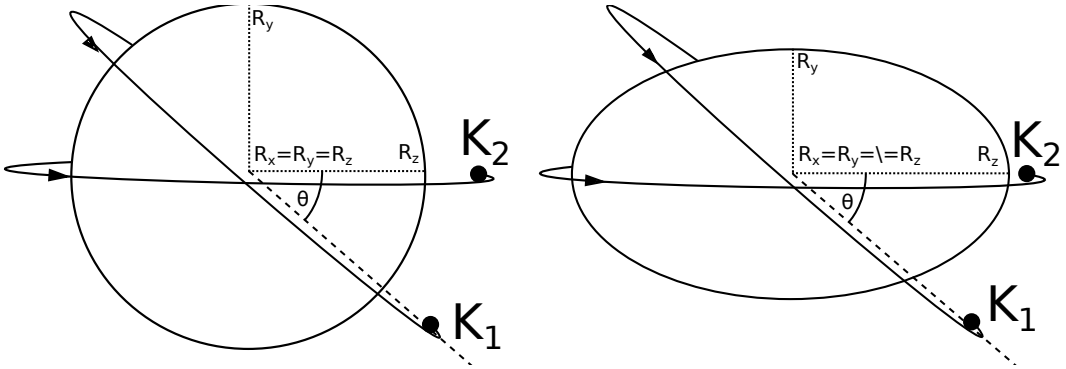

Figure 3.4: Diagram of two nucleons occupying two different K orbitals, K_1 and K_2, both of which orbit at the same distance from the origin. On the left the nuclear volume is spherical and there is no preferred direction as orbitals K_1 and K_2 possess equal energy. On the right a prolate deformation has been introduced, introducing a directional preference by altering the relative distance between these orbits and the bulk of the nuclear material, lowering the energy of the K_2 orbital and raising that of K_1.

K_1 and K_2 are two orbits with identical single particle angular momentum, j, but different orbital planes at angle θ to the symmetry axis, onto which K is the particles projection. As the energy of an orbit depends on its proximity to the bulk of the nuclear material, the closer the orbit is to the rest of the nucleus the lower its energy, and vice versa for an orbit further away from nucleus. Therefore while

the potential is spherical ($\epsilon = 0$) there will be no preferred direction in space and as a result no difference in energy between the two orbits, the shell that the K_1 and K_2 orbits correspond to remains degenerate.
With the introduction of a prolate deformation a discrepancy arises between the two orbits respective distance from bulk of the material, increasing the energy of the K_1 orbit and lowering that of the K_2 orbit, meaning that there is now a dependence on the orientation of an orbit relative to the symmetry axis, thus further breaking degeneracy down to only two (each orbit possesses time reversed symmetry). This is known as K splitting [14].
Note that technically K is the projection of the total angular momentum onto a symmetry axis, the single particle projection for a given orbit with individual angular momentum j is actually denoted by Ω. However, within the conditions of the axis of rotation being perpendicular to the symmetry axis, as is the case with with a prolate $\gamma = 0°$ nucleus, and low rotational frequencies the rotational angular momentum contributes nothing to K. In which case K=Ω and the two terms may be used interchangeably.
The lack of contribution from the rotation of the nucleus stems from the relative frequencies of the orbiting nucleons being considerably greater than the frequency of rotation for the full deformed nucleus at low energies. A condition that does not remain valid as the nucleus goes to higher frequencies, and will be discussed further in sections 3.1.5 and 3.1.8.
Plots of energy levels as a function of ϵ (the so-called *Nilsson diagrams* [43]) for neutron levels in the range $82 \leq N \leq 126$ and protons, $50 \leq P \leq 82$, have been presented in Figs. 3.6 and 3.7 respectively.
Each orbital is labelled in accordance with the Nilsson asymptotic quantum numbers

$$K^{\pi}[Nn_z\Lambda], \tag{3.20}$$

Where π is the parity of the orbital, N is the principle quantum number of the major shell ie, the total number of nodes in the wave function, n_z is the number of those nodes in the z direction and Λ is the component of the orbital angular momentum along the z axis (Λ = K$\pm$1/2). For a representation of how these quantum numbers relate to the properties of orbital angular momentum l, spin s

and total angular momentum j see Fig. 3.5.

When $\epsilon > 0$ there is a decline in energy for the low K value orbits, meaning their

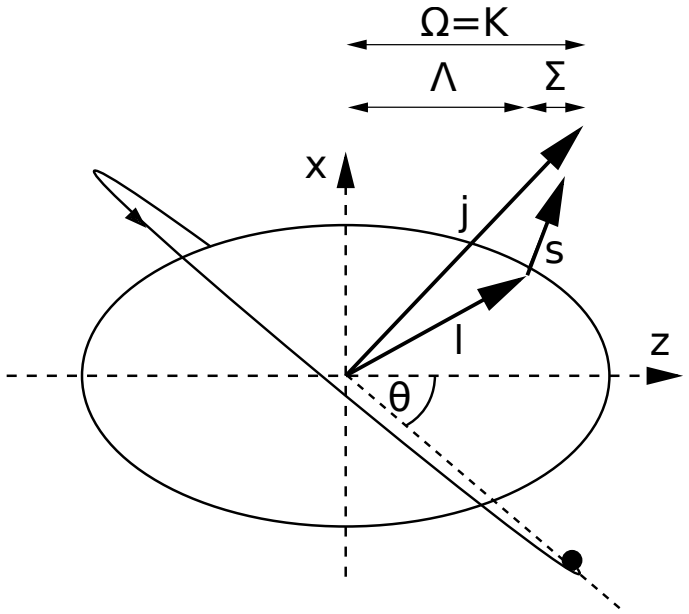

Figure 3.5: Diagram relating the Nilsson quantum numbers to the orbital quantum numbers l, s and Ω. Adapted from reference [11].

orbital motion is aligned equatorially along the prolate nuclides axis of symmetry. Conversely high K values see an increase in energy and therefore occupy an orbit more aligned with an axis perpendicular to the symmetry axis.

The angle of the orbital plane for these orbitals can be approximated by the relation $\sin\theta \approx$ K/j, so for example, the orbital angle of the $1/2^+[660]$ and the $13/2^+[606]$ orbitals would be $\theta = \sin^{-1}(\frac{1}{2}/\frac{13}{2}) = 4.4°$ and $\theta = \sin^{-1}(\frac{13}{2}/\frac{13}{2}) = 90°$ relative to the axis of symmetry respectively. Obviously for when $\epsilon < 0$ (Oblate deformation) this means that the relative adjustments to these orbitals energy levels will be be reverse.

Another component of the Nilsson diagrams which needs to be considered is that of mixing. Since the Pauli exclusion principle forbids two or more identical fermions from occupying the same energy state, the energy level of two states with the same quantum numbers may not cross. The relevant quantum numbers in the Nilsson model are K and π, therefore two orbits possessing the same spin and parity must deflect one another. Following this inflection point the trajec-

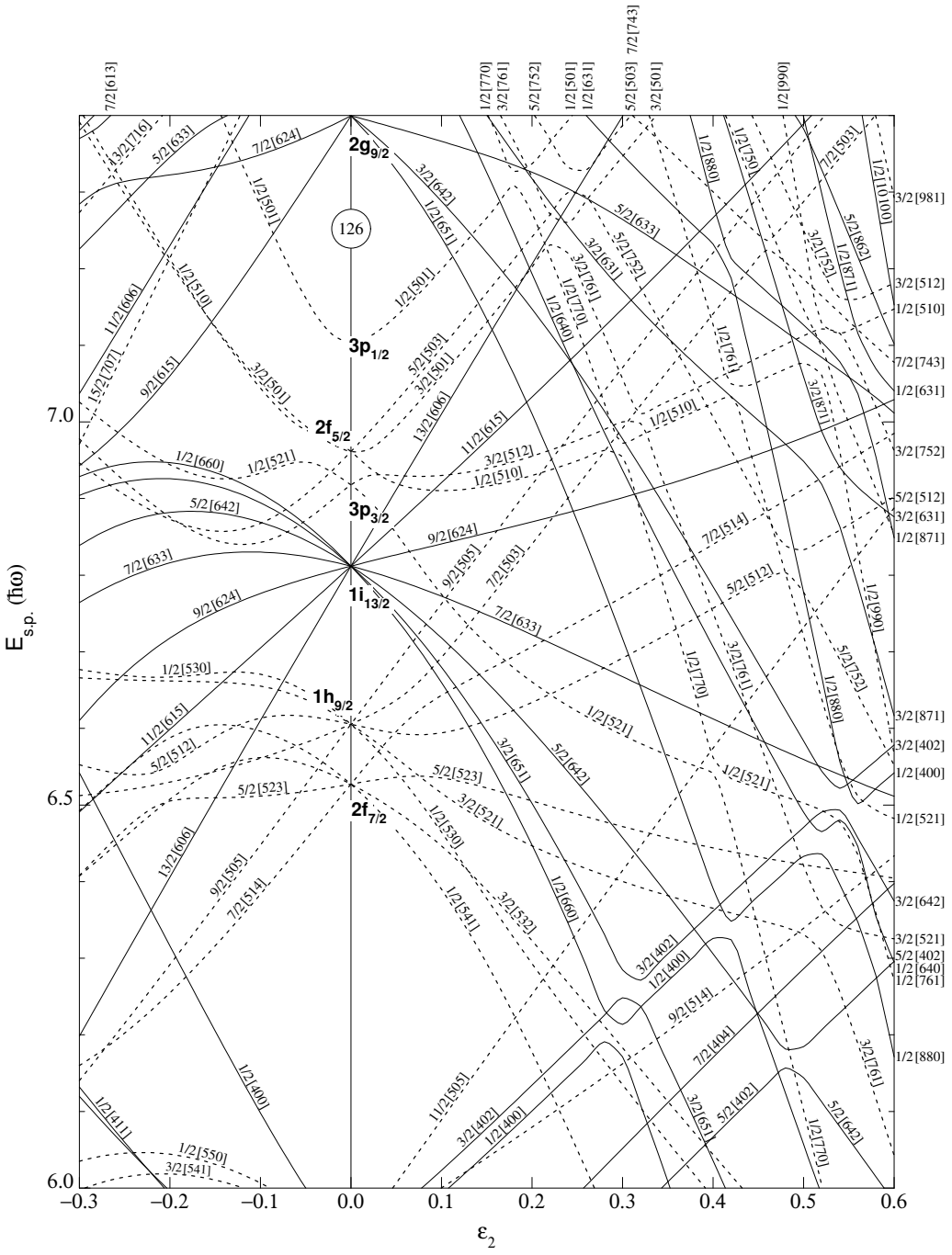

Figure 3.6: Nilsson diagram of the single particle excitation energies, E_{sp} as a function of quadrupole deformation, ϵ_2, for neutrons in the $82 \leq \mathrm{N} \leq 126$ mass range. Reprinted from reference [12].

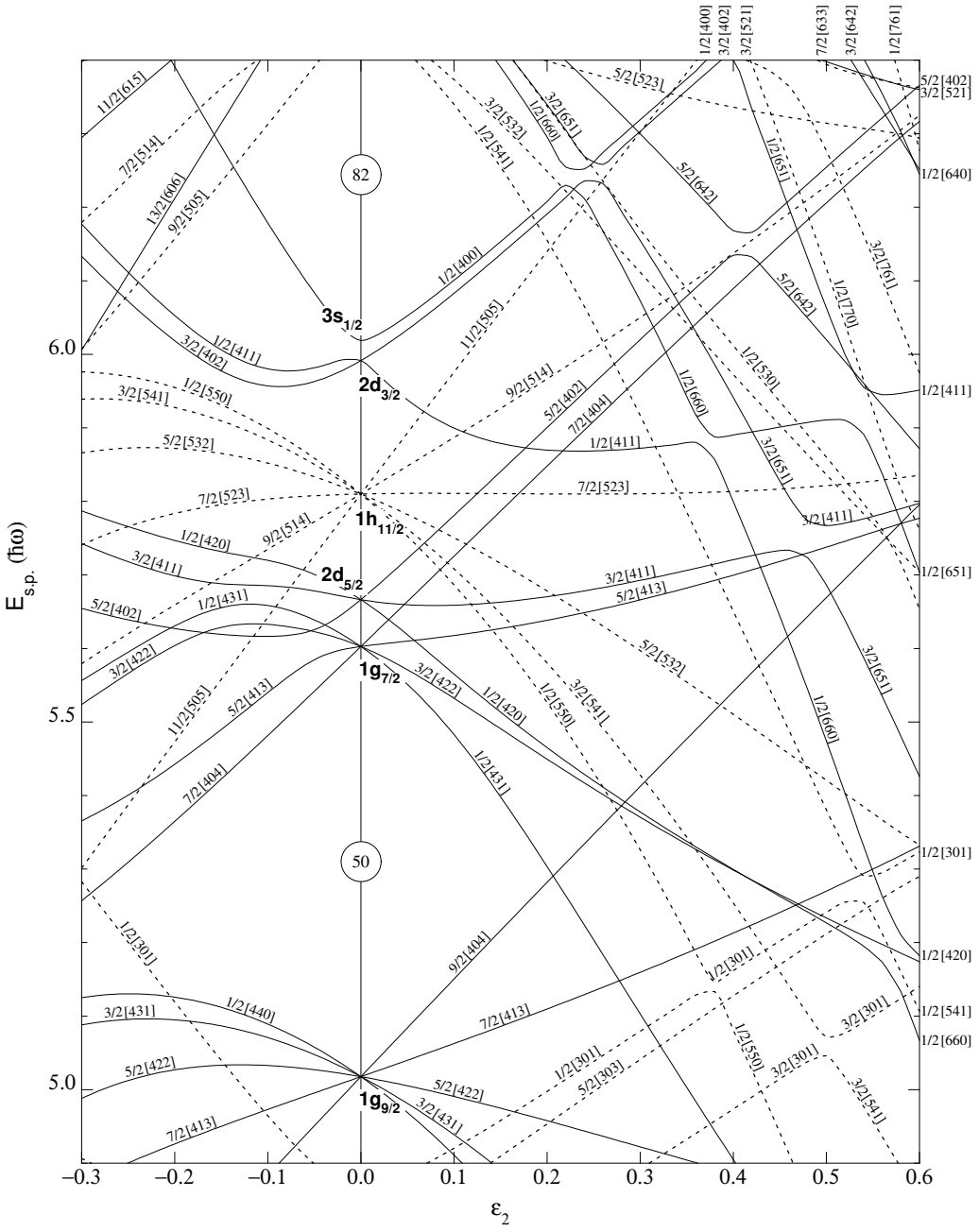

Figure 3.7: Nilsson diagram of the single particle excitation energies, E_{sp} as a function of quadrupole deformation, ϵ_2, for protons in the $50 \leq \mathrm{P} \leq 82$ mass range. Reprinted from reference [12].

tories of each state is swapped, which naturally alters the changing energy as a function of ϵ for these orbitals.

3.1.5 Cranked Shell Model

While the assumption of nucleons orbiting about a static potential used in the Nilsson model provides an powerful approximation at low rotational frequencies, it ceases to remain so when we approach excitation energies high enough for the rotational frequencies of the core nucleus to affect the behaviour of the nucleons in orbit about it through the influences of the centrifugal and Coriolis forces, a limitation which led to the creation of the Cranked Shell Model (CSM) [44][45]. To simulate these perturbations an additional term may be included in the Hamiltonian, giving

$$\hat{H}_\omega = \hat{H}_0 - \omega J_x, \tag{3.21}$$

where $\hat{H}_\omega$ is the modified Hamiltonian, $\hat{H}_0$ is the Hamiltonian for the static nuclear potential and ωJ_x is the quantum operator corresponding to the effects of the Coriolis and centrifugal forces.

This expression embodies the total cranking Hamiltonian, or collective behaviour of the nucleus, and is the sum of all the single particle Hamiltonians, individually given by

$$\hat{h}_{sp_\omega} = \hat{h}_{sp_0} - \omega j_x, \tag{3.22}$$

The eigenvalues of $\hat{h}_{sp_\omega}$ are commonly referred to as Routhians.

As mentioned in the previous section, each Nilsson orbital has a degeneracy of two: the symmetrical, time reversed orbits of two otherwise identical states. The introduction of significant rotation to the nuclear potential breaks this symmetry, thus removing the last remaining degeneracy, as the orbiting nucleons will experience opposing Coriolis forces. The newly separated orbits are referred to as signature partner states, described in terms of their parity and signature, (π, α).

For $\omega J_x \neq 0$ these are the only remaining good quantum numbers as the eigenstates of the Hamiltonian no longer describe the energy states in the lab frame but instead relate to the energy states in the rotating reference frame, which renders the angular momentum projection on the symmetry axis and the total

angular momentum to be both no longer good quantum numbers. Specifically the quantum numbers of parity and signature refer to the invariance with respect to spatial inversions and invariance with respect to 180° rotation about the x-axis respectively.

In the harmonic oscillator Nilsson model convention the parity quantum number is defined by N, Even N orbitals have a positive parity and odd N, a negative parity. The signatures of the two orbits, $\alpha = 0$ or 1 or $\alpha = \pm 1/2$, diverge as rotational frequency increases, an effect known as signature splitting, which is illustrated in the last step on the right of Fig. 3.8.

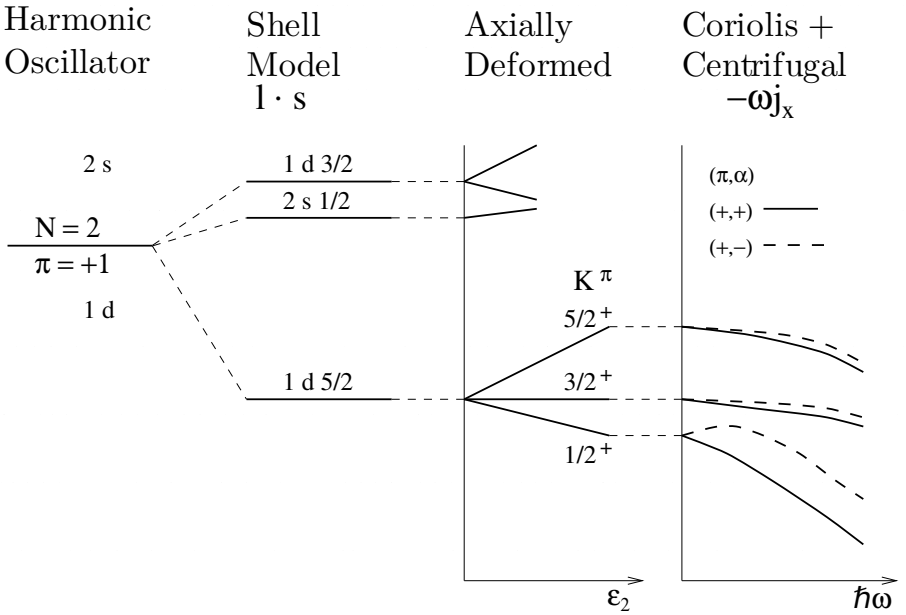

Figure 3.8: Diagram showing the loss of degeneracy with each new adjustment, and the good quantum numbers at each step. Adapted from reference [13].

3.1.6 Pairing Effects

As mentioned in the earlier section discussing the Liquid Drop Model, protons and neutrons exhibit a tendency to form pairs [14] (represented by δ symbol in

the LDM). This tendency bares further discussion as not only does it explain some empirically observed features that fail to be described by the Shell Models thus far, but also, in the development of a systematic treatment of these features in the capacity of the Shell Models, introduces an enormous simplification to how the behaviour of valence particles are described. This is of great benefit in the analysis of experimental data obtained from heavier nuclei.

The empirically observed behaviours associated with pairing are rooted in the existence of an extremely short ranged attractive component to the nuclear force. This component will naturally be most prevalent when nucleons are closest to one another and would be strongest between nucleons that share the same spatial co-ordinates. However, the Pauli exclusion principle restricts nucleon behaviour, preventing identical fermions from sharing the exact same quantum numbers. Therefore the greatest degree of overlap occurs between nucleon pairs moving in time reversed orbits.

Each pair of nucleons possess j and K values that are of the same magnitude but opposing signs, and their combined spins will cancel to zero. This cancellation of spin explains why all even-even nuclei have a groundstate spin and parity of $I^{\pi} = 0^{+}$. Another phenomena present in even-even nuclei that can be explained by the pairing interaction is the typically large amount of energy required to reach the first excited state above the groundstate, a so-called pairing gap of 1-2 MeV. This systematic is not present in odd A nuclei, thereby giving an indication of the strength of the pairing interactions.

The increased binding energy between paired nucleons also ties in with the previously noted differences in the binding energies between nuclei, with even-even nuclei being more strongly bound than odd-even nuclei which are in turn more strongly bound than odd-odd nuclei.

There is a mass dependence on the pairing strength. In heavier nuclei the outermost nucleons are generally further apart meaning that the spatial coordinates between paired nucleons generally will overlap less and thus the pairing interaction will be weaker. A common expression for this dependence is

$$G_p = \frac{17}{A} MeV, \tag{3.23}$$

$$G_n = \frac{23}{A} MeV, \tag{3.24}$$

where G_p and G_n are the strength of the pairing force for protons and neutrons respectively. The repulsive Coulomb force present for protons lowers the effective strength of the pairing force for these nucleons. Close to the Fermi surface, λ,

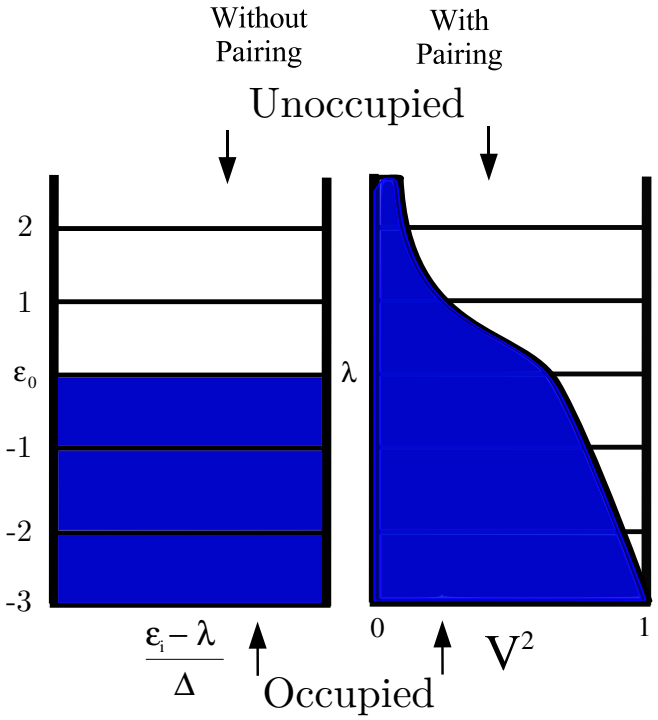

Figure 3.9: Without pairing the orbitals will fill each level consecutively, with a distinct Fermi level defined by the highest occupied orbital. With pairing the Fermi surface is diffuse, producing partially occupied states that are described in terms of quasiparticles. Adapted from reference [14].

there is a "smearing" of the occupied nucleon energy levels, as depicted on the right in Fig. 3.9. This results from nucleons scattering into higher orbitals following a collision, which is quite probable for two nucleons travelling in the same orbital space. Therefore at any given time there will be a number of nucleons occupying states above the Fermi surface, with each nucleon possessing a corresponding hole below that surface.

If nucleons could not form into time reversed orbitals then such collisions would not take place and any new nucleon added to the system would simply raise the

Fermi surface by occupying the next available orbit(See Fig. 3.9). Furthermore the scatterings of paired nucleons do not take place for orbits far below the Fermi surface as the Pauli exclusion principle blocks them from scattering into the already occupied neighbouring orbitals, therefore these nucleons may be discounted in the treatment of the behaviour of the nucleons on the surface.
The difference between the groudstate and the first excited band is known as the pair gap parameter

$$\Delta = G\sum_{i,j} U_i V_j, \tag{3.25}$$

which is summed over orbits i, j. G is the strength of the pairing interaction and U and V are the so-called emptiness and fullness factors, which, respectively squared, correspond to the probability that an orbit, i, is empty or full. The pairing gap parameter Δ may be estimated from the empirical mass difference between adjacent nuclei with odd and even nucleon numbers.
In the fore mentioned scenario of no time reversed orbits, $(\epsilon_i - \lambda)$ would be the excitation energy required to excite one nucleon from the Fermi orbit to a higher orbit, where ϵ_i is the single particle energies, with ϵ_0 reserved for the level closest to the Fermi level. However, with pairing the single particle excitation energy is replaced by a quasiparticle energy, E_i given by

$$E_i = \sqrt{(\epsilon_i - \lambda)^2 + \Delta^2}. \tag{3.26}$$

In this manner the individual nucleons discussed so far (and their hole counterparts) are replaced by a pair of quasiparticle [46][47] representatives describing partially filled levels.

3.1.7 Quasiparticles

This translation from particles to quasiparticles represents a shift in perspective from one based off the last closed shell to one based on the Fermi surface, effectively limiting necessary considerations down to only low energy quasiparticles. This is useful in the case of midshell nuclei whose single particle levels would be high even at the groundstate.
Including pairing in the Routhian, defined in equation 3.22, gives the quasiparticle

Routhian

$$\hat{h}_{qp} = \hat{h}_{sp} - \Delta(\hat{P}^{+}\hat{P}^{-}) - \lambda\hat{N} - \omega j_x, \tag{3.27}$$

where Δ is the pair gap parameter, $\hat{P}^{+}$ and $\hat{P}^{-}$ are the quasiparticle creation and annihilation operators, λ is the chemical potential and $\hat{N}$ is the expectation value of the particle number operator.

The solutions for this equation are often presented in the form of a Routhian

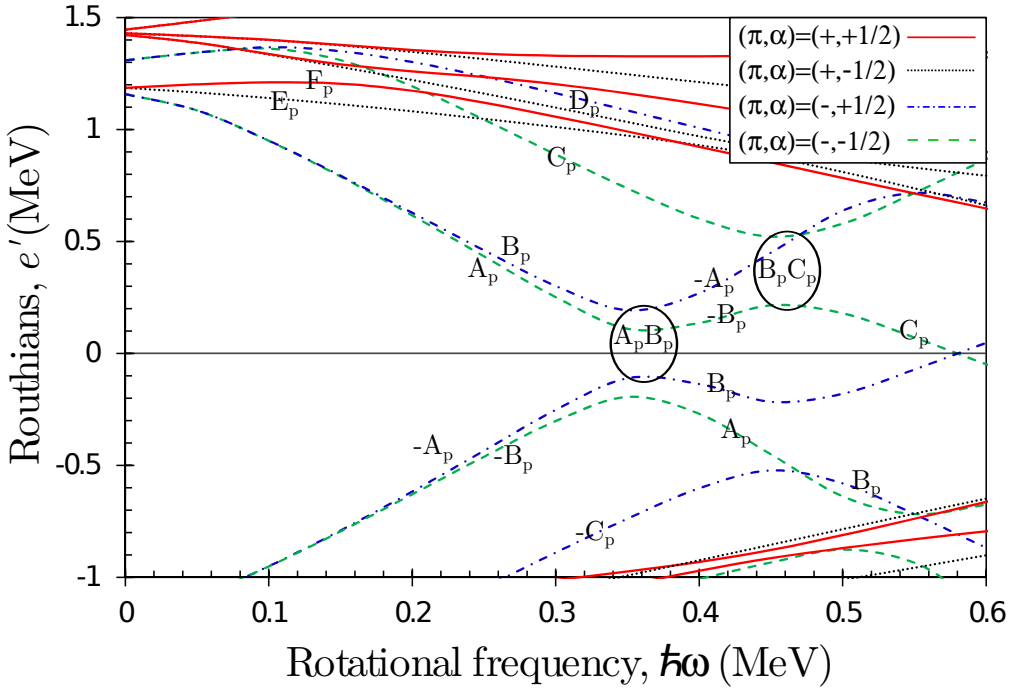

Figure 3.10: Proton quasiparticle diagram of single particle Routhians as a function of rotational frequency, $\hbar\omega$. The signature partner orbitals are labelled in accordance with the convention outlined in table 3.1.

diagram, examples of which are shown for protons and neutrons respectively in Figs. 3.10 and 3.11) where the quasiparticle energies close to the Fermi surface of ^{156}Ho, e′ have been plotted as a function of rotational frequency, $\hbar\omega$.

The quasiparticle orbit in the diagram is labelled by their signature and parity, alongside the Nilsson orbital from which they originate (at $\omega = 0$), which have been abbreviated here using a labelling convention; A, B, C, D, E and F for neutrons and A_p, B_p, C_p, D_p, E_p and F_p for protons. A summary of these labels is

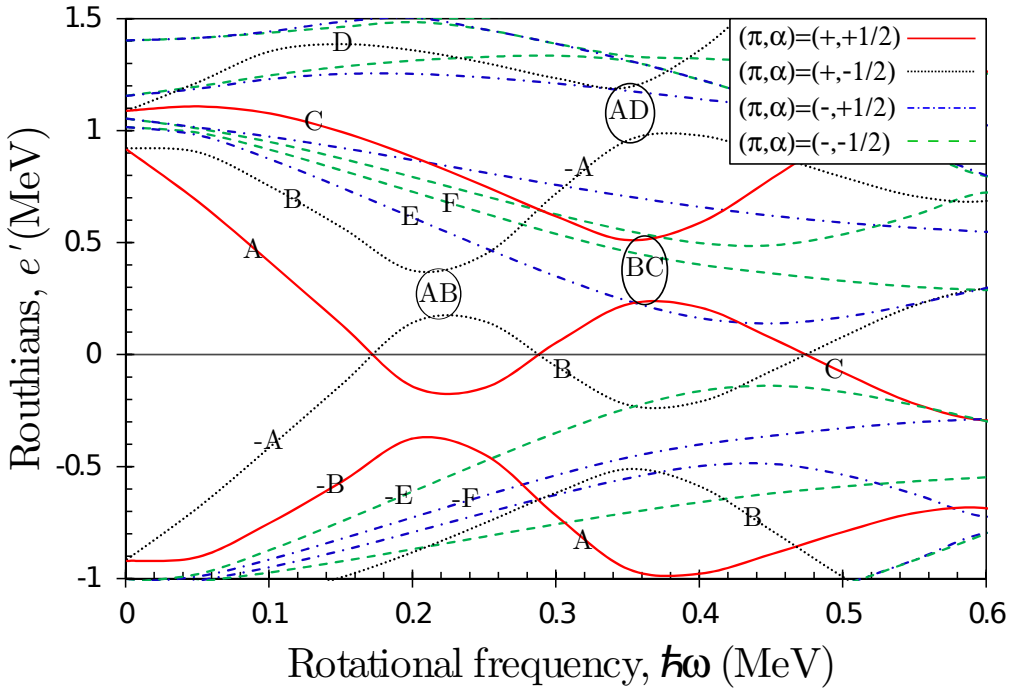

Figure 3.11: Neutron quasiparticle diagram of single particle Routhians as a function of rotational frequency, $\hbar\omega$. The signature partner orbitals are labelled in accordance with the convention outlined in table 3.1.

shown in table 3.1. Each orbital above the Fermi surface (here on referred to as a positive orbital) possesses a mirror image negative state of opposing signature, forming a quasiparticle-quasiparticle hole pair. The status of occupancy for these orbitals at low frequencies is dictated by whether the nucleus is an even mass or an odd mass nucleus. In the case of an even number of protons or neutrons only the negative states are occupied when $\omega = 0$, whereas for an odd number of neutrons or protons the first available positive quasiparticle orbit is occupied and its negative counterpart is empty. The exact value of e' varies as a function of ω depending on the Nilsson orbital from which they originate and the relevant deformation parameters (ie, β_2, β_4 and γ), which shuffles the quasiparticle states as ω increases.

Note in Fig. 3.11 that shortly after $\hbar\omega = 0.2$ MeV the positive A and B orbitals are deflected by the -B and -A negative orbitals, which respectively share the same quantum numbers, π and α. Such an exchange is known as a band crossing,

Table 3.1: Labelling convention for neutron (left) and proton (right) quasiparticles.

Neutron	(π,α)	Nilsson orbit	Proton	(π,α)	Nilsson orbit
A	(+,+1/2)	$i_{13/2}$[660]1/2	A_p	(-,-1/2)	$h_{11/2}$[523]7/2
B	(+,-1/2)	$i_{13/2}$[660]1/2	B_p	(-,+1/2)	$h_{11/2}$[523]7/2
C	(+,+1/2)	$i_{13/2}$[651]3/2	C_p	(-,-1/2)	$h_{11/2}$[514]9/2
D	(+,-1/2)	$i_{13/2}$[651]3/2	D_p	(-,+1/2)	$h_{11/2}$[514]9/2
E	(-,+1/2)	$h_{9/2}$[521]3/2	E_p	(+,-1/2)	$g_{7/2}$[404]7/2
F	(-,-1/2)	$h_{9/2}$[521]3/2	F_p	(+,+1/2)	$g_{7/2}$[404]7/2

specifically in this case the AB crossing. These crossings can only take place when the interaction involves a quasiparticle-quasiparticle hole pair and are otherwise blocked. For example, if there are an even number of neutrons then all of the available quasiparticles will occupy negative orbits below the Fermi surface at low ω and the AB crossing involves an unoccupied A (occupied -A) orbital interacting with an occupied -B (unoccupied B) orbital, therefore the crossing takes place. On the other hand, were there an odd number of neutrons present the first quasiparticle A would be occupied, therefore this crossing would involve an interaction between an occupied A (unoccupied -A) and an occupied -B (unoccupied B) and thus would be blocked.

The quasiparticles do not actually cross into their opposing orbitals in these exchanges and it follows that the status of the first orbitals occupancy will dictate the availability of each crossing that follows, for example in the above case of an even number of neutrons that the second neutron BC crossing at $\hbar\omega$=0.35 MeV would be blocked, and conversely, unblocked for an odd number of neutrons.

In addition to the crossing frequencies there are some other very useful qualities that may be extracted from these quasiparticle diagrams, namely the crossing interaction strengths and aligned angular momentum properties for each orbital. The interaction strength, $—V—$, of a crossing may be defined as

$$|V| = 1/2[|e'_i| - |e'_j|], \tag{3.28}$$

where $|e'_i|$ and $|e'_j|$ are the Routhians for two interacting orbitals at the point where the orbitals are closest. Approximations for the alignment, i, can be extracted

from the slope of e' through the relation

$$i_{\mathrm{x}}(\omega) \approx de'/d\omega. \tag{3.29}$$

Through comparing these extracted properties against experimental Routhian and alignment details alongside a consideration of trends observed in the decay scheme we can build an interpretation of the dynamic structures at play.
Another useful expression of the single particle energies is relative to a γ-dependent reference [48], E'_{ref}, allowing a projection of the expected triaxiality of a specific quasiparticle configuration. Summing the single particle Routhians with such a reference gives

$$E'(\omega,\gamma) = \sum e'_{\mu}(\omega,\gamma) + E'_{ref}(\omega,\gamma), \tag{3.30}$$

with the reference determined through the relation

$$E'_{ref}(\omega,\gamma = \frac{1}{2}V_{PO}cos(3\gamma) - \frac{2}{3}\omega^2\left(\mathcal{J}_0 + \frac{1}{2}\mathcal{J}_1\right)cos^2(\gamma + 30^\circ), \tag{3.31}$$

where V_{PO} is the prolate-oblate energy difference (chosen as -0.4 MeV here). $\mathcal{J}_0$ and $\mathcal{J}_1$ are the Harris parameters [49], which are chosen to produce zero initial alignment and are determined from neighbouring nuclei. For this work the values $\mathcal{J}_0$=32.1$\hbar^{-1}$ MeV^2 and $\mathcal{J}_1$=34.0$\hbar^{-3}$ MeV^4 were chosen as these values give a near constant alignment for the three quasiparticle yrast configuration of neighbouring isotope ^{157}Ho [50].

3.1.8 Experimental Data in the Rotating Frame

In order to compare values derived from the theoretical framework mentioned in section 3.1.7 it is necessary to translate the experiment data into the rotating reference frame. To begin, we relate the rotational frequency, ω, to the experimentally determined excitation energies, *E(I)*, and their associated change in angular momentum, ΔI by the expression [14]

$$\hbar\omega = \frac{dE(I)}{\Delta I_x} = \frac{E(I+1) - E(I-1)}{I_x(I+1) - I_x(I-1)}. \tag{3.32}$$

For a quadrupole transition where $\Delta I = 2$ this may be approximated as $\hbar\omega \approx \frac{E_\gamma}{2}$, where E_γ is the energy of a detected γ-ray.
I_x is the x component of I, in other words the projection of the total angular momentum on the axis of rotation. This is related to the projection of I onto the symmetry axis, K, by

$$I_x(I) = \sqrt{I(I+1) - K^2}, \tag{3.33}$$

where the K quantum number is set as the band head angular momentum. This treatment is additive, so if a band possesses more than one particle in its low spin configuration the angular momentum of the band head is the sum of the constituent K orbitals. For example, the band head angular momentum for a band built on the K = $1/2^+[660]\mathrm{i}_{13/2}$ neutron coupled to the K= = $7/2^-[523]\mathrm{h}_{11/2}$ proton orbitals would be 4. With I_x it is now possible to express the experiment Routhians by the relation [51]

$$E'(\omega) = \frac{1}{2}[E(I+1) + E(I-1)] - \hbar\omega I_x(I). \tag{3.34}$$

At this stage the experiment Routhians, $E'(\omega)$, does not directly translate to the theoretically determined quasiparticle Routhians of section 3.1.7 as they describe the energy of both the core and the quasiparticles. To bring these experiment Routhians into the rotating frame, and thus relative to the quasiparticle Routhians only, a rotational reference term must be defined. For this we start by determining a reference for the alignment

$$I_{\mathrm{x,ref}}(\omega) = \omega(\mathcal{J}_0 + \mathcal{J}_1\omega^2). \tag{3.35}$$

Integrating equation 3.35 with respect to ω gives the energy reference

$$E_{ref}(\omega) = -\int I_{x,ref}(\omega)d\omega, = \frac{1}{2}\omega^2\mathcal{J}_0 - \frac{1}{4}\omega^4\mathcal{J}_1 + \frac{\hbar^2}{8\mathcal{J}_0}, \tag{3.36}$$

where the integration constant has been set to $\frac{\hbar^2}{8\mathcal{J}_0}$ to set the groundstate energy reference to zero.
With these reference terms it is now possible to express the experiment quasiparticle alignment, i_x, and Routhian, $e'(\omega)$ in a manner that can be directly

compared to their theoretical values

$$i_x(\omega) = I_x(\omega) - I_{x,ref}(\omega), \tag{3.37}$$

$$e'(\omega) = E'(\omega) - E_{ref}(\omega). \tag{3.38}$$

Another common interpretation of the experiment data is to plot the γ energies, E_γ, relative to a rigid rotor as a function of angular momentum, I. To determine the rigid rotor reference we begin with the knowledge that for a rotating nucleus I is the sum of the collective rotation of the nucleus, R, and the angular momentum provided by the valence nucleons, J. If only collective rotation is considered then J may be discounted and $I = R$. For a rigid body the classical rotational energy of rotating body is given by

$$E = \frac{1}{2}\Im\omega^2, \tag{3.39}$$

and its angular momentum by

$$I = \Im\omega, \tag{3.40}$$

where $\Im$ is the rigid body moment of inertia, classically expressed as $\Im = mr^2$ with m and r representing mass and distance from a centre point respectively. Combining equations 3.39 and 3.41 we get

$$E = \frac{I^2}{2\Im}. \tag{3.41}$$

Quantum mechanically $I^2 = I(I + 1)\hbar^2$, which gives a rigid rotor reference of

$$E_{rig} = \frac{\hbar^2}{2\Im} I(I+1), \tag{3.42}$$

Which is subtracted from the measured γ energy, E_γ at a given spin, I. In the vicinity of A = 158, the term $\frac{\hbar^2}{2\Im}$ is often approximated as 0.007 MeV.
These plots are useful for determining the yrast band structures at a given spin and in the analysis of a nuclear core changing shape in the lead up to band termination.

3.1.9 Ratio of Reduced Transition Probabilities and Signature Splitting

The reduced transition probabilities provide a means of cross checking the validity of a proposed configuration and are usually expressed in the form of the ratio of stretched E2 to stretched M1 transitions, *B(M1)/B(E2)*. Theoretically these ratios can be determined following the semi-classical formalism of Dönau and Frauendorf [52]

$$\begin{aligned}\frac{B(M1:I\rightarrow I-1)}{B(E2:I\rightarrow I-2)} &= \frac{12}{fQ_0^2 cos^2(\gamma+30^\circ)}\left[1-\frac{K^2}{(I-\frac{1}{2})^2}\right]^{-2} \\ &\{\left(1-\frac{K^2}{I^2}\right)^{1/2}[K_1(g_1-g_R)\left(1\pm\frac{\Delta e'}{\hbar\omega}\right) \\ &+\sum_n K_n(g_n-g_R)]-\frac{K}{I}\left[(g_1-g_R)i_1+\sum_n(g_n-g_R)i_n\right]\}^2,\end{aligned} \tag{3.43}$$

where Q_0 is the quadrupole moment and K_1, g_1 and i_1 represent the K value, g-factor and alignment of the quasiparticle causing the signature splitting in a configuration. The value of the single particle g-factor depends on the shell configuration of the state. g_R and $\mathrm{K} = \sum_n \mathrm{K}_n$ are respectively the rotational g-factor (often taken to be Z/A) and total K value, with the subscript n denoting the quasiparticles of the configuration. The $\pm\frac{\Delta e'}{\hbar\omega}$ term accounts for signature splitting.

The experimentally extracted *B(M1)/B(E2)* ratios are found through the relation

$$\frac{B(M1:I\rightarrow I-1)}{B(E2:I\rightarrow I-2)} = 0.693\frac{E_\gamma^5(I\rightarrow I-2)}{E_\gamma^3(I\rightarrow I-1)}\frac{1}{\lambda(1+\delta^2)}, \tag{3.44}$$

where $E_{gamma}(I \rightarrow I-2)$ and $E_{gamma}(I \rightarrow I-1)$ are the transition energies in MeV, respectively for the $\Delta I = 2$ and $\Delta I = 1$ γ-rays feeding from a given state I. δ is the E2/M1 mixing ratio and λ is the branching ratio, given by the ratio of the $\Delta I = 2$ and $\Delta I = 1$ γ-ray transition intensities

$$\lambda = \frac{I_\gamma(I\rightarrow I-2)}{I_\gamma(I\rightarrow I-1)}. \tag{3.45}$$

The experimental signature splitting between states in strongly coupled bands may be estimated by the relation

$$\Delta E_{split} = E(I) - E(I-1) - \frac{1}{2}[E(I+1) - E(I) + E(I-1) - E(I-2)], \quad (3.46)$$

where *E(I)* is the excitation energy of the state at spin $I\hbar$ and ΔE_{split} is the signature splitting between the signature partners of a band.

3.1.10 Shape Change and the Loss of Collectivity: Band Termination

As has already been established, one of the major differences between the spherical nuclei at the closed shells associated with the magic numbers and their deformed midshell counterparts is the presence of collective phenomena associated with the latter.

Indeed, the treatment of the nucleus as a macroscopically rotating form works very well for describing much of what is seen at low to moderate spins. However the nucleus remains a composite entity and the underlying microscopic properties beneath this collective rotation become increasingly pronounced as spin escalates. For a deformed nucleus gains in spin are acquired through the gradual alignment of the nucleons angular spin vectors with the axis of rotation. As the increasing Coriolis force breaks the nucleon pairs and more valence nucleons align along the equatorial plane the effective behaviour of the nucleus shifts from that of a rotating prolate nucleus to one possessing an oblate deformation whose symmetry and rotation axis are the same [53]. In the Lund convention such a change in shape is characterised by a shift through the triaxial plane, with the γ parameter proceeding from $\sim 0^\circ$ to 60° as spin increases.

This destroys the collective properties present for the rotating prolate form as the rest of the nuclear matter can no longer contribute to any further gain in angular momentum, which now comes solely through the non-collective rearrangement of the valance nucleons. With this situation an upper limit is placed on the allowed angular momentum by the Pauli exclusion principle, whereby the available orbitals are consecutively filled by the now unpaired valence nucleons until all the

available orbits have fully aligned, at which point the band is considered to have terminated.

Terminating bands have been identified in a number of nuclei in the rare earth region, with the textbook case being that of ^{158}Er [43], depicted in Fig. 3.12. Included in this figure is a plot of E - $E_{ridrotref}$ as a function of I, where the the hallmarks of band termination are visible prior to termination in the form of a series of increasingly efficient gains in spin (marked as white triangles) shortly before the terminating states, also known as favoured states (Noted at 46^+, 48^- and 49^-). These states can be reproduced through treating the nuclear system as a build up of valence nucleons around a spherical ^{146}Gd core, giving us eight valence neutrons and four valence protons for ^{158}Er. The terminating configurations may written as a sum of the spins of these valence nucleons by the orbitals that they occupy above the Z=64 subshell closure and N=82 shell closure for an oblate deformation. So, the 46^+ state of $^{158}_{68}\mathrm{Er}_{90}$ is expressed as

$$\pi[(h_{11/2})^4_{16}]_{16^+} \otimes \nu[(i_{13/2})^2_{12}(f_{7/2})^3_{15/2}(h_{9/2})^3_{21/2}]_{30^+} \ ,$$

the 48^- state as

$$\pi[(h_{11/2})^4_{16}]_{16^+} \otimes \nu[(i_{13/2})^3_{33/2}(f_{7/2})^3_{15/2}(h_{9/2})^2_{8}]_{32^-} \ ,$$

and the 49^- state as

$$\pi[(h_{11/2})^4_{16}]_{16^+} \otimes \nu[(i_{13/2})^3_{33/2}(f_{7/2})^2_{6}(h_{9/2})^3_{21/2}]_{33^-} \ .$$

Beyond these configurations further gains in angular momentum will require the breaking of a nucleon pair within the ^{146}Gd core and thus such gains in spin are costly relative to the preceding band terminating states.

The downwards trend seen as a band approaches termination is not always smooth, and prior to a terminating state there can sometimes an energetically favoured low lying state, such as the 38^+ state that precedes the 46^+ terminating state. Such states represent an anti aligned nucleon yet to align its spin vector with the total angular momentum of the valence nucleons.

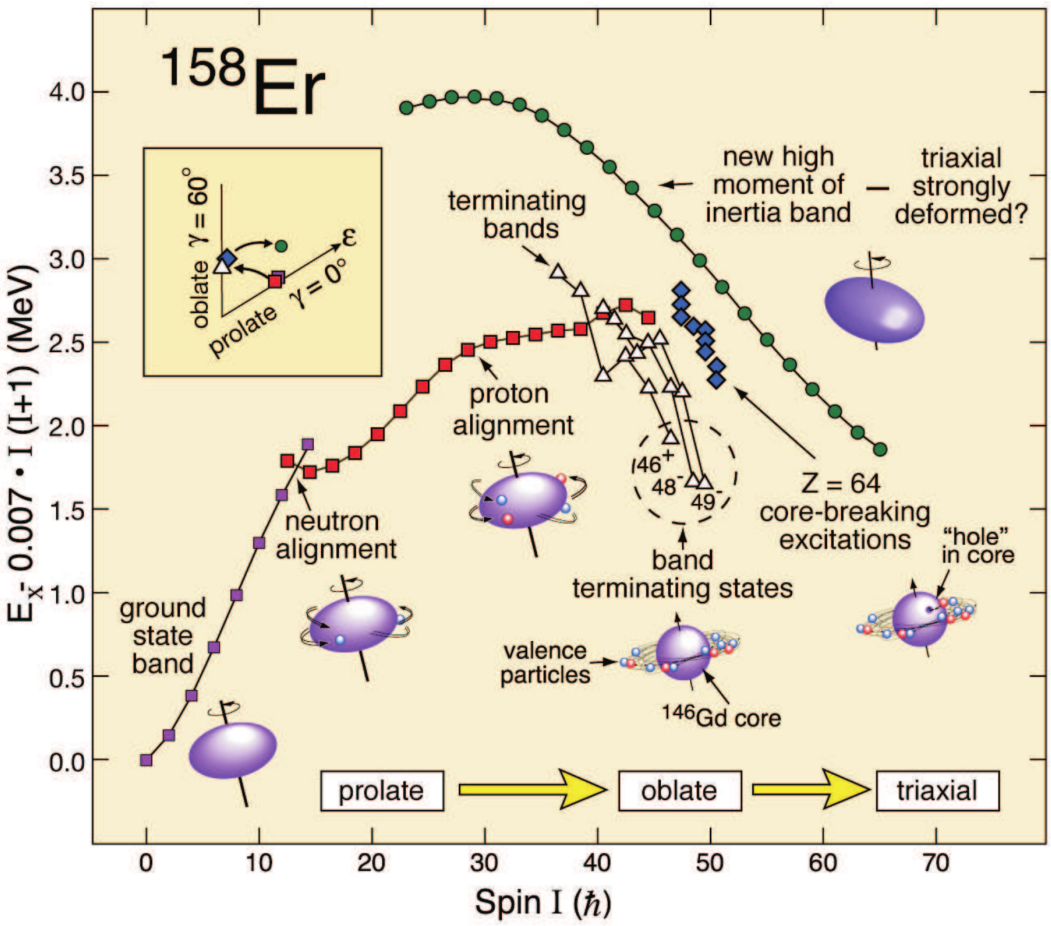

Figure 3.12: Diagram highlighting the textbook example of band termination seen in ^{158}Er. Excitation energies relative to a rigid rotor reference frame are plotted with a representation of the shape change that takes place as the nucleus goes to higher rotational frequency. Reprinted from reference [15].

Chapter 4

Holmium 156: Experimental Details and Discussion

4.1 Introduction

Experiment GSFMA269 took place at the ATLAS facility of the Argonne National Laboratory with the objective to explore collective structures beyond band termination in ^{157}Ho. In order to populate high-spin states in this experiment a 180 MeV beam of ^{37}Cl was directed to bombard two stacked self-supporting thin foil targets of ^{124}Sn of total thickness 1.1mg/cm^2. Over the course of six days a total of approximately 10^{10} coincidence events were collected using the GAMMASPHERE array equipped with 101 Compton-suppressed HPGe detectors, with each event defined as 5 or more HPGe detectors triggered in prompt coincidence. The three most strongly populated nuclei were ^{155}Ho, ^{156}Ho and ^{157}Ho, which were measured to be populated in a ratio of (0.6:1.0:0.3), respectively [9]. The nucleus ^{156}Ho is the subject of this work.

In the off-line analysis these data were sorted into a four dimensional hypercube allowing for quadruple coincidence analysis with the Radware code [29] 4DG8TR and a level scheme was constructed through coincidence relations and measured γ-ray intensities using triple coincidences placed in the hypercube.

Following the methods detailed in chapter 2 an angular correlation analysis was performed to determine the multipolarity of the observed transitions and thus fa-

cilitate the assignment of spin and parity values. Typical angular intensity ratios, R, extracted in this work for stretched dipole ($\Delta I = 1$) and stretched quadrupole ($\Delta I = 2$) transitions were found to be $\sim$0.75 and $\sim$1.3 respectively. Note that to date no transitions have been identified linking the excited structures of ^{156}Ho to an, as yet, undiscovered ground state, hence all spin assignments for this nucleus are uncertain.

For comparison a level scheme from previous work is included in Fig. 4.1. The latest level scheme for ^{156}Ho is shown in Fig. 4.2. Each of the known bands have been extended and four new bands have been identified. To facilitate discussion the bands have been labelled 1-9 with signature partner bands designated with a and b affixes. This labelling convention largely follows that used by Cullen *et al* with a few exceptions: The former band 4 has been determined to be an extension of the former band 6a. These bands have been now consolidated into one band labeled band 4a and the signature partner band 6b is now 4b. The new band 6 is an entirely new structure observed in this work. A complete tabulation of each γ-rays energy and intensity is presented in table 1 alongside all measured angular intensity ratios and the corresponding assigned spin-parity properties. The given intensity values are relative to 210 keV. As there are a large number of transitions in the full level scheme it has been broken down to improve clarity. Bands 1, 2 and 9 are shown in Fig. 4.3, bands 3, 4, 5 and 6 in Fig. 4.4 and bands 7 and 8 have been presented in 4.5.

The results for each band is now discussed alongside examples of projected spectra.

4.2 Results

4.2.1 Bands 1a and 1b

The previously assigned sequences for low-spin yrast bands 1a and 1b have been mostly corroborated in this work and a total of eleven new transitions have been added. The 149 keV and 81 keV transitions previously assigned to the $11^- \rightarrow 10^-$ and $10^- \rightarrow 9^-$ transitions respectively were not verified here. Full spectra for both bands are shown in Fig. 4.6.

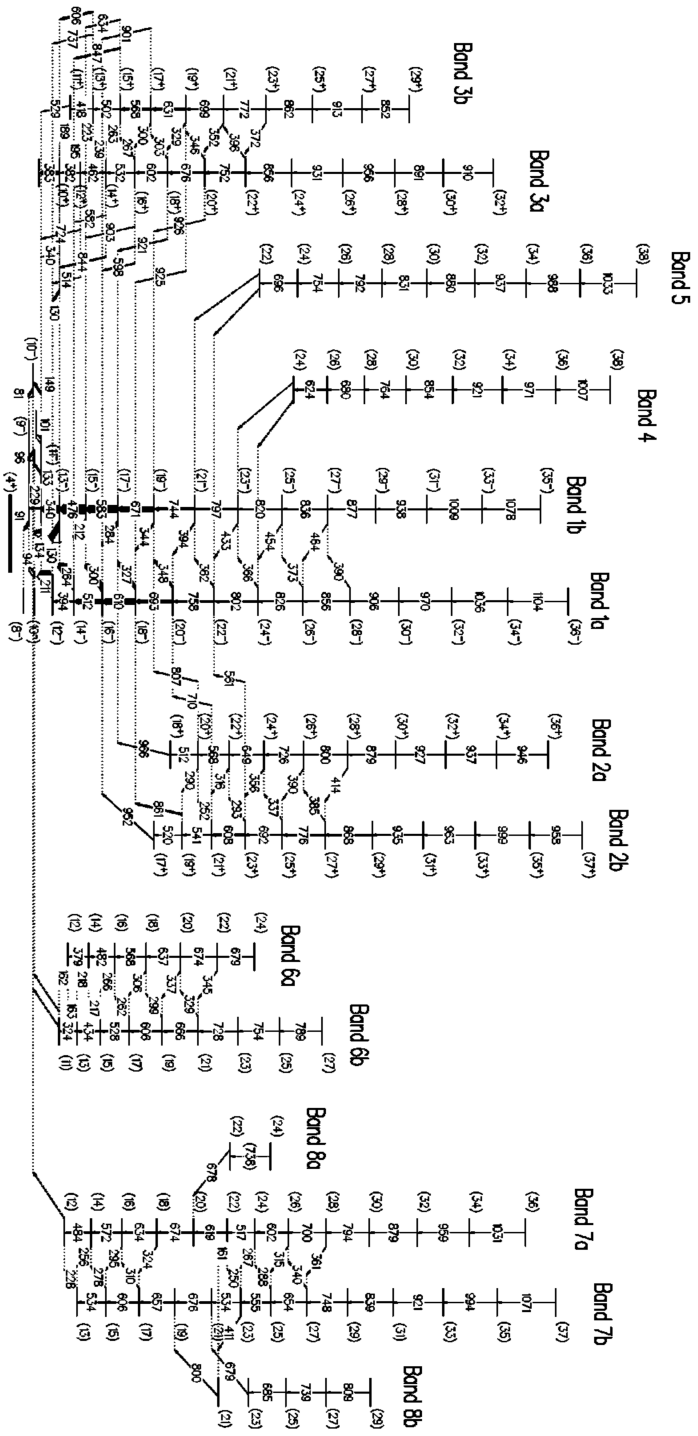

Figure 4.1: Level scheme for ^{156}Ho from prior work. Reprinted from [1].

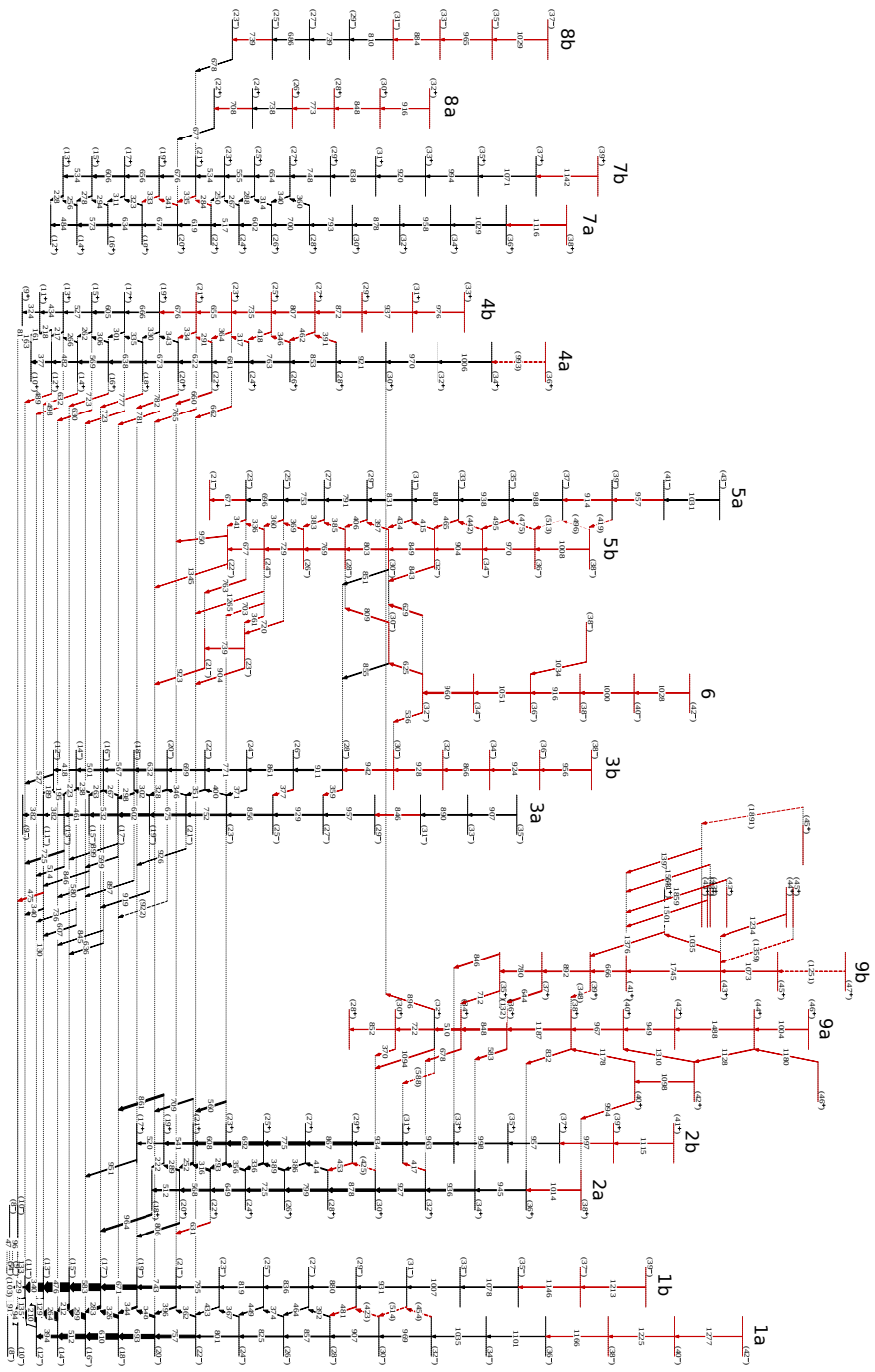

Figure 4.2: Full level scheme for ^{156}Ho as determined in this work. The newly established transitions are shown in red. All transitions are relative to an as yet unknown ground state and therefore all spins and parities are tentatively assigned.

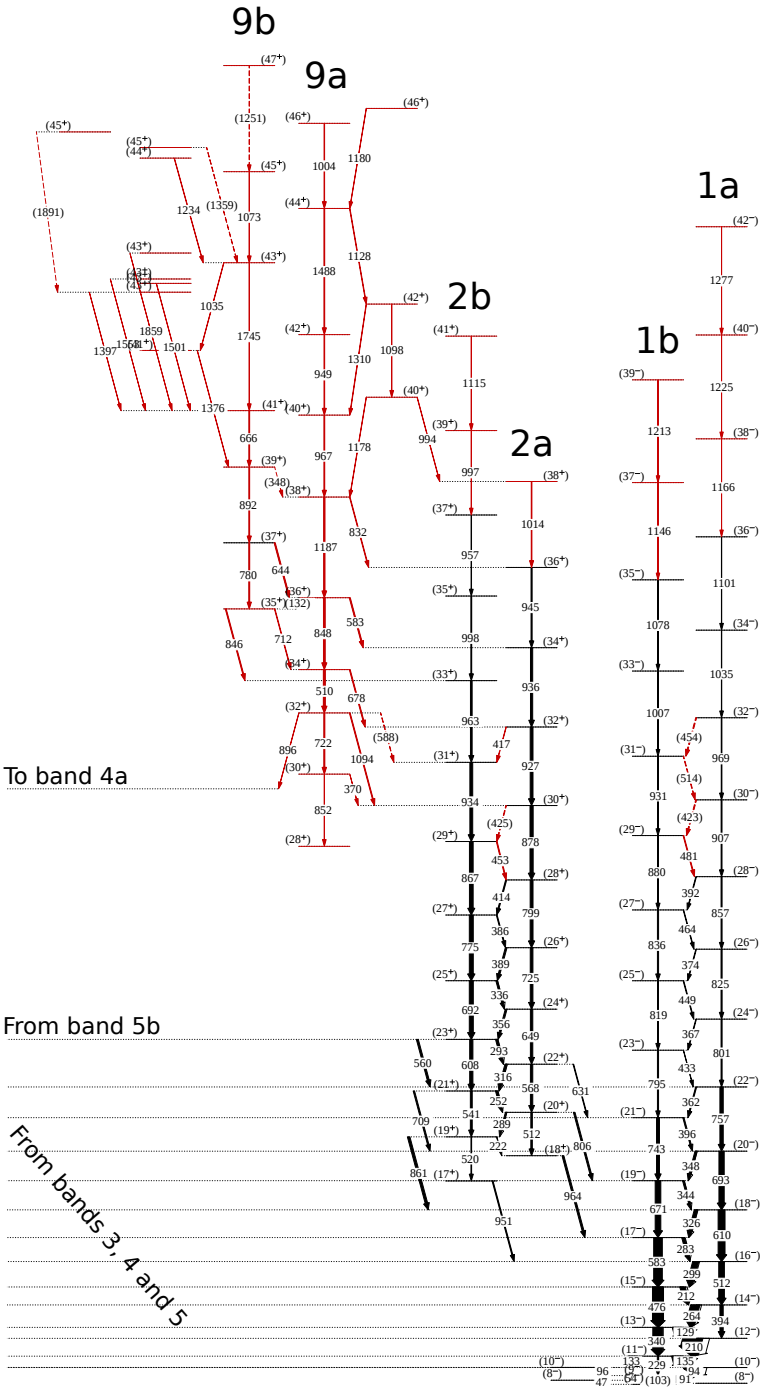

Figure 4.3: Bands 1a(1b), 2a(2b) and 9a(9b) of the level scheme for ^{156}Ho.

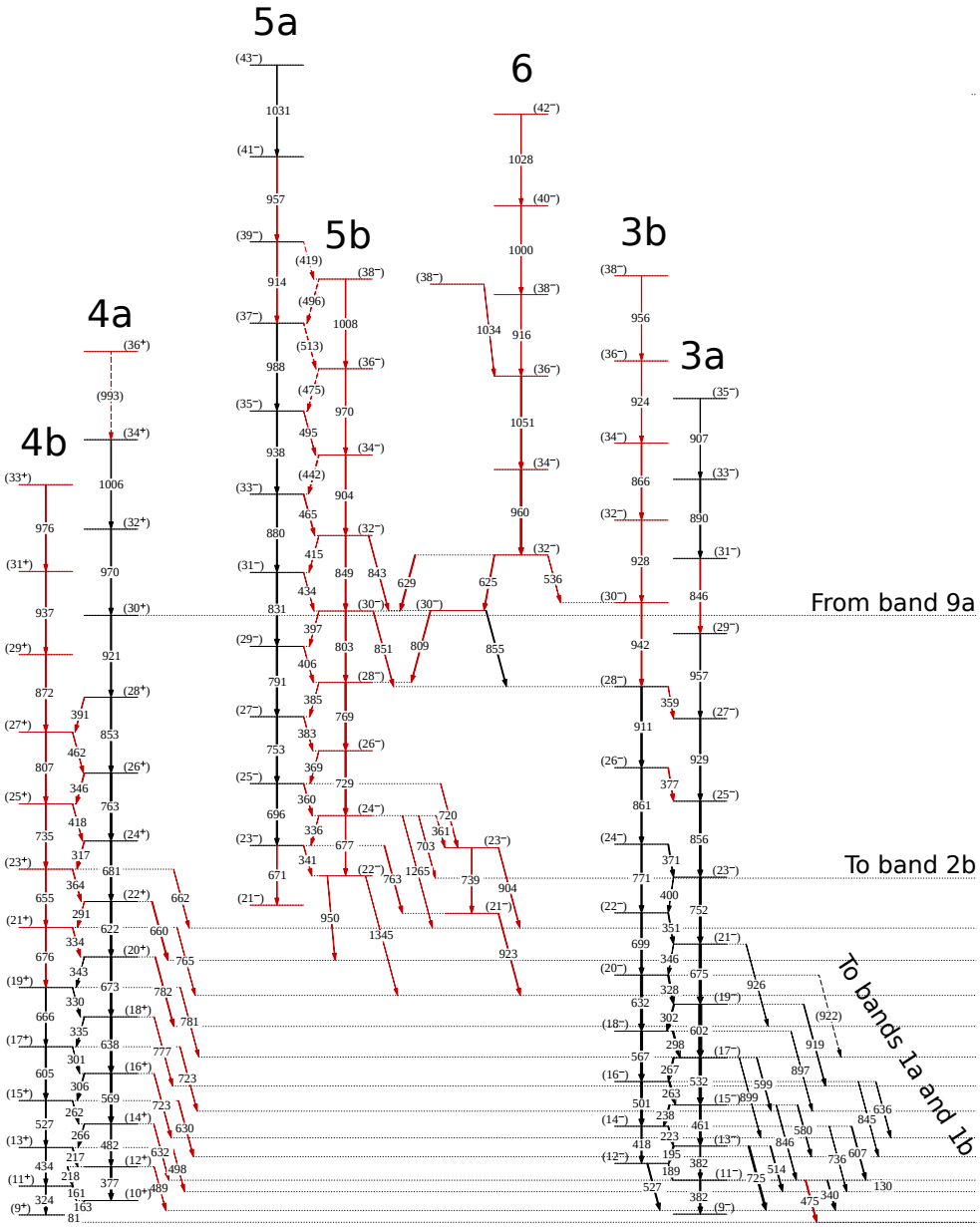

Figure 4.4: Bands 3a(3b), 4a(4b), 5a(5b) and 6 of the level scheme for ^{156}Ho.

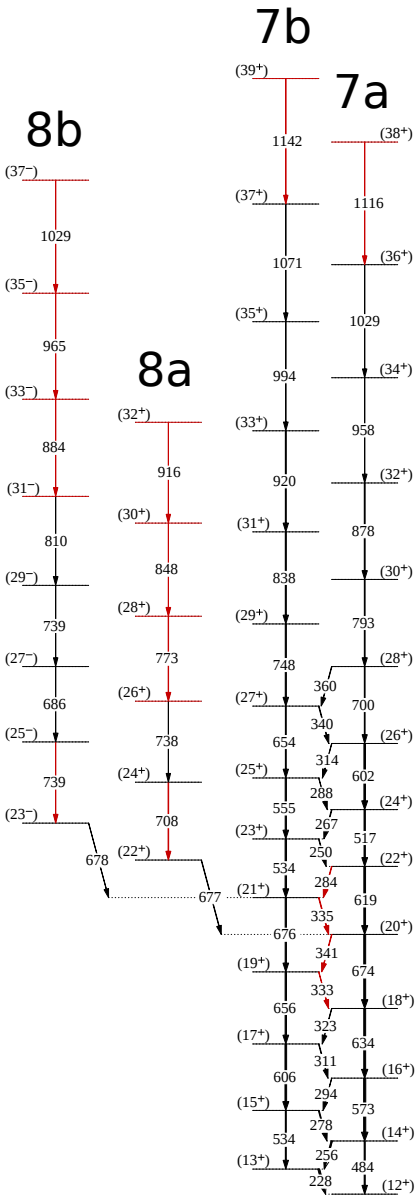

Figure 4.5: Bands 7a(7b) and 8a(8b) of the level scheme for ^{156}Ho.

The highest spin state observed for band 1a has been extended from 36^- to 42^- with new transitions seen at 1166 keV, 1225 keV and 1277 keV. Band 1b has also been extended from 35^- to 39^- through two new transitions at 1146 keV and 1213 keV. In addition to this a low-lying 103 keV γ-ray has been assigned as corresponding to the stretched E2 $9^- \rightarrow 7^-$ transition, although as this transition was hard to distinguish from background it has been marked as tentative.
Four new interband transitions at 481 keV, 423 keV, 514 keV and 454 keV have been assigned as $\Delta I = 1$ mixed M1/E2 transitions linking each state of bands 1a and 1b between 28^- to 32^-, however the 423 keV, 514 keV and 454 keV transitions have been marked as tentative due to low statistics and peak overlap making clear identification of these transitions difficult. Accurately determining the multipolarity of these transitions has not been possible.

4.2.2 Bands 2a and 2b

As with bands 1a and 1b, the previously identified sequence of states for bands 2a and 2b are in agreement with present data. Band 2a has been extended to 38^+ with the addition of a new 1014 keV transition and the 22^+ state has been found to be linked to the 21^- state of 1b via a newly observed 631 keV transition.
Band 2b has been extended from 37^+ to 41^+ through two new transitions with energies 997 keV and 1114 keV. Three new interband transitions between 2a and 2b were observed at 453 keV, 425 keV and 417 keV. These have been assigned as the $29^+ \rightarrow 28^+$, $30^+ \rightarrow 29^+$ and $32^+ \rightarrow 31^+$ transitions, respectively. The 425 keV transition was hard to fully verify and has therefore been marked as tentative.
Above $I^\pi = 30^+$ bands 2a and 2b become more energetically favoured than bands 1a and 1b, which is reflected in the higher intensities for transitions between states in bands 2a and 2b than in bands 1a and 1b above this point.
Angular correlation measurements of the 709 keV, 806 keV, 861 keV and 951 keV transitions linking bands 2a and 2b to bands 1a and 1b show them to be dipole in nature. Considering this with the observation that each state is seen to feed only to one other state in these interband decays (see Fig. 4.2) it is thought to be likely that these transitions are E1, as $\Delta I = 2$ M2 transitions would not be

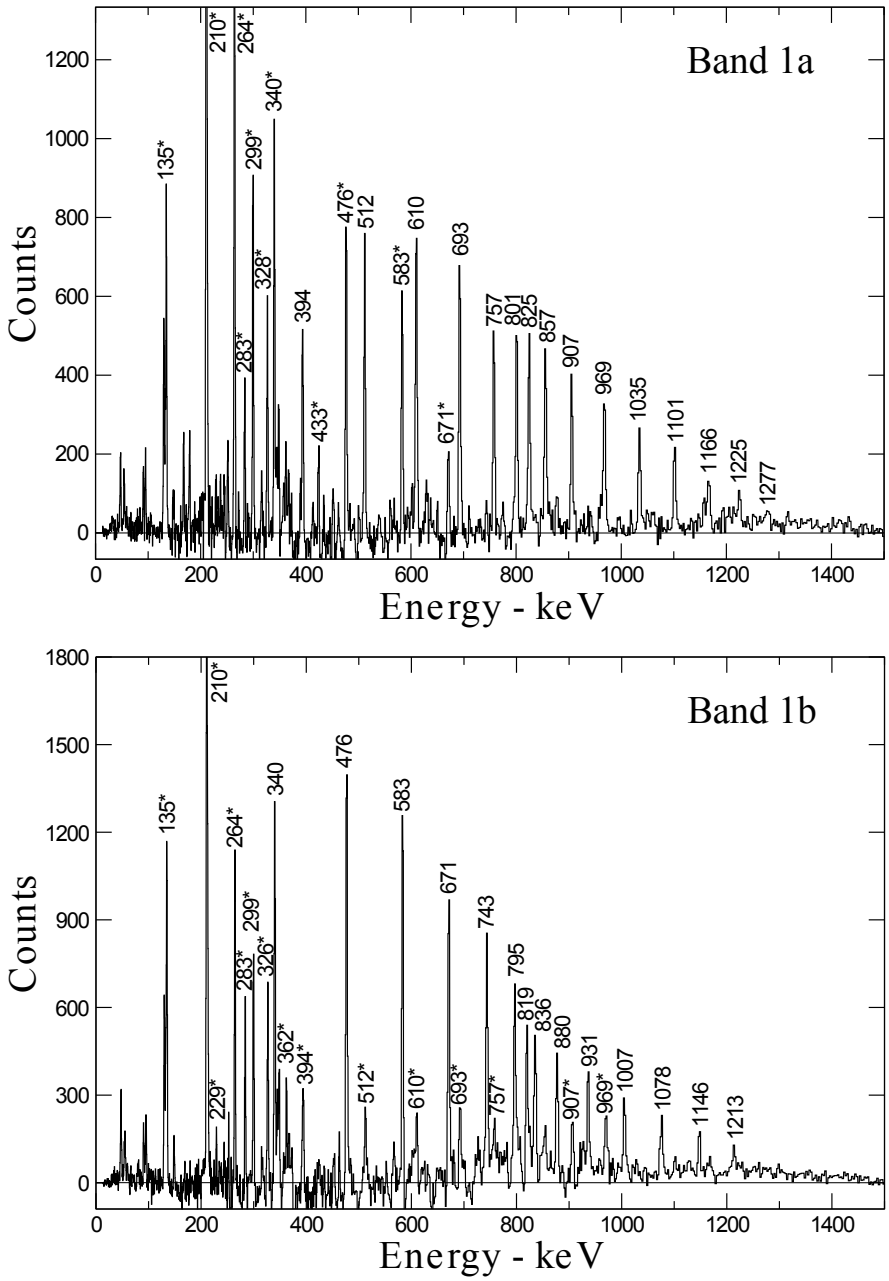

Figure 4.6: Coincidence spectra for the α=1/2 and -1/2 signature partner bands 1a and 1b. The spectra were produced through a summation of triple coincidence gates whereby a gatelist consisting of the top four transitions in a band are set in double coincidence with a gatelist of all the transitions below the top four. All E2 transitions within a signature sequence are plainly labelled while all interband $\Delta I = 1$ or 2 transitions and transitions belonging to another band are marked with an asterix.

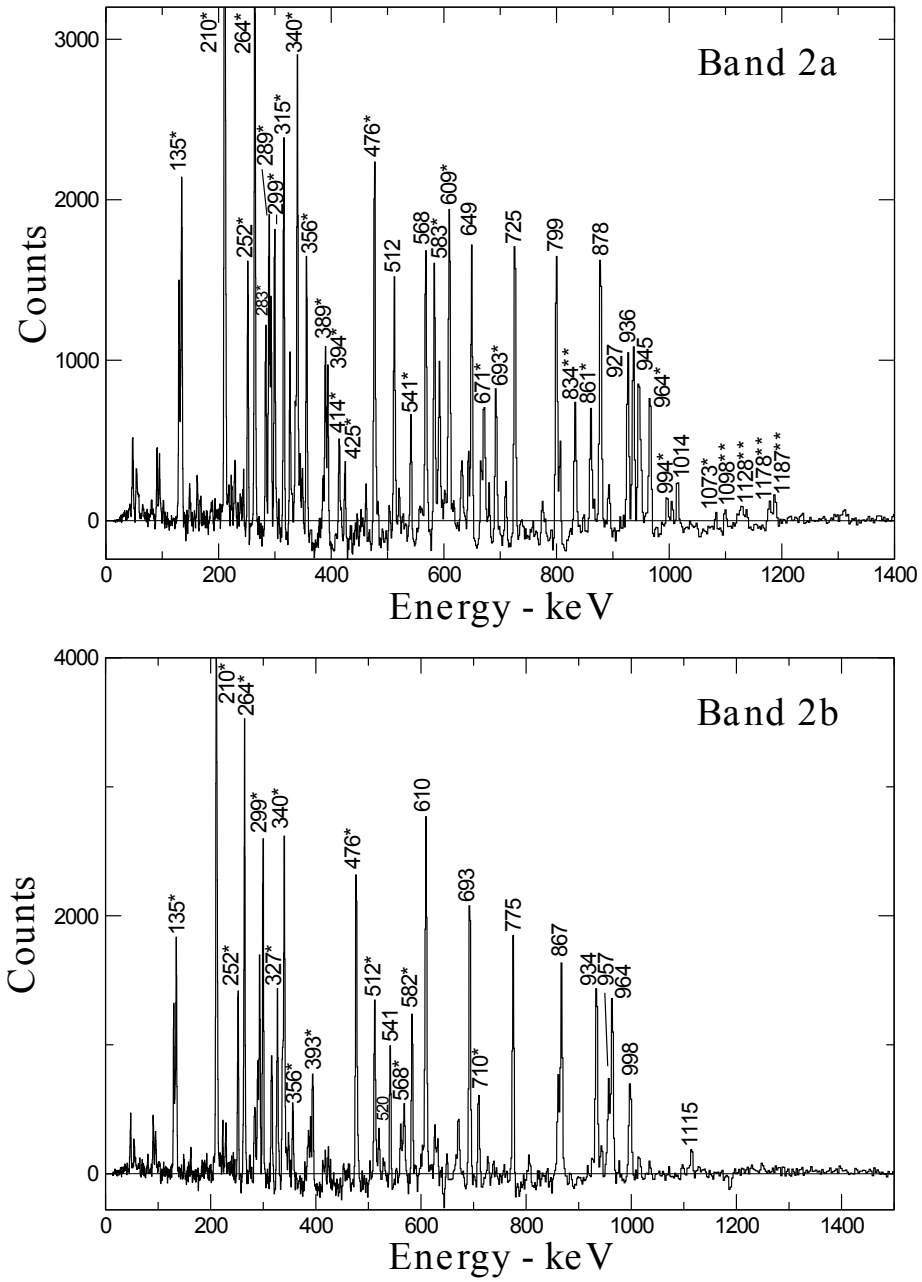

Figure 4.7: Coincidence spectra for the α=1/2 and -1/2 signature partners of bands 2a and 2b. The spectra were produced through a summation of triple coincidence gates whereby a gatelist consisting of the top four transitions in a band are set in double coincidence with a gatelist of all the transitions below the top four. All E2 transitions within a signature sequence are plainly labelled while all interband $\Delta I = 1$ or 2 transitions and transitions belonging to another band are marked with an asterix.

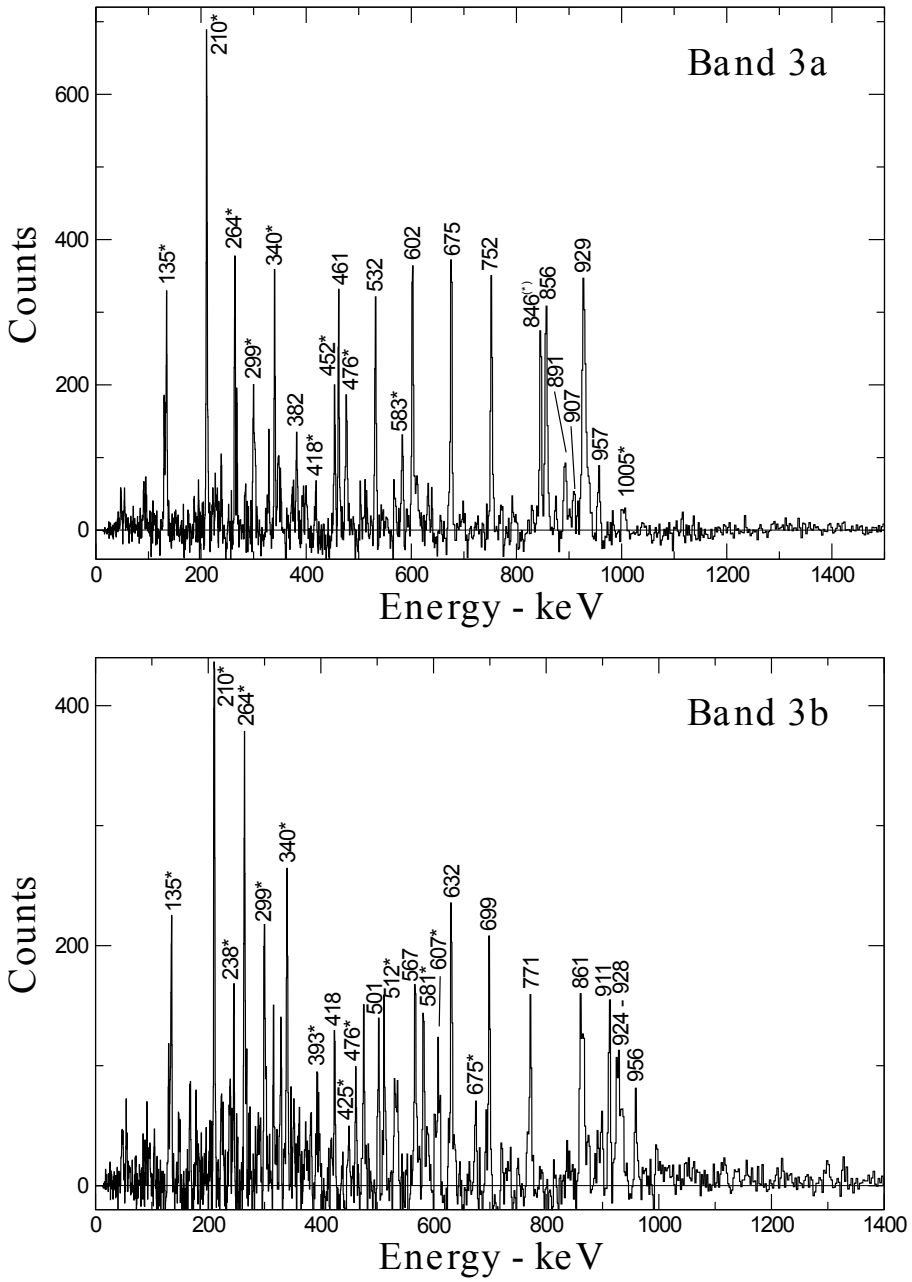

Figure 4.8: Coincidence spectra for signature partner bands 3a and 3b. For 3a the spectrum was produced through a summation of triple coincidence gates from a gatelist consisting of transitions 890 keV, 846 keV and 856 keV set in double coincidence with a gatelist of all the transitions below 856 keV. For band 3b a gatelist comprising 924 keV, 866 keV and 942 keV was set in double coincidence with a gatelist formed of all transitions below 942 keV. Transitions belonging to another band are marked with an asterix.

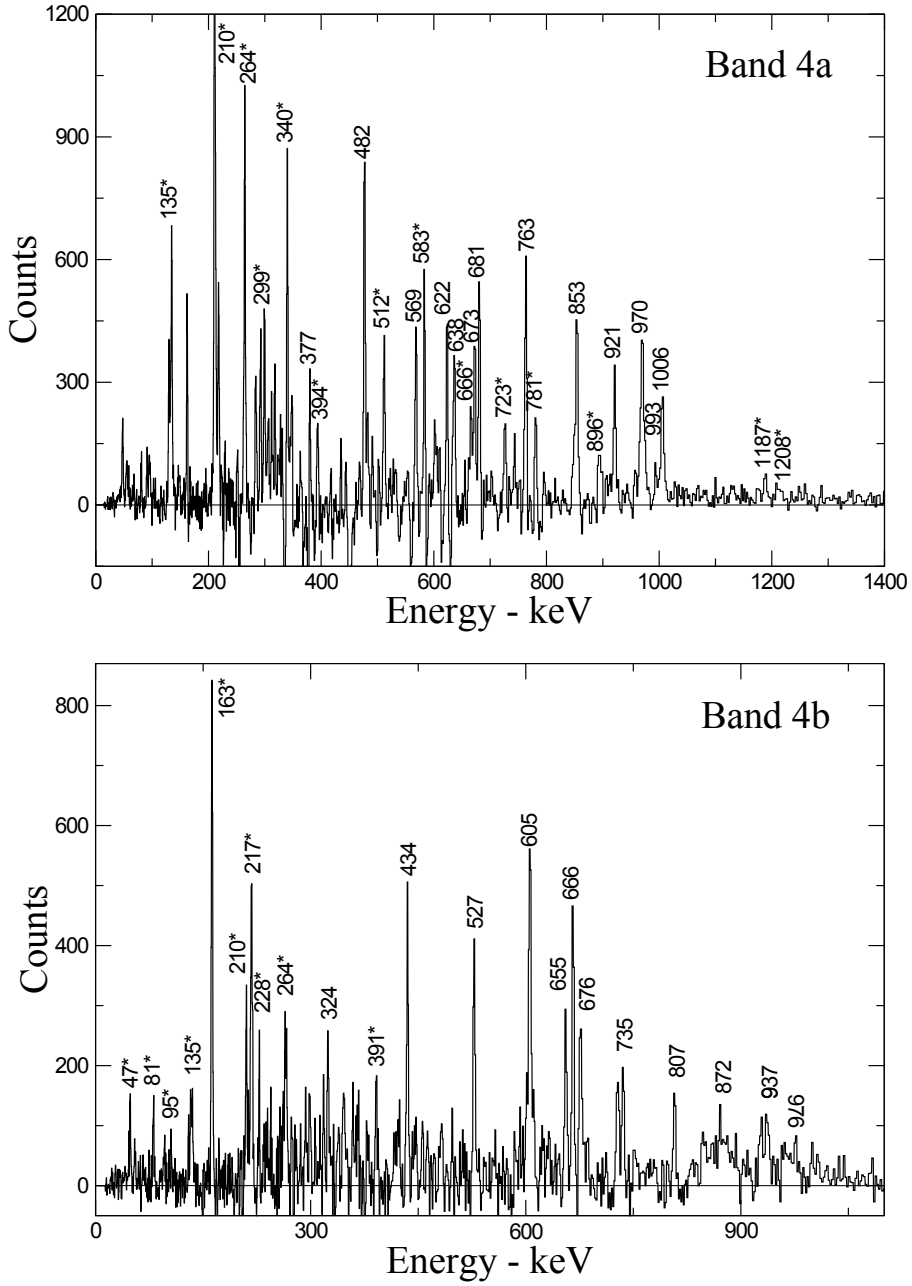

Figure 4.9: Coincidence spectra for signature partner bands 4a and 4b. For 4a this was produced through a summation of triple coincidence gates from a gatelist of transitions 921 keV, 854 keV, 763 keV and 681 keV set in double coincidence with a gatelist of transitions 622 keV, 637 keV, 568 keV and 377 keV. For band 4b a gatelist of all transitions from 735 keV to 976 keV was put in double coincidence with a gatelist consisting of all transitions below 666 keV. All transitions belonging to another band are marked with an asterix.

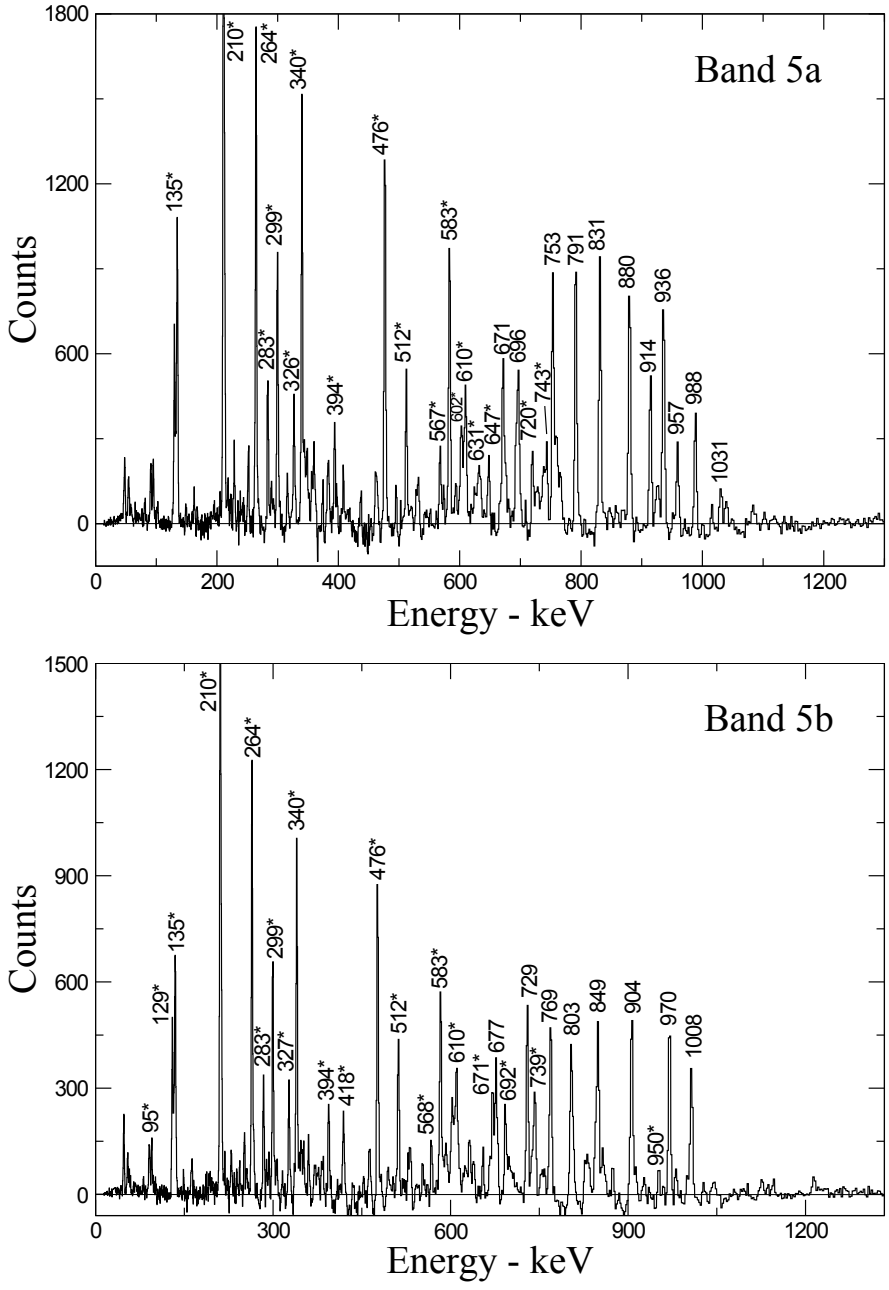

Figure 4.10: Coincidence spectra for signature partner bands 5a and 5b. For 5a this was produced through a summation of triple coincidence gates from a gatelist of all transitions above 936 keV set in double coincidence with a gatelist of all transitions below 988 keV. For 5b a gatelist of all transitions above 803 keV was set in double coincidence with a gatelist of all transitions below 849 keV. All E2 transitions belonging to another band are marked with an asterix.

observed given their low probability of occurrence. This would mean that bands 2a and 2b should possess opposite parity to that of bands 1a and 1b.

4.2.3 Bands 3a and 3b

Bands 3a and 3b are another previously identified pair of signature partner bands [1]. Both bands feed into bands 1a and 1b, a step formerly proposed to involve a change in parity. However, if we consider Fig. 4.4, we see that most of the states feeding to bands 1a and 1b decay to multiple states as opposed to the one to one feeding exhibited by bands 2a and 2b which would take place were these transitions a mixture of stretched M1/E2 and E2 transitions. Yet unfortunately due to the low statistics for these transitions it has only been possible to use angular correlation to determine that the 607 keV $14^+ \rightarrow 13^-$ transition is dipole, and as a result the true nature of the remainder of these transitions remains uncertain. There is an 855 keV currently assigned as the $30^- \rightarrow 28^-$ transition linking to a state visible to bands 3b and 5b. While the multipolarity of this transition also could not be determined, the old spin and parity assignments for bands 3a and 3b [1] would mean that this transition would be E3. Given this and the possibility that the transitions feeding from bands 3a and 3b to bands 1a and 1b are a mixture of M1/E2 and E2 transitions, the parity has been changed and the spin assignments for these bands has been increased by one. This change is supported in the later discussion on quasiparticle assignments for bands 3a and 3b.

The new transition at 474 keV has been identified decaying from the 11^- state of band 3a to the 10^- state of band 1a. For the intraband sequence of band 3a one new transition at 846 keV has been found. Based on relative intensities this has been assigned as the $31^- \rightarrow 29^-$ transition between the already known transitions at 957 keV and 890 keV. Five new transitions at 942 keV, 928 keV, 866 keV, 924 keV and 956 keV have been established for the high-spin sequence of band 3b, extending this band to 38^-. It has been determined that the former 852 keV transition (assigned by Cullen *et al* as the $29^+ \rightarrow 27^+$ transition) is likely to be an overlap of two transitions close in energy (851 keV and the 855 keV transition mentioned earlier) feeding from two structures newly identified in this

work, bands 5b and 6.

4.2.4 Bands 4a and 4b

As already mentioned, band 4a is a consolidation of what was previously believed to be two seperate band structures. With this association the signature partner band 4b was significantly extended and a total of eight new $\Delta I = 1$ transitions between bands 4a and 4b were identified. Thirteen new transitions linking these bands to bands 1a and 1b have also been observed, allowing relative bandhead energies for the bands to be established. The decay pattern for these transitions to bands 1a and 1b is similar to the corresponding transitions for bands 2a and 2b, with each state decaying only to one state rather than multiple states. Employing the same argument used for bands 2a and 2b, it is considered probable that these are are E1 transitions, which would introduce a change in parity from that of bands 1a and 1b.

One further 993 keV transition has been tentatively assigned to band 4a as a stretched E2 transition, extending the highest spin for this band to 36^+. The transitions between the four highest energy states previously associated with band 4b (728 keV, 754 keV and 789 keV) were not found to be associated with this band in this work. Instead seven new transitions identified at 676 keV, 655 keV, 735 keV, 807 keV, 872 keV, 937 keV and 976 keV have been assigned as stretched E2 transitions extending the band to the 33^+ state.

4.2.5 Bands 5a and 5b

Formerly deemed to be a decoupled band, eight of the transitions assigned to band 5a were already established in previous work and have been verified here. Three new intraband transitions (671 keV, 914 keV and 957 keV) have been identified as belonging to this structure. The $\Delta I = 2$, 671 keV transition has been assigned as feeding the lowest spin state, the band head at the 21^- state. Relative intensities appear to place the other two transitions immediately below the already known 1031 keV transition. Accordingly they have been assigned as the $39^- \rightarrow 37^-$ and $41^- \rightarrow 39^-$ transitions for 914 keV and 957 keV respectively. Excitation energies for this band relative to bands 1a and 1b have now been

determined through five new γ-ray transitions at 720 keV, 739 keV, 763 keV, 904 keV and 923 keV decaying to band 1a sequentially through two intermediate states. An entirely new signature partner band of nine transitions in sequence has been labelled 5b and a total of seventeen new interband M1 transitions between bands 5a and 5b have been identified. From new structure 5b three transitions (950 keV, 1265 keV and 1345 keV) have been observed linking this band directly to both bands 1a and 1b, alongside a 361 keV transition feeding from the 24^- state to one of the new intermediate states referred to above. Additionally, a 703 keV transition has also been identified as linking the 24^- state of band 5b to the 23^+ state of band 2a.

Band 5b has also been observed to be in coincidence with band 3b through a $30^- \rightarrow 28^-$ transition seen at 851 keV. Another transition of γ-ray energy 843 keV feeds from the 32^- state of band 5b to the 30^- state also linked to bands 3b and 6 as mentioned earlier.

4.2.6 Band 6

An entirely new structure for which six transitions have been identified at 960 keV, 1051 keV, 916 keV, 1034 keV, 1000 keV and 1028 keV. This band appears to be decoupled and is composed of five transitions in sequence. Where possible angular correlation measurements have indicated that these transitions are quadrupole in nature. The band is observed to be in coincidence with both bands 3b and 5b, with three transitions decaying from the bandhead 32^- state to the 30^- states of bands 3b, 5b and the aforementioned intermediate between these two bands. These transitions have been observed at energies 536 keV, 629 keV and 625 keV, respectively.

The 1034 keV transition is not seen in coincidence with the 916 keV transition or any of the transitions between higher energy states above it. It has therefore been assigned as a second $38^- \rightarrow 36^-$ transition.

4.2.7 Bands 7a and 7b

Most of the transitions seen in this work for Bands 7a and 7b were already known and each band has only been extended by one, bringing the highest observed state

to 38^+ and 39^+, respectively. A sequence of four relatively low intensity interband $\Delta I = 1$ transitions have been identified between bands 7a and 7b from 18^+ to 22^+. Two transitions formerly assigned as feeding from the 22^+ and 23^+ to the 21^+ state of band 8b were not observed in this work.
With the current spin assignments bands 7a and 7b become yrast above $I = 24^+$ (see Figs. 4.17 and 4.18), which is supported by the relatively high intensities of transitions within these bands. However as neither band 7a or 7b have been seen to be in prompt γ coincidence with any other structure associated with ^{156}Ho the exact bandhead energies for these bands relative to others present structures are not known. This will be discussed in further detail later in section 4.2.11.

4.2.8 Bands 8a and 8b

Previously only one transition at 738 keV had been associated with band 8a. In this work, an additional four transitions have been observed in coincidence with this transition at 708 keV, 773 keV, 848 keV and 916 keV. Based on relative intensity ratios the 738 keV transition has been reassigned from $24 \rightarrow 22$ to $26 \rightarrow 24$ and the 708 keV transition has been assigned as the transition decaying to the band head state. Given the angular intensity ratios measured for 738 keV and 773 keV, these transitions have been assumed to be $\Delta I = 2$, extending the highest spin associated with this band to 32^+. No further transitions linking this band to 7a were seen.
A total of four new transitions (739 keV, 884 keV, 965 keV and 1029 keV) were identified with band 8b and the transition previously assigned as feeding into the band head state has been reassigned in the same manner as the 738 keV transition of 8a mentioned above. These transitions have been assigned as $\Delta I = 2$, extending the band to spin 37^+. Again, no new transitions linking this band to 7b were identified. Furthermore no interband transitions between bands 8a and 8b have been found.

4.2.9 Bands 9a and 9b

Bands 9a and 9b are two entirely new structures that have identified in this work feeding to bands 2a and 2b. The primary sequence of transitions for band 9a

consists of nine transitions extending from 28^+, where shape coexistence begins, to 46^+. Four $\Delta I = 2$ transitions with energies 1094 keV, 678 keV, 583 keV and 832 keV have been observed to decay from the 32^+, 34^+, 36^+ and 38^+ states to band 2a. There is a sequence of three $\Delta I = 2$ transitions joining the 44^+ state of band 9a to the 38^+ state of band 2a, specifically: 1128 keV $44^+ \rightarrow 42^+$, 1098 keV $42^+ \rightarrow 40^+$ and 994 keV $40^+ \rightarrow 38^+$. Angular intensity ratio measurements suggest that these transitions are quadrupole in nature supporting the assigned spins. A pair of transitions are seen at 1310 keV and 1178 keV decaying from the 42^+ and 40^+ states mentioned above back into the main sequence of band 9a. A 588 keV transition has been tentatively assigned as the $32^+ \rightarrow 31^+$ transition linking band 9a to band 2b.

Band 9b has been assigned as a sequence of six $\Delta I = 2$ transitions extending from the 35^+ state to the 47^+ state, the highest spin observed for this nucleus to date. A cascade of nine transitions have been observed feeding into this band through the 39^+, 41^+ and 43^+ states. Three transitions linking this band to band 9a have been observed at 712 keV ($35^+ \rightarrow 34^+$), 644 keV ($37^+ \rightarrow 36^+$) and 348 keV (tentatively assigned as $39^+ \rightarrow 38^+$) transitions.

A single transition linking the 35^+ of band 10 to the 33^+ state of band 2b has been identified at 846 keV.

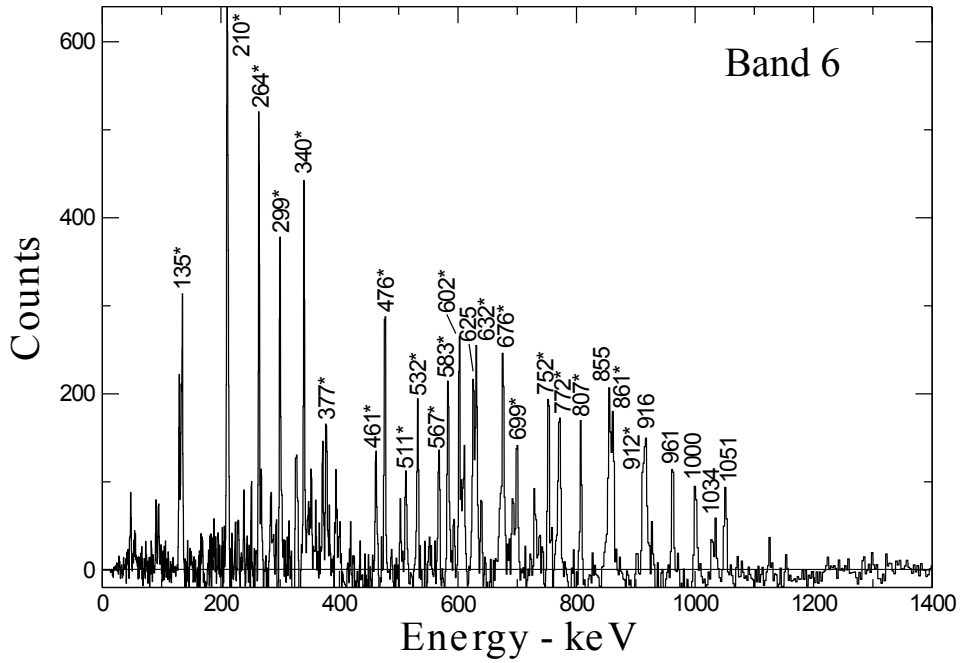

Figure 4.11: Coincidence spectra for band 6. Here the spectrum was produced through a summation of triple coincidence gates created from a gatelist consisting of all transitions in band 6, as well as the 625 keV, 629 keV, 809 keV and 855 keV preceding the band. All E2 transitions within a signature sequence are plainly labelled while all interband $\Delta I = 1$ or 2 transitions and transitions belonging to another band are marked with an asterix.

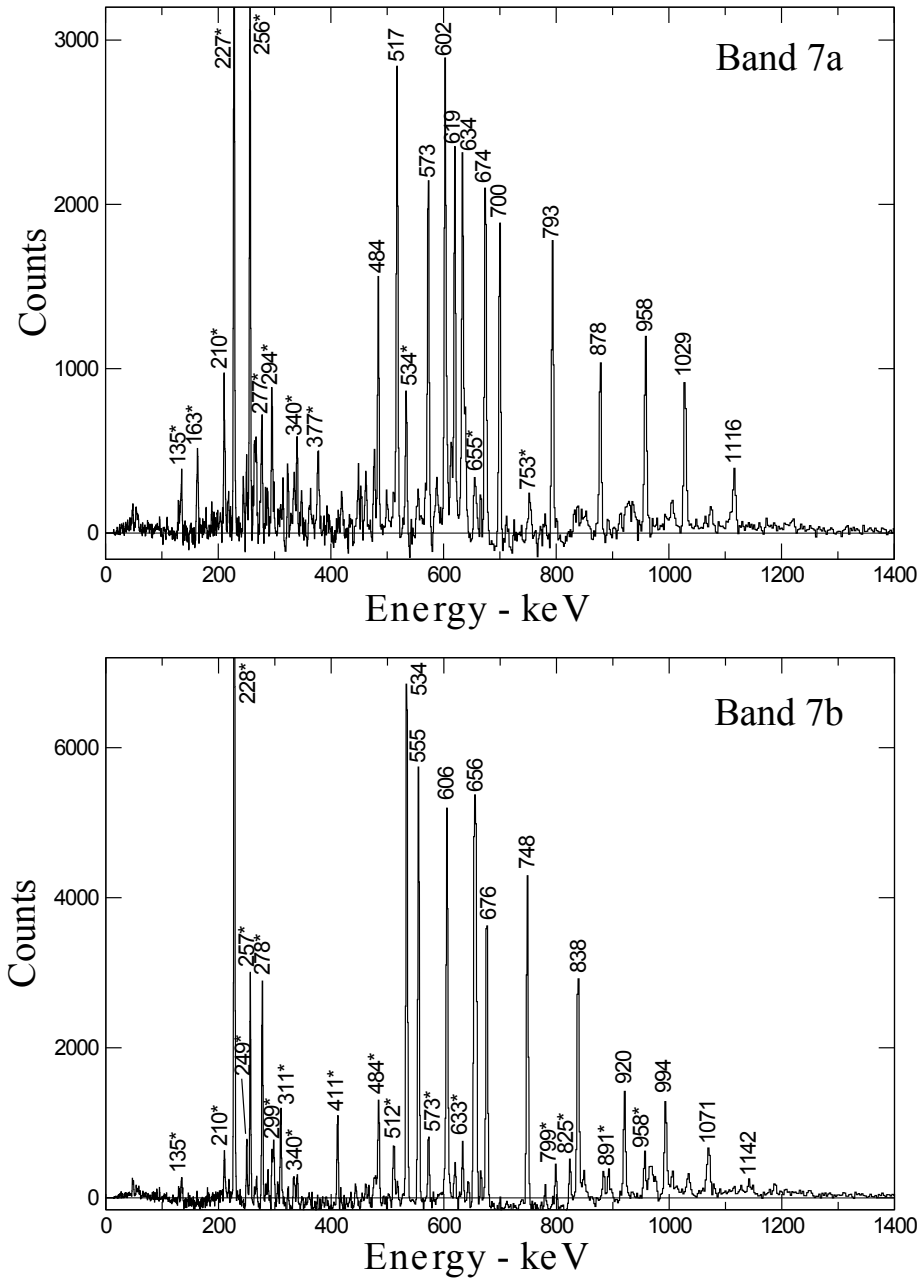

Figure 4.12: Coincidence spectra for signature partner bands 7a and 7b. The spectra were produced through a summation of triple coincidence gates whereby a gatelist consisting of the top four transitions in a band are set in double coincidence with a gatelist of all the transitions below. All transitions within a signature sequence are plainly labelled while all interband $\Delta I = 1$ or 2 transitions and transitions belonging to another band are marked with an asterix.

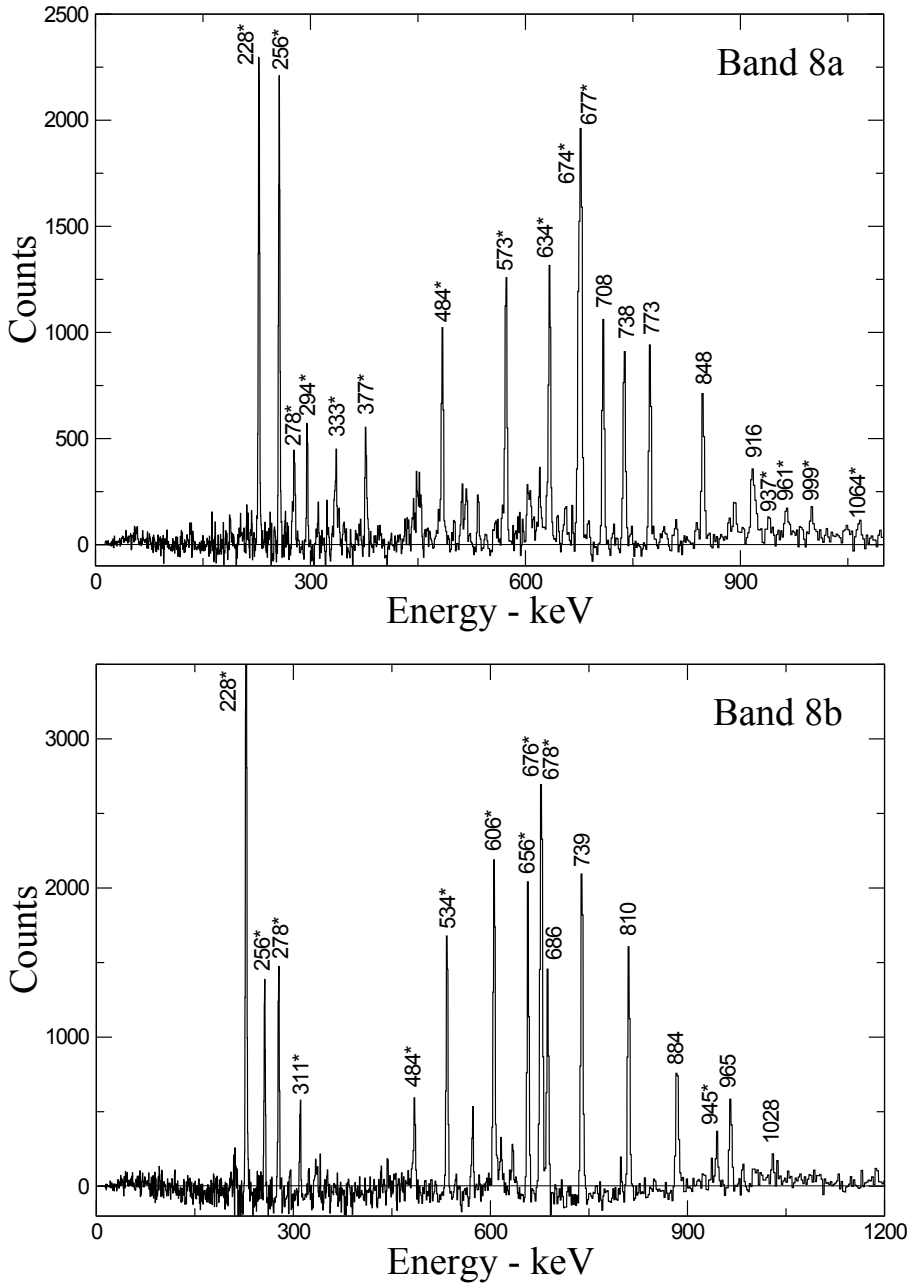

Figure 4.13: Coincidence spectra for bands 8a and 8b. The spectra were produced through a summation of triple coincidence gates whereby a gatelist consisting of all transitions in bands 8a and 8b are set in double coincidence with gatelist comprising the preceding transitions of 7a and 7b respectively. All transitions belonging to another band are marked with an asterix.

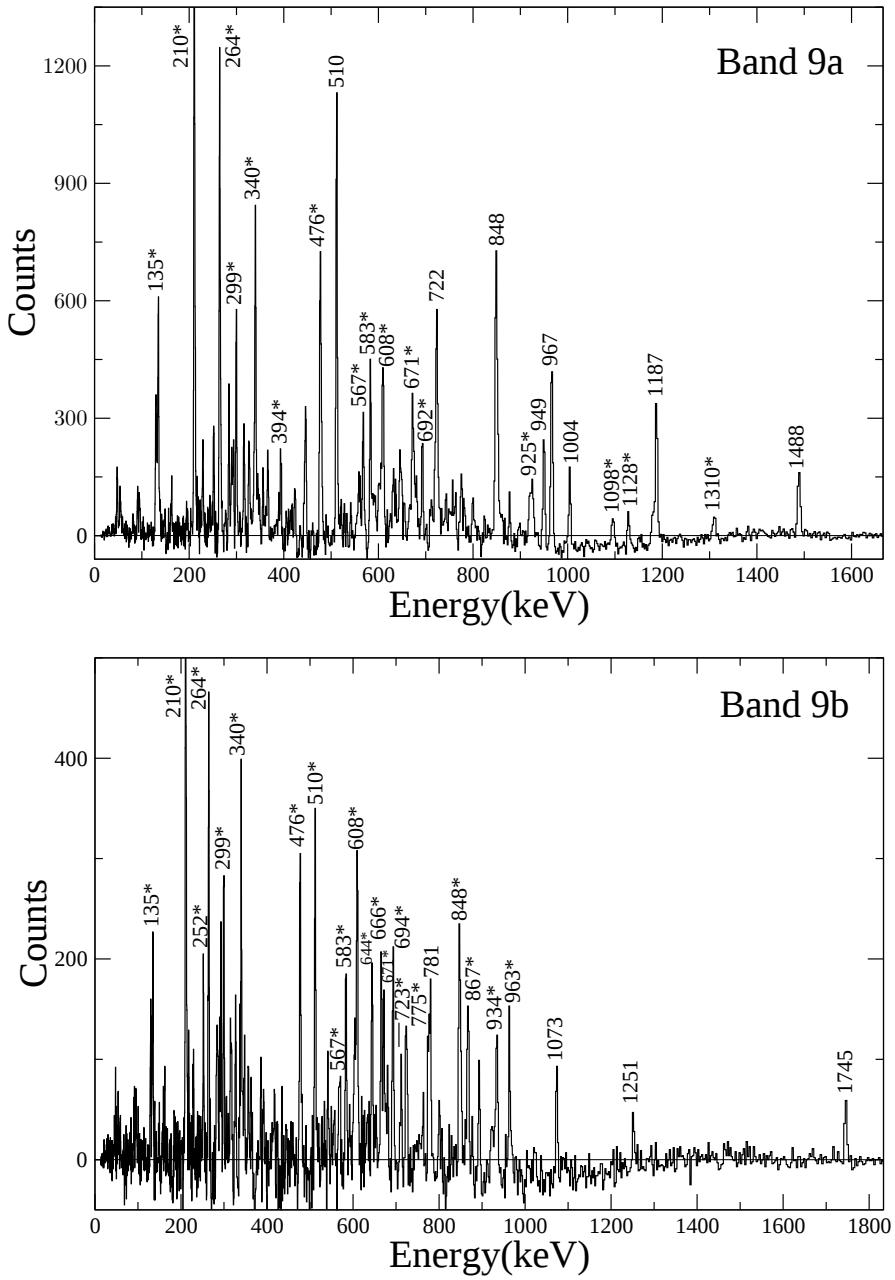

Figure 4.14: Coincidence spectra for bands 9a and 9b. The spectra were produced through a summation of triple coincidence gates whereby a gatelist consisting of all transitions in bands 8a and 8b are set in double coincidence with gatelist comprising the preceding transitions of 7a and 7b respectively.what is seen in a double coincidence gatelist of all the transitions below those used in the high excitation gatelist. All E2 transitions within a signature sequence are plainly labelled while all interband $\Delta I = 1$ or 2 transitions and transitions belonging to another band are marked with an asterisk.

4.2.10 Discussion

In order to understand the structure of the high-spin rotational bands observed in ^{156}Ho it is helpful to describe the system in terms of the quasiparticle configurations. This is done within the framework of cranked shell model calculations, as detailed in chapter 3. A good starting point in any discussion regarding quasiparticle configurations is to determine the relevant Nilsson orbitals lying close to the Fermi surface. For this, the low-spin deformation parameters for ^{156}Ho given in reference [1] have been adopted, $\beta_2 = 0.21$ and $\beta_4 = 0.02$. From summing the valence particles outside a ^{146}Gd core at this deformation (as depicted in Fig. 4.15) we can see that Nilsson orbits closest to the highest energy valence nucleons are the $h_{11/2}[523]$ K = 7/2 and $g_{7/2}[404]$ K = 7/2 orbits for protons and the $i_{13/2}[660]$ K = 1/2 and $h_{9/2}[521]$ K = 3/2 for neutrons.

These labeled orbits are consistent with the quasiparticle orbits assignments given to the most significantly represented bands in neighbouring odd-odd nuclei, ^{154}Tb [54] and ^{158}Tm [55][56], and odd-even nuclei, ^{155}Ho [9], ^{155}Dy [57] and ^{157}Er [58]. Therefore the bands with the greatest low-spin intensity in ^{156}Ho are expected to involve a combination of these quasiparticles.
The labelling convention for the quasiparticles relevant to the following discussions is the same as that used by Cullen *et al* [1] and is listed in table 4.1.

For an overview preceding discussions of the individual bands, experimental alignments (Fig. 4.16) and Routhians (Fig. 4.17) as a function of rotational frequency have been plotted for all bands bar bands 9a and 9b. Fig. 4.18 shows the excitation energies relative to a rigid rotor reference as a function of spin for all bands.

Table 4.1: Labelling convention for the quasineutron and quasiproton orbits relevant to this work.

Quasineutrons		
Label	$(\pi, \alpha)_n$	Nilsson State
A	$(+, +1/2)_1$	$i_{13/2}$ [660]1/2
B	$(+, -1/2)_1$	$i_{13/2}$ [660]1/2
C	$(+, +1/2)_2$	$i_{13/2}$ [651]3/2
D	$(+, -1/2)_2$	$i_{13/2}$ [651]3/2
E	$(-, +1/2)_1$	$h_{9/2}$ [521]3/2
F	$(-, -1/2)_1$	$h_{9/2}$ [521]3/2
X	$(-, +1/2)_2$	$h_{11/2}$ [505]11/2
Y	$(-, -1/2)_2$	$h_{11/2}$ [505]11/2
Quasiprotons		
Label	$(\pi, \alpha)_n$	Nilsson State
A_p	$(-, -1/2)_1$	$h_{11/2}$ [523]7/2
B_p	$(-, +1/2)_1$	$h_{11/2}$ [523]7/2
C_p	$(-, -1/2)_1$	$h_{11/2}$ [514]9/2
D_p	$(-, +1/2)_1$	$h_{11/2}$ [514]9/2
E_p	$(+, -1/2)_1$	$g_{7/2}$ [404]7/2
F_p	$(+, +1/2)_1$	$g_{7/2}$ [404]7/2

4.2.11 Quasiparticle Configurations

Bands 1a and 1b

With their initial alignment of $i_x \approx 7\hbar$, the low-spin yrast bands 1a and 1b possess the highest initial alignment of all the identified two-quasiparticle band structures in ^{156}Ho (Fig. 4.16). Of the Nilsson orbits expected to lie closest to the Fermi surface, the $i_{13/2}$ A and B neutron orbits carry the greatest alignment ($i_x \approx 5\hbar$), therefore it is likely that the low-spin configurations for these bands involves one of these orbitals.

The non-observation of the AB crossing, seen as a sharp gain in alignment of $\Delta i_x \approx 10\hbar$ at $\hbar\omega \approx 0.25$ in ^{157}Ho [17] and $\hbar\omega \approx 0.28$ MeV in ^{156}Dy [59] (shown in Fig. 4.21), supports this assessment as this crossing would not take place if either the A or B neutron orbital were occupied.

There is a gain in alignment of $\Delta i_x \approx 6\hbar$ at $\hbar\omega \approx 0.4$ MeV which is fairly close to the predicted crossing frequency of $\hbar\omega \approx 0.36$ MeV for both the proton A_pB_p

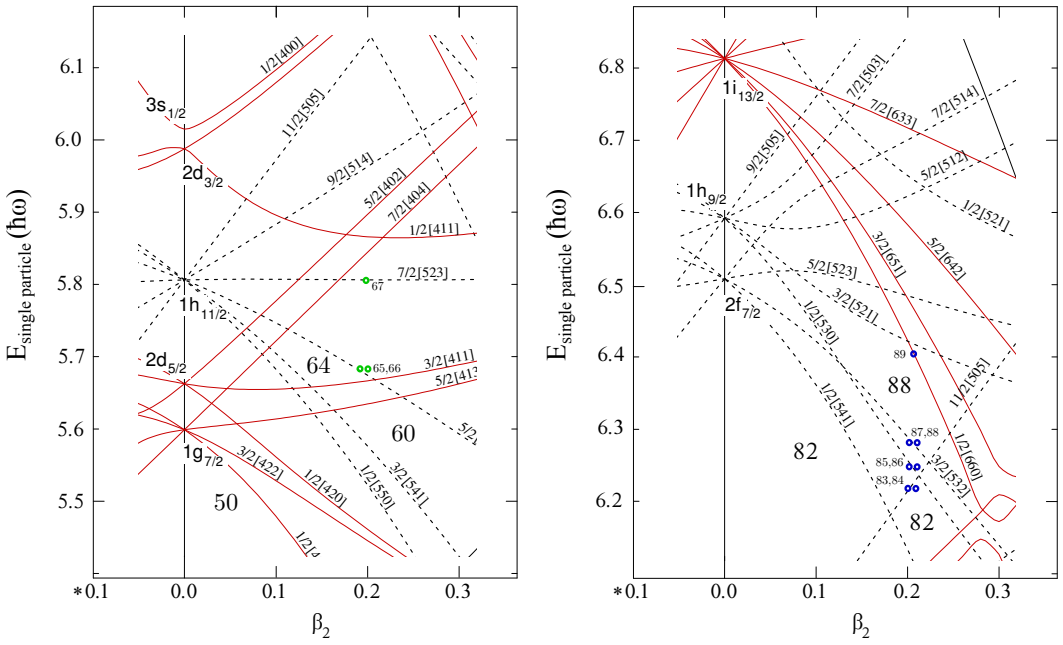

Figure 4.15: Nilsson diagrams restricted to the regions relevant to this work for protons (left) and neutrons (right). The orbitals occupied by valence particles outside the Z = 64 and N = 82 shell closures of the ^{146}Gd core are marked as green circles for protons and blue circles for neutrons.

(Fig. 3.10 in chapter 3) and neutron BC (Fig. 3.11 in chapter 3) crossings in CSM calculations assuming $\gamma = 0°$. Neither of these crossings would be blocked if the low-spin configurations consisted of the A quasi-neutron coupled to either the $g_{7/2}$ E_p or F_p quasi-protons, however the proton A_pB_p crossing typically possesses a strong interaction strength resulting in a gradual increase in alignment over a large frequency range, such as seen in ^{156}Dy [59] and ^{157}Ho [60] (demonstrated in Fig. 4.21 following the AB crossings). Such a gain is not seen for either bands 1a or 1b, which would suggest that it is the BC neutron crossing that is responsible for the gain seen, with the proton A_pB_p crossing blocked by the occupation of one of these orbitals. Therefore it is most probable that the low-spin configurations for these bands involves the A quasi-neutron coupled to the proton A_p and B_p signature partners.

While the difference between the predicted BC neutron crossing frequency of $\hbar\omega \approx 0.36$ MeV and the observed crossing frequency of $\hbar\omega \approx 0.4$ MeV is not very large, it has been found that introducing a negative value for the γ parameter

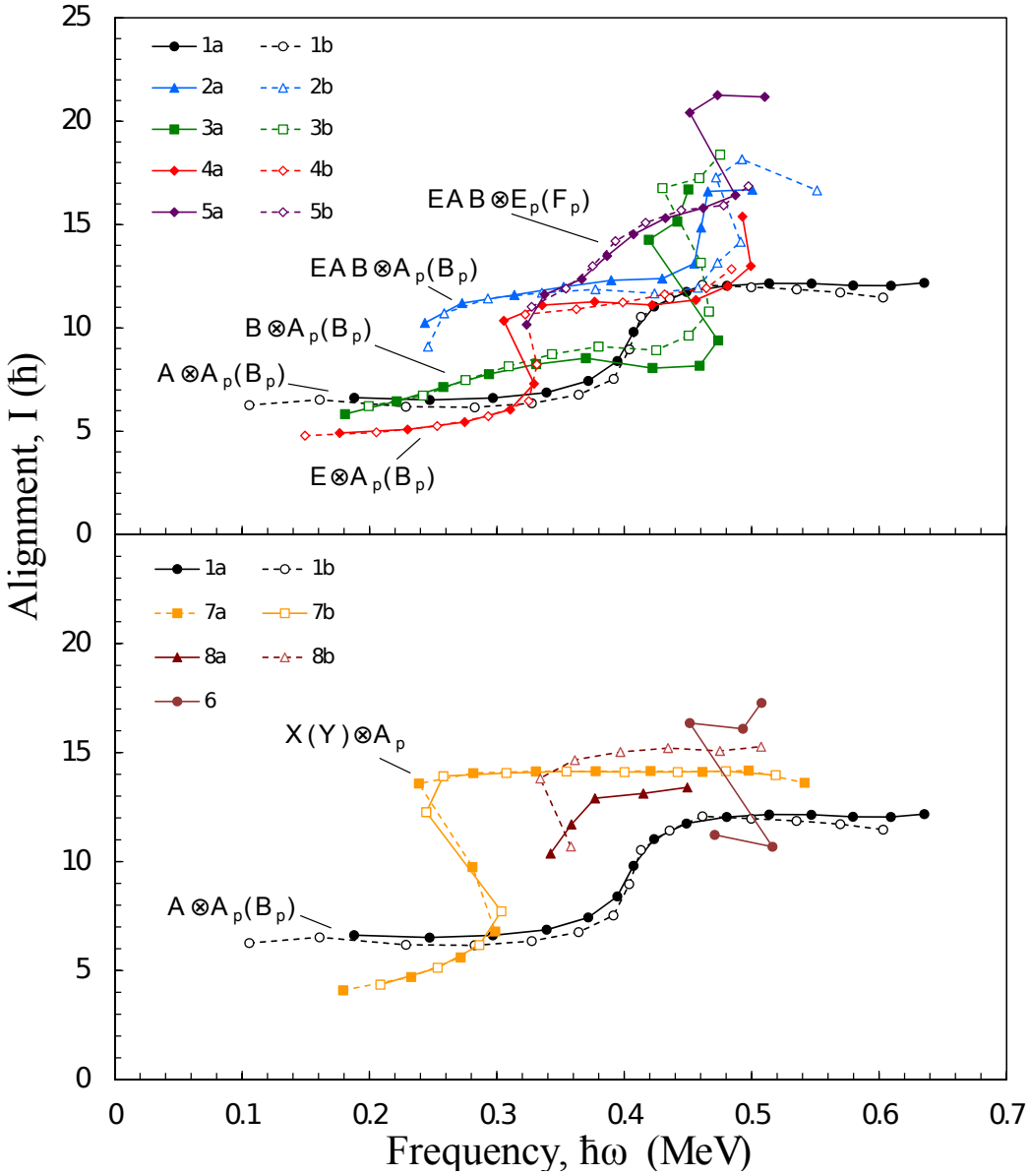

Figure 4.16: Experimental alignment, i_x, as a function of rotational frequency, $\hbar\omega$ for bands in ^{156}Ho. The $\alpha = 1/2$ and $\alpha = -1/2$ signature partners of bands 1, 2, 3, 4 and 5 are presented on top. In the bottom image the signature partners of bands 1, 7 and 8 are shown alongside the decoupled structure labelled band 6.

used for the CSM calculations much better agreement between experiment and theory may be reached. CSM calculations for e′ as a function of γ have been performed for two-quasiparticle configurations $AA_p(B_p)$, $BA_p(B_p)$ and $AE_p(F_p)$

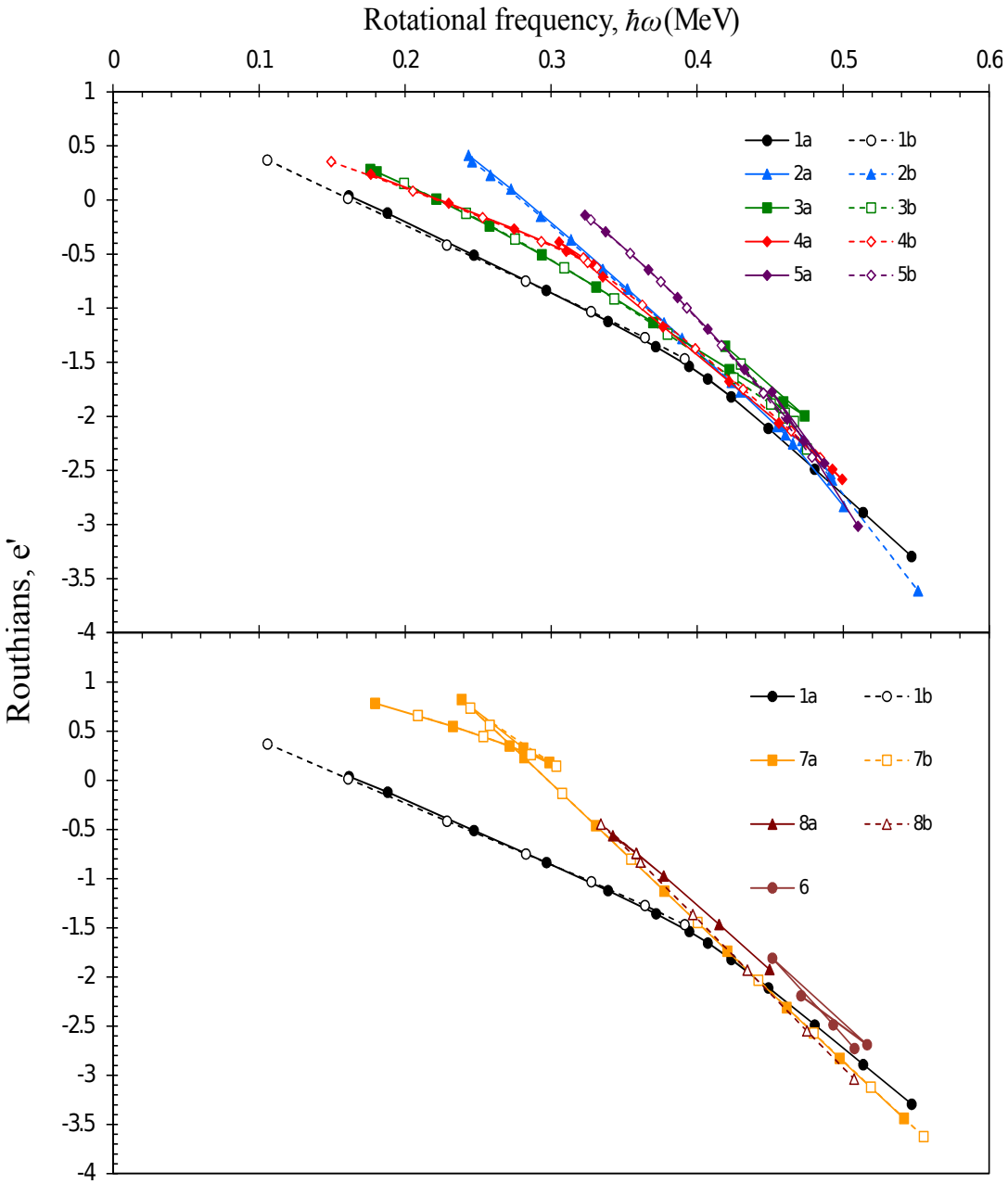

Figure 4.17: Experimental Routhians, e', as a function of rotational frequency, $\hbar\omega$ for bands in ^{156}Ho. The $\alpha = 1/2$ and $\alpha = -1/2$ signature partners of bands 1, 2, 3, 4 and 5 are presented on top. In the bottom image the signature partners of bands 1, 7 and 8 are shown alongside the decoupled structure labelled band 6.

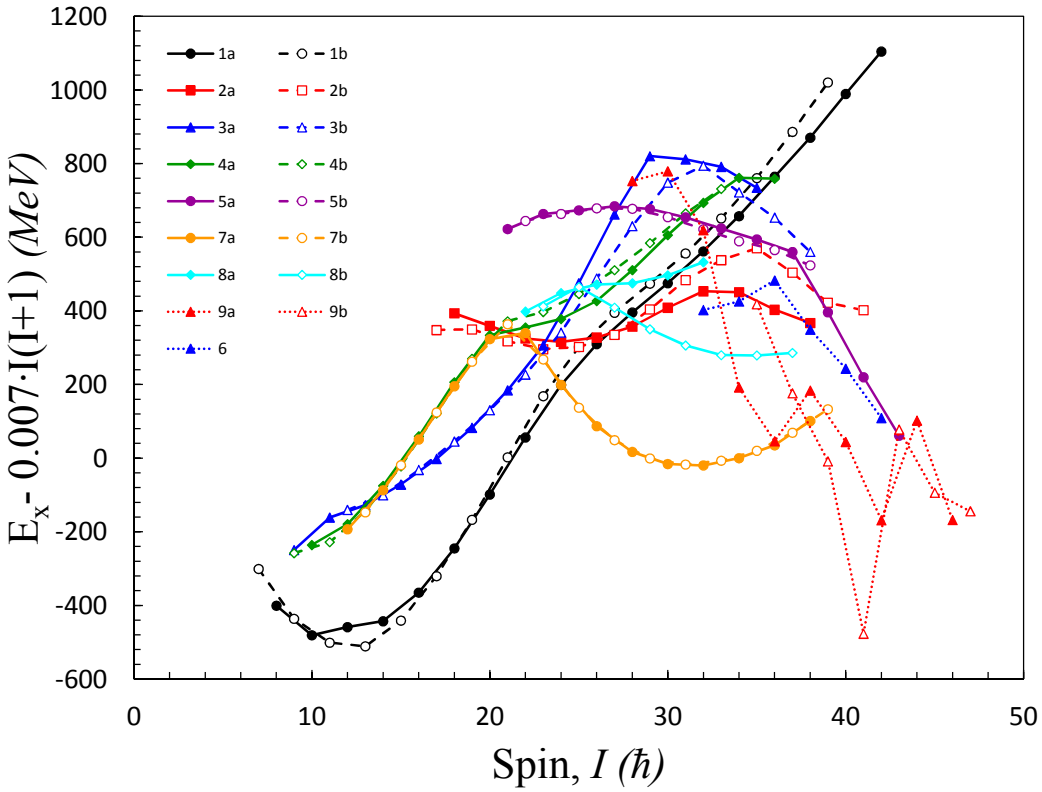

Figure 4.18: Excitation energies relative to a rigid rotor reference frame as a function of spin for all bands in ^{156}Ho.

at rotational frequencies 0.2 MeV and 0.4 MeV, which are presented in Fig. 4.19. Here it is of note that while at low frequencies the $AA_p(B_p)$ configurations are predicted to possess a potential minimum at $\gamma \approx 0°$, this minimum is seen to shift to γ = -25° at 0.4 MeV. Around this γ deformation the BC crossing is predicted to take place at $\hbar\omega \approx 0.4$ MeV (Fig. 4.20), closely matching what is seen in the experiment results.

An expanded comparison of the BC crossing systematics seen in bands 1a and 1b to BC crossings that take place in nearby odd-odd nuclei ^{154}Tb [54], ^{158}Ho [61], ^{158}Tm [55] and ^{160}Tm [62] (Fig. 4.21) shows strong similarities in the interaction strength and magnitude of gain in alignment. The exact crossing frequency of the neutron crossings have been found in previous works to be inversely related to the number of valence neutrons over an isotopic chain [54][55][63], which is consistent with the reduction in the BC crossing frequency for N = 91 Ho and

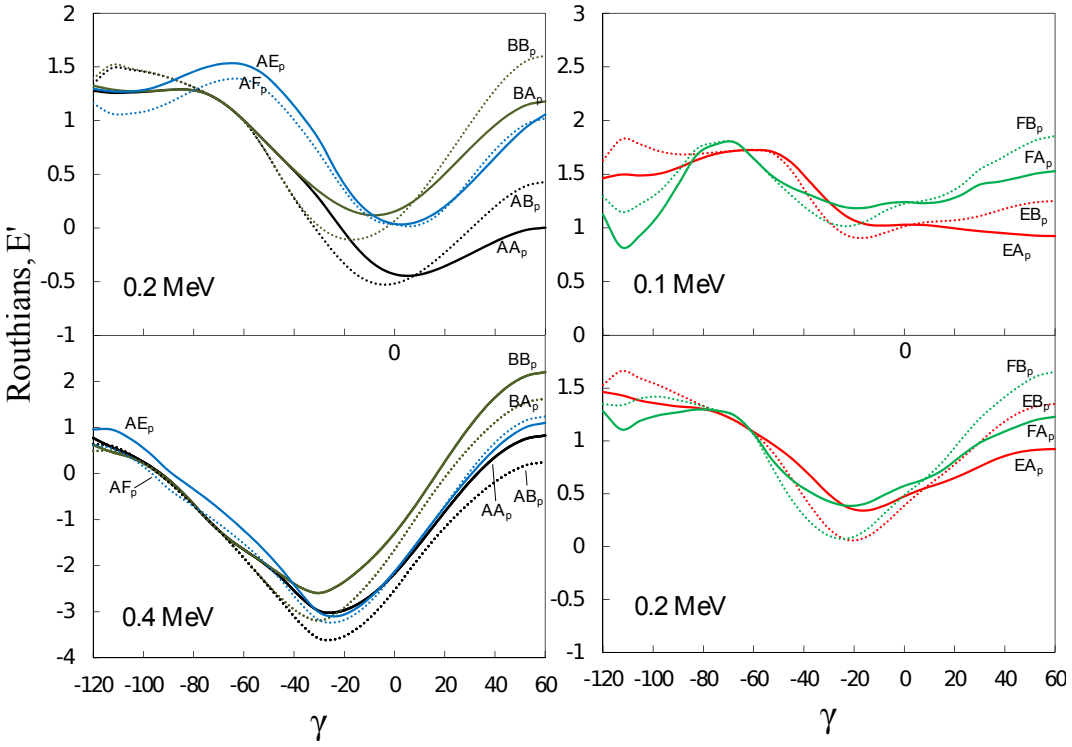

Figure 4.19: Left: E′ as a function of γ for the $AA_p(B_p)$ (black solid and dotted respectively), $BA_p(B_p)$ (olive green) and $AE_p(F_p)$ (blue) configurations at $\hbar\omega$=0.2 MeV(top) and 0.4 MeV(bottom). Right:e′ as a function of γ for the $EA_p(B_p)$ (red solid and dotted respectively) and $FA_p(B_p)$ configurations at $\hbar\omega$=0.1 MeV(top) and 0.2 MeV(bottom)

Tm isotopes relative to the N = 89 isotones, shown in Fig. 4.22.

The next expected crossing is the second proton B_pC_p crossing, predicted to take place at $\hbar\omega \approx 0.47$ MeV. This crossing is seen at $\hbar\omega \approx 0.5$ MeV for ^{158}Ho [64] and ^{160}Tm [62] in Fig. 4.21 and would not be blocked for the AA_p configuration of 1a, yet despite observing states up to $\hbar\omega \approx 0.65$ MeV no further gain in alignment takes place. The A_pD_p crossing, expected shortly after in band 1b is also not observed.

It is not known why these crossings are not seen, however it is worth noting that while the proton B_pC_p crossing seems to involve a gain in alignment of $\Delta_i \approx 7\hbar$ in ^{160}Tm the same crossing only involves a gain of $\Delta_i \approx 4\hbar$ in ^{158}Ho. The cause of this difference in gained alignment is also not known.

Considering *S(I)* as a function of I (Fig. 4.23), bands 1a and 1b both show the

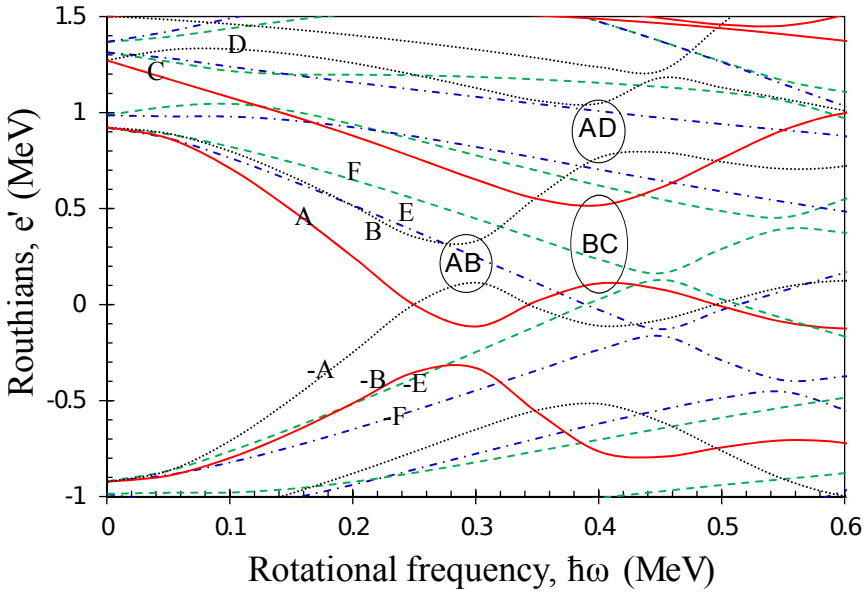

Figure 4.20: Routhian as a function of rotational frequency for neutrons when $\gamma = -20°$ with $\beta_2 = 0.210$ and $\beta_4 = 0.02$.

large signature splitting typical of a pair of bands built on proton $h_{11/2}$ signature partners and analogous bands built upon the $A_p(B_p)$ signature partners in ^{158}Ho and ^{160}Tm see strong agreement with bands 1a and 1b above the signature inversion point at $I^\pi = 19^-$. Furthermore, extracted B(M1)/B(E2) ratios for bands 1a and 1b line up well at low spins with theoretical ratios for the $AA_p(B_p)$ configuration when $\gamma = 0°$ as shown in Fig. 4.24. For the first few states there is very little signature dependence, however above $I^\pi = 18^-$ there is clear staggering between the $\alpha = 1/2$ and $\alpha =$ -1/2 signature components of band 1. Such staggering is indicative of the presence of triaxiality for these structures [65], which is consistent with the shift to negative γ deformation indicated in the CSM calculations of Fig. 4.19.

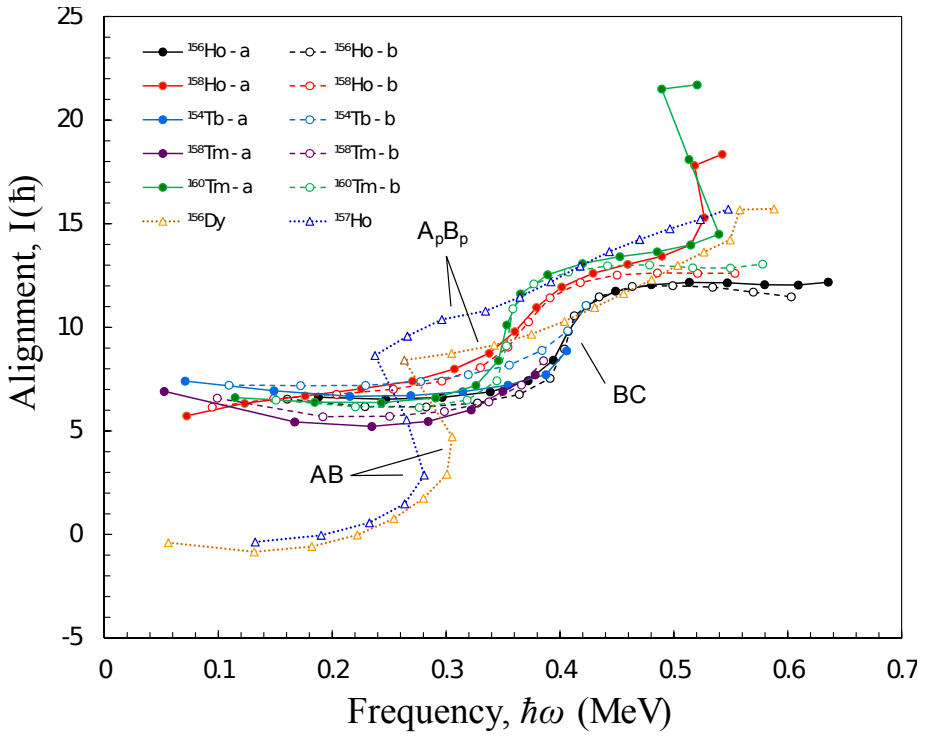

Figure 4.21: Systematics of the BC neutron crossing seen in bands built on a $h_{11/2}[523]7/2 \otimes i_{13/2}$ configuration in ^{154}Tb, ^{156}Ho, ^{158}Ho, ^{158}Tm and ^{160}Tm. To represent the AB neutron crossing and A_pB_p proton crossings bands from nearby nuclei ^{156}Dy and ^{157}Ho have been included.

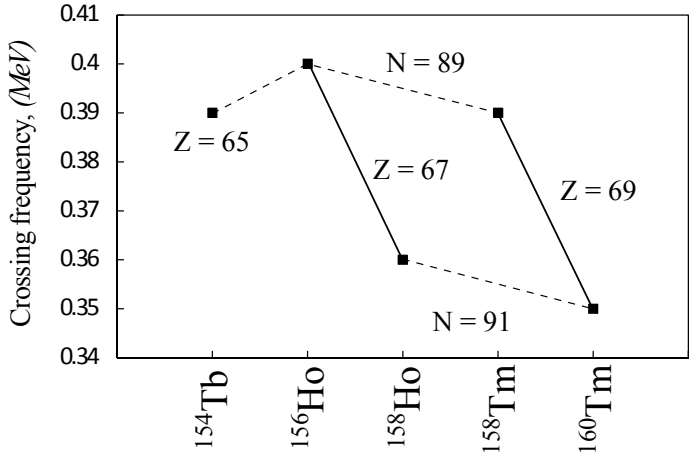

Figure 4.22: BC crossing frequency for bands built on a $h_{11/2}[523]7/2 \otimes i_{13/2}$ configuration in ^{154}Tb, ^{156}Ho, ^{158}Ho, ^{158}Tm and ^{160}Tm.

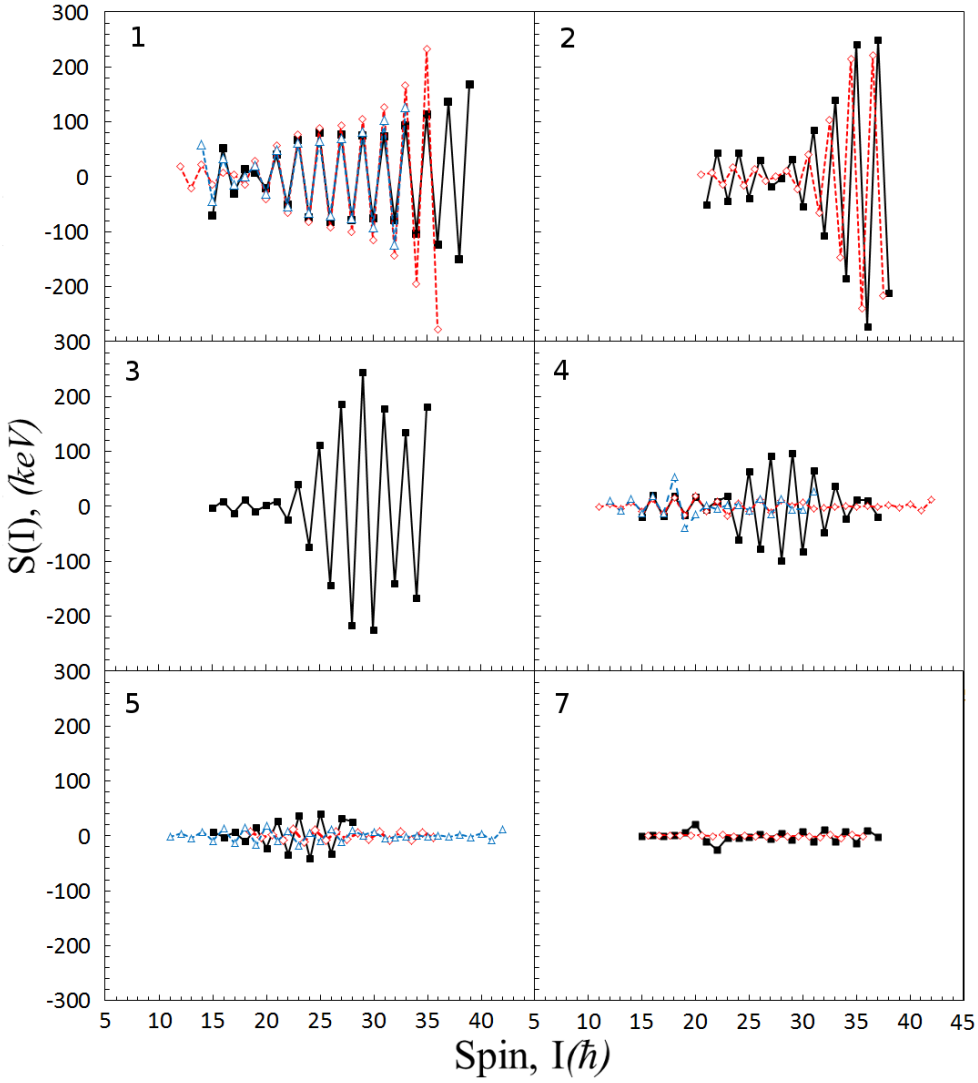

Figure 4.23: S(I) as a function of spin for bands 1, 2, 3, 4, 5 and 7 of ^{156}Ho (Black). Analogous bands in neighbouring nuclei are included for comparison, namely: Band 1, $h_{11/2}[523]7/2$ proton signature partners from ^{158}Ho (Red diamond) and ^{160}Tm (blue triangle). Band 2, $h_{11/2}[523]7/2$ proton signature partners from ^{157}Ho (red diamond). Band 4, comparisons to bands in nearby odd-odd nuclei possessing similar alignment characteristics, ^{158}Ho (red diamond) and ^{160}Tm (blue triangle). Band 5, $g_{7/2}[404]7/2$ proton signature partners from ^{157}Ho (red diamond) and ^{158}Ho (blue triangle). Band 7, $h_{11/2}[505]11/2$ neutron signature partners from ^{157}Ho.

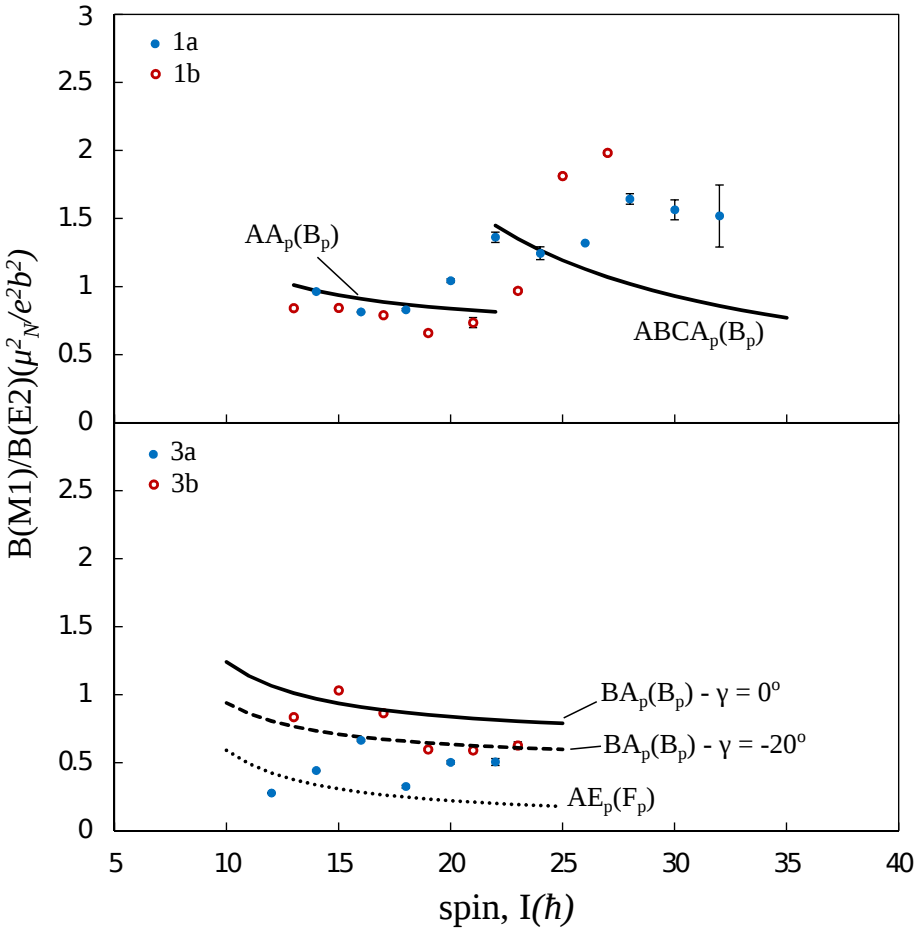

Figure 4.24: In the top plot calculated values for the B(M1)/B(2) ratios for the AA$_p$(B$_p$) and ABCA$_p$(B$_p$) configurations when $\gamma = 0°$ have been compared against the experimentally extracted ratios for bands 1a and 1b. In the bottom plot extracted values for bands 3a and 3b have been compared against calculated ratios for the AE$_p$(F$_p$) (dotted) and BA$_p$(B$_p$) (solid) configurations with $\gamma = 0°$, as well the BA$_p$(B$_p$) configuration with γ = -20° (dashed). For the theoretical values Q$_0$ was set to 5.5 eb from measurements of neighbouring isotope ^{157}Ho [16] and g$_R$ was set equal to Z/A.

Bands 2a and 2b

The high initial alignment for bands 2a and 2b of $i_x \approx 12\hbar$ implies four-quasiparticle base configuration which includes both the $i\approx 5\hbar$ A and B neutron orbitals. Indeed, the lowest states show a downturn around the expected frequency for the AB neutron crossing with $\gamma = 0°$ and seem to roughly follow on from where this

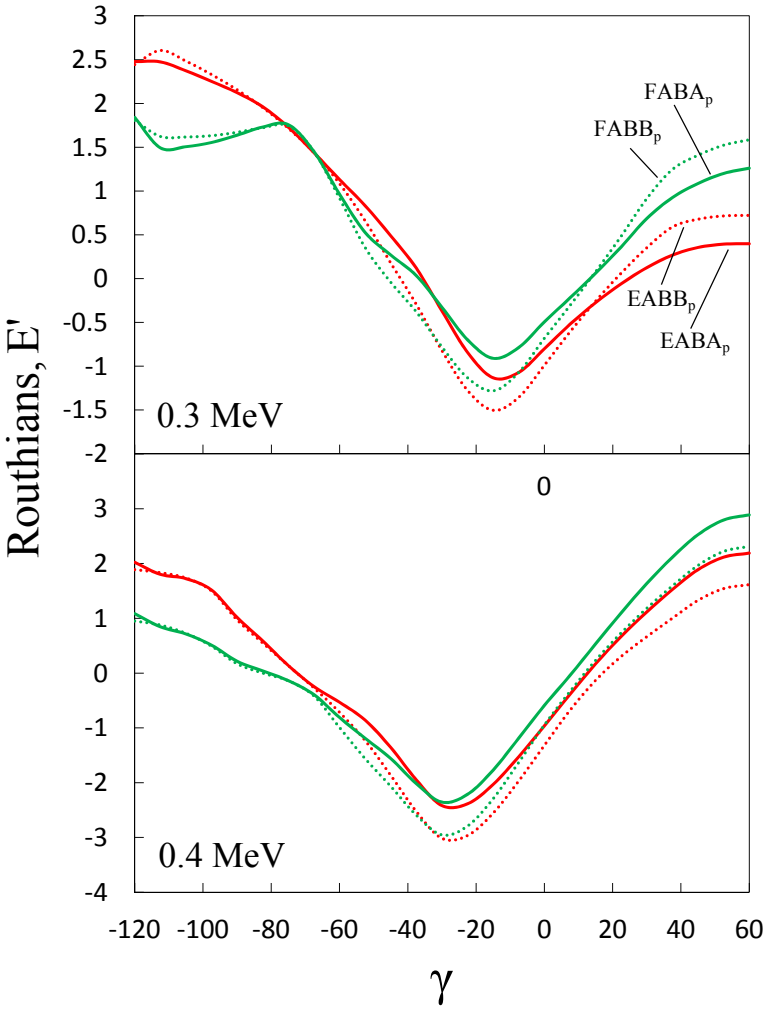

Figure 4.25: e′ as a function of γ for the EABA$_p$(B$_p$) (red solid and dotted respectively) and FABA$_p$(B$_p$) (green) configurations at $\hbar\omega$=0.3 MeV(top) and 0.4 MeV (bottom).

crossing takes place in ^{155}Ho and ^{157}Ho as seen in Fig. 4.26.

The A$_p$B$_p$ crossing is not observed, implying that at least one of the A$_p$ or B$_p$ orbitals is occupied. The next available neutron orbital lying close to the Fermi surface is the $h_{9/2}$ E quasineutron, so it is probable that bands 2a and 2b are the EABA$_p$ and EABB$_p$ configurations, respectively, as previously suggested by Cullen *et al* [1]. These configurations are consistent with the parity change implied by the feeding pattern of transitions linking these bands to the yrast bands, as discussed in section 4.2.2.

As bands 2a and 2b appear to continue on from an AB crossing it follows that

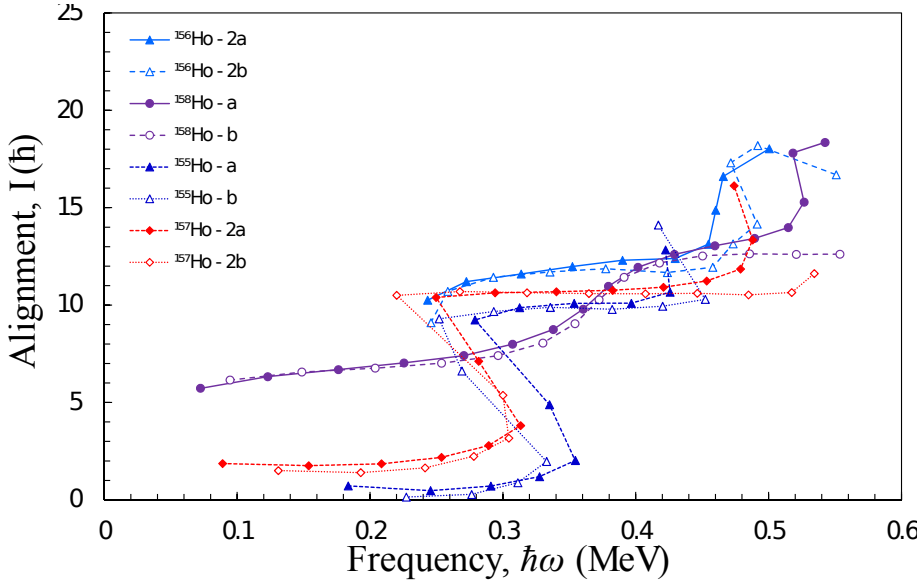

Figure 4.26: e′ as a function of $\hbar\omega$ for bands built on the $ABA_p(B_p)$ in ^{155}Ho. ^{157}Ho and ^{158}Ho alongside 2a and 2b.

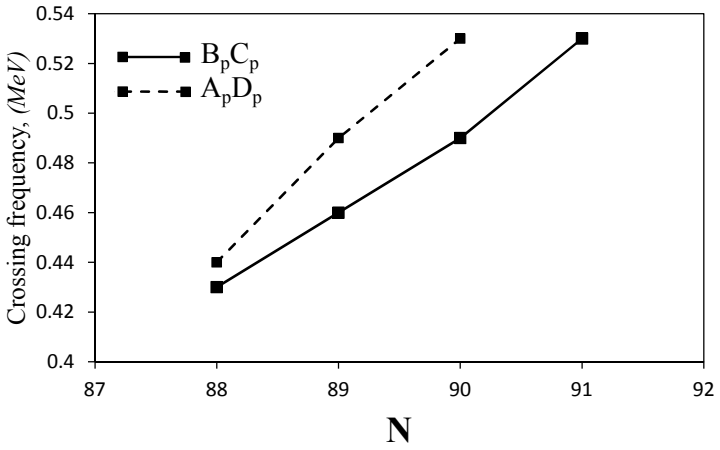

Figure 4.27: Crossing frequency as a function of neutron number for the second and third B_pC_p and A_pD_p proton crossings observe in isotones ^{155}Ho, ^{156}Ho, ^{157}Ho and ^{158}Ho. The crossing frequency can be seen to increase with the addition of valence neutrons.

there exists for these bands a pair of corresponding two-quasiparticle configura-

tions that are unfavoured, EA_p and EB_p. CSM calculations of e′ as a function γ for the $EA_p(B_p)$ and $FA_p(B_p)$ configurations are shown in Fig. 4.19. At low frequencies ($\hbar\omega \approx 0.1$ MeV) the $EA_p(F_p)$ configuration appears to possess no discernible Routhian minimum, and e′ continues to decrease up to the limit of $\gamma = 60°$. Proceeding to $\hbar\omega = 0.2$ MeV a minimum is predicted to develop at roughly γ = -20°, a value which persists for the $EABA_p(B_p)$ configurations at $\hbar\omega = 0.3$ MeV (See Fig. 4.25). This may explain why no transitions are seen for these bands until they reach a four-quasiparticle configuration.

The first directly observed gains in alignment for Bands 2a and 2b take place at $\hbar\omega \approx 0.45$ MeV and $\hbar\omega \approx 0.48$ MeV respectively (Fig. 4.26). Similar gains are seen in analogous bands from ^{155}Ho and ^{157}Ho where they were assigned as the second and third proton crossings B_pC_p and A_pD_p. It is likely that these crossings are responsible for the alignment gains seen in bands 2a and 2b as, despite non-observation of the B_pC_p and A_pD_p crossings in bands 1a and 1b, they are still predicted to occur in this frequency region. It is of note that the exact frequency at which the crossings take place appears to increase with the addition of valence neutrons (Fig. 4.27). This is consistent with previous work by Riley *et al* [63] where the same trend was observed for what has there been labelled the A_pB_p proton crossing across Erbium isotopes ^{157}Er, ^{158}Er and ^{159}Er.

As with bands 1a and 1b, the high degree of signature splitting for bands 2a and 2b following signature inversion at $I^\pi = 27^+$ is typical for bands built on the A_p and B_p proton signature partners. An analogous band involving the $ABA_p(B_p)$ three quasiparticle configurations in ^{157}Ho [66][17] is shown against bands 2a and 2b in Fig. 4.23, and above $I^\pi = 28^+$ there is strong agreement between this and and the $EABA_p(B_p)$ configuration of bands 2a and 2b.

Bands 3a and 3b

3a and 3b are seen to begin with an initial alignment of $i \approx 6\hbar$, slightly below that of bands 1a and 1b, suggesting a two-quasiparticle configuration that includes either the A or B neutron orbitals. This is supported by the non observation of the sharp $\Delta i \approx 10\ \hbar\omega$ backbend characteristic of the AB crossing.

There is a gain in alignment of $\Delta i \approx 3\hbar$ over frequency range $\hbar\omega \approx 0.20 - 0.35$ MeV, which possesses the gradual increase in alignment characteristic of the proton A_pB_p crossing. While this crossing would not be blocked for the $AE_p(F_p)$ configurations, the gain observed is small relative to the magnitude seen for this crossing in ^{156}Dy and ^{157}Ho and takes place at a lower rotational frequency than the $\hbar\omega \approx 0.36$ MeV crossing predicted by CSM calculations assuming $\gamma = 0°$.

As with the $AA_p(B_p)$ configuration, the Routhian minimum of the $AE_p(F_p)$

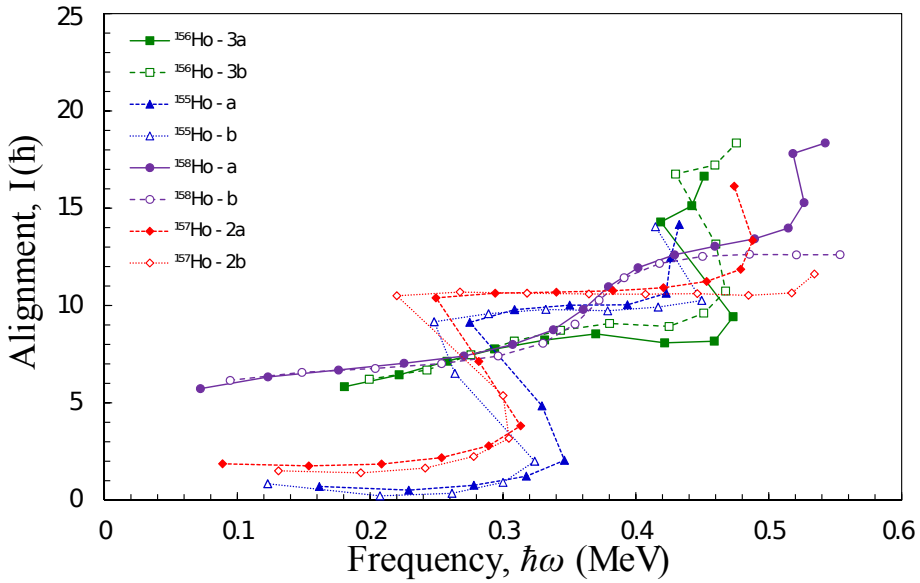

Figure 4.28: Systematics of the B_pC_p and A_pD_p proton crossings in holmium isotopes for N=88, 89, 90 and 91.

configurations shifts from $\gamma \approx 0°$ to a negative γ deformation as rotational frequency increases, reaching $\gamma \approx$ -20° by $\hbar\omega = 0.4$ MeV (Fig. 4.19). Using a negative γ parameter for CSM calculations of e′ as a function of $\hbar\omega$ the predicted crossing frequency for the A_pB_p crossing is lowered (See Fig. 4.29), however even at γ = -20° the gain in alignment observed at low frequencies for bands 3a and 3b still occurs earlier than predicted. Considering this and the small magnitude of the gain it is hard to reconcile this with the A_pB_p proton crossing.

Ruling out the A_pB_p proton crossing and considering the feeding pattern from these bands to the yrast, it is thought unlikely that the low-spin configurations of bands 3a and 3b are the $AE_p(F_p)$ configurations. This leaves the $BA_p(B_p)$

configuration as the next available two-quasiparticle configuration that involves either the A or B quasineutron orbitals.

As the B orbit would possess a lower alignment than the A orbit this would again fit with the initial alignment of bands 3a and 3b being slightly less than that of bands 1a and 1b, however the initial gain in alignment remains problematic. If bands 3a and 3b built on the $\mathrm{BA}_p(\mathrm{B}_p)$ configuration the profile of alignment as a function of rotational frequency would be expected to mirror that of the $\mathrm{AA}_p(\mathrm{B}_p)$ configurations of bands 1a and 1b, yet they do not. Considering e′ as a function of γ, it can be seen that the $\mathrm{BA}_p(\mathrm{B}_p)$ configuration is predicted to possess a Routhian minimum around $\gamma \approx -20°$ even at the lowest rotational frequencies, as opposed to the minimum at $\gamma \approx 0°$ seen for the $\mathrm{AA}_p(\mathrm{B}_p)$ configuration.

Taking this into account for calculations of theoretical B(M1)/B(E2) ratios,

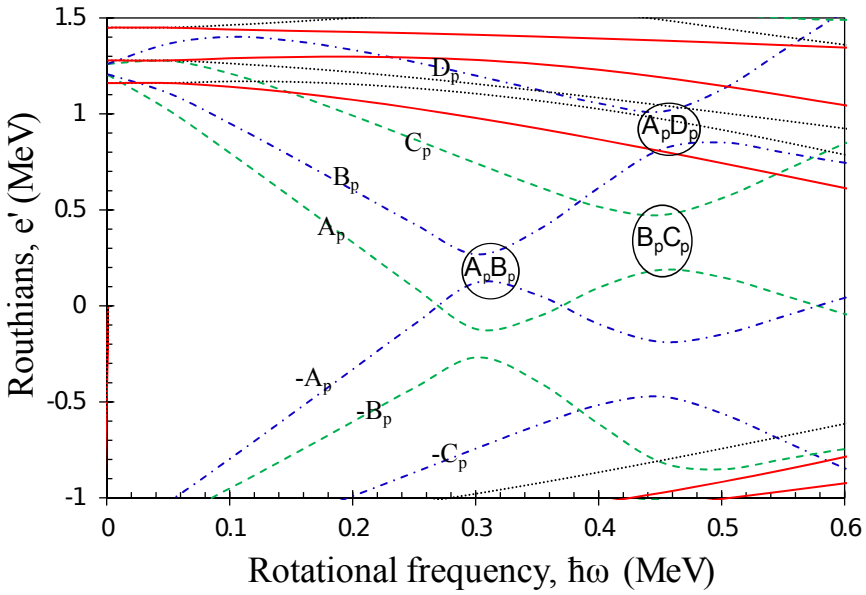

Figure 4.29: Routhian as a function of rotational frequency for protons when $\gamma = -30°$ with $\beta_2 = 0.210$ and $\beta_4 = 0.02$.

there is good agreement between the experimentally extracted low-spin ratios and theoretical values predicted for configurations involving an $\mathrm{i}_{13/2}[660]$ neutron coupled to $\mathrm{h}_{11/2}[523]$ proton signature partners at γ = -20° (see Fig. 4.24). Included for comparison are the calculated ratios for the $\mathrm{AE}_p(\mathrm{F}_p)$ configurations

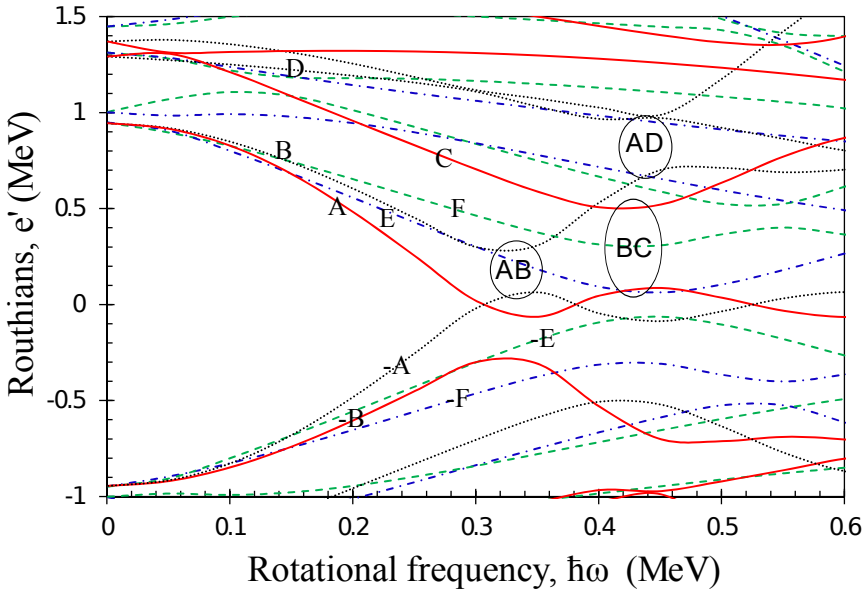

Figure 4.30: Routhian as a function of rotational frequency for neutrons when $\gamma = -30°$ with $\beta_2 = 0.210$ and $\beta_4 = 0.02$.

(dotted) and the $BA_p(B_p)$ configurations for $\gamma = 0°$ (solid).

Invoking the triaxiality argument used in the discussions on bands 1a and 1b, the presence of staggering between the signature partners of bands 3a and 3b is also supportive of the γ = -20° deformation calculated to be present in the $BA_p(B_p)$ configuration at $\hbar\omega = 0.2$ MeV.

Therefore despite the differences in alignment between bands 1a(1b) and 3a(3b) it is thought likely that the low-spin configuration of bands 3a and 3b is $BA_p(B_p)$, however the cause of the initial gain in alignment remains uncertain.

Proceeding to higher spins, after the initial alignment increase the first crossings to take place occur at $\hbar\omega \approx 0.47$ MeV where both bands undergo a sharp gain in alignment of $\Delta i_x \approx 8\hbar$. As with bands 2a and 2b, these crossings fit well with the proton B_pC_p and A_pD_p crossings (Fig. 4.28), which further supports the assessment that the A_pB_p crossing is not responsible for the early gain as both the B_pC_p and A_pD_p crossings would be blocked if it were. Still, the $\Delta i_x \approx 8\hbar$ gain in alignment is too large to be accounted for by the B_pC_p and A_pD_p proton crossings alone.

At rotational frequencies between 0.4 and 0.5 MeV the Routhian minimum for the $BA_p(B_p)$ configuration is predicted to be $\sim$ -30°. With this value for γ the BC and AD neutron crossing frequencies are predicted to be delayed until $\hbar\omega \approx 0.46$ MeV (See Fig. 4.30). Since the AD crossing would not be blocked for the $BA_p(B_p)$ configuration it is possible that this gain is a result of two crossings overlapping.

Another possibility is that the unusually large gains in aligned angular momentum seen for these crossings stems from the emergence of single-particle behaviour, which is often seen in a band approaching termination. A loss of collectivity will lead to the collapse of systematic behaviours dictated by that collectivity and thus i_x ceases to be a good indicator of the specific qualities of the quasiparticles involved relative to a collectively rotating nucleus. This is shown in Fig. 4.31 where the alignment as a function of rotational frequency for bands undergoing termination has been plotted against bands 3a and 3b.

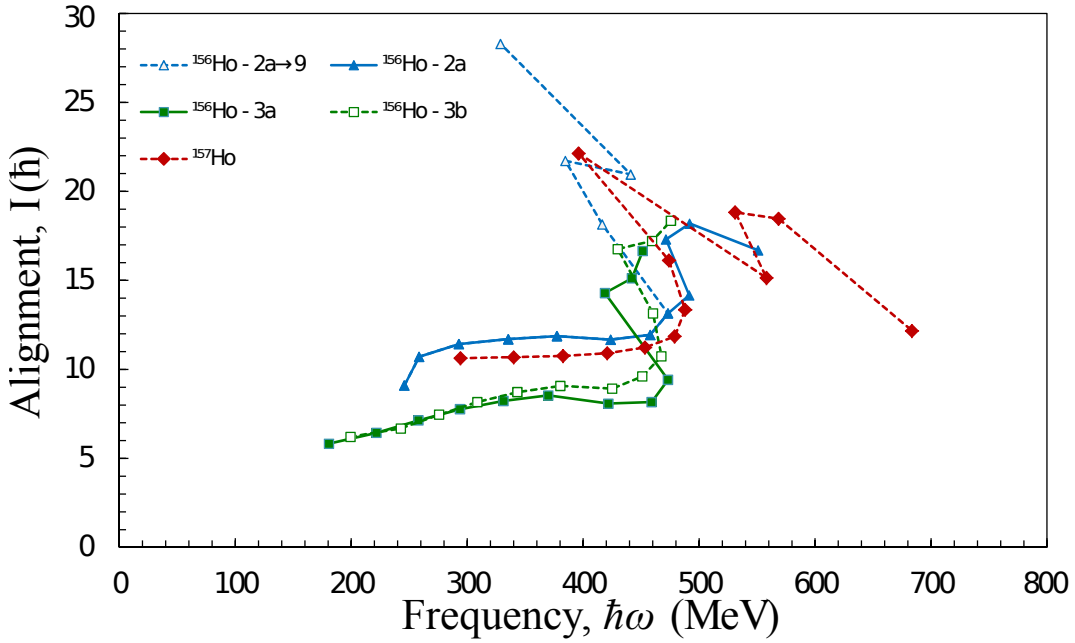

Figure 4.31: i_x as a function of $\hbar\omega$ for bands 3a and 3b of ^{156}Ho alongside terminating bands in ^{156}Ho (band 2a) and ^{157}Ho.

Unfortunately, without observing bands 3a and 3b to higher spin it is not currently possible to know whether the continued increase in alignment occurs due to such a shift from collective to non-collective or whether it is due to overlapping

alignments.
Besides the ambiguous nature of things at the top of bands 3a and 3b, there is a definitive shift from collective to non-collective behaviour seen in the form of band 6 which feeds into the 28^- and 30^- state of both bands 3b and 5b. This will be discussed in the section on band termination.
Finally the signature splitting for bands 3a and 3b shows the large splitting profile typical of signature partners built on $h_{11/2}$ protons and above the inversion point at $I^\pi = 19^-$ there is some similarity to bands 1a and 1b, although the splitting for 3a and 3b is larger.

Bands 4a and 4b

With their initial alignments of $i_x \approx 5\hbar$, the implied positive parity of these bands from the decay pattern for transitions joining bands 4a and 4b to the yrast would suggest that the low-spin configuration for these bands may be the $AE_p(F_p)$ configuration ruled out for bands 3a and 3b. Another possible positive-parity configuration for these bands could be the F neutron coupled to the $A_p(B_p)$ protons. The E quasineutron is not a likely candidate for the low-spin configurations of bands 4a and 4b as the four-quasiparticle $EABA_p(B_p)$ configuration of 2a and 2b is expected to be a continuation of the $EA_p(B_p)$ configurations after an AB crossing.

As mentioned in the discussion on bands 3a and 3b, if the low-spin configuration of bands 4a and 4b were to involve the A neutron coupled to the E_p and F_p proton signature partners respectively then the A_pB_p crossing would not be blocked and we would expect to see a gradual gain in alignment over a large frequency range centred around $\hbar\omega \approx 0.35$ MeV, however no such gain is observed.
Instead there is an unusual gain in alignment of $\Delta i_x \approx 6\hbar$ at $\hbar\omega \approx 0.32$ MeV, close to the frequency expected for the AB neutron crossing. This crossing would not be blocked for the $FA_p(B_p)$ configuration yet the gain is much smaller than that which is seen in neighbouring nuclei for the AB neutron crossing. In fact, its magnitude more closely matches that of the BC neutron crossings seen to take place at $\hbar\omega \approx 0.4$ MeV in bands 1a and 1b. Since the crossing seen in bands 4a and 4b occurs at such a low frequency it is unlikely that it is the BC crossing.

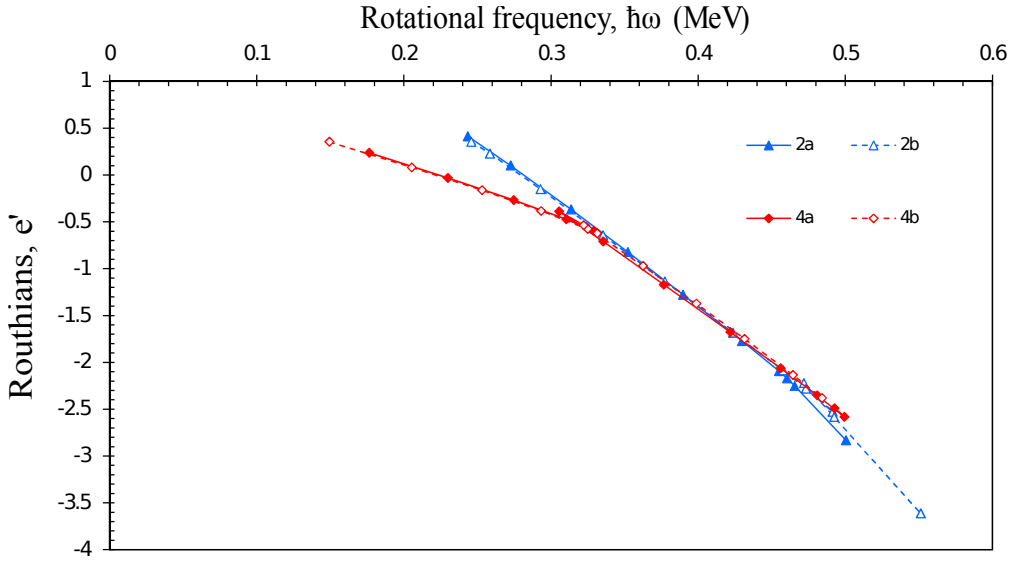

Figure 4.32: Experimental Routhians as a function of rotational frequency for bands 2a(2b) and 4a(4b).

After this unusual backbend e' and i_x as a function of $\hbar\omega$ (see figures 4.32 and

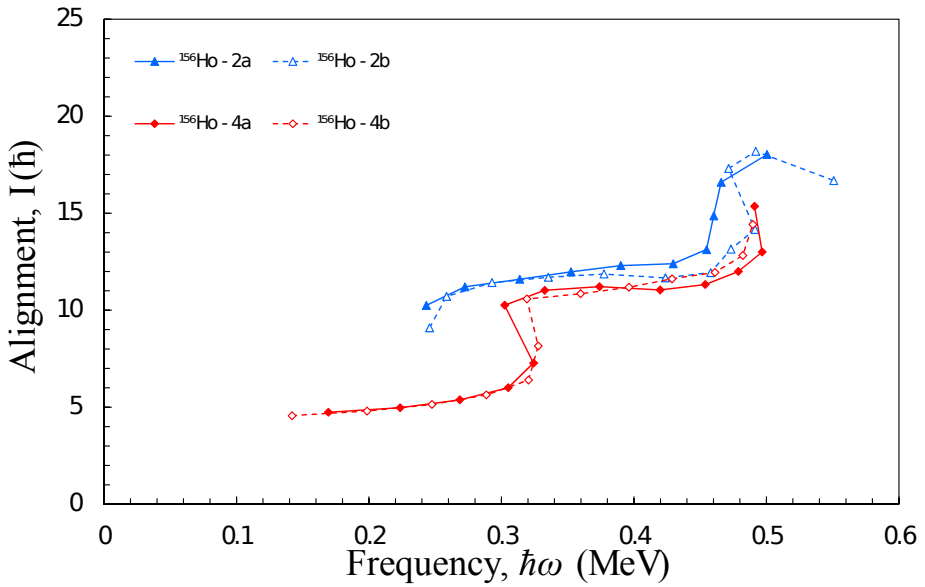

Figure 4.33: Alignment as a function of rotational frequency for bands 2a(2b) and 4a(4b).

4.33) resembles that of the positive parity EABA$_p$(B$_p$) configuration assigned to

bands 2a and 2b, which would be expected were the four-quasiparticle configurations of 4a and 4b FABA$_p$(B$_p$). Indeed, at $\hbar\omega \approx 0.5$ MeV there begins another gain in alignment for both bands, which could be the start of the B$_p$C$_p$ and A$_p$D$_p$ crossings as seen in bands 2a and 2b. However as the full crossings were not observed in this experiment it is hard to be certain of their exact nature.

One point of concern is that the initial rotational frequencies at which the four-quasiparticle configurations of bands 2a(2b) and bands 4a(4b) begin are so different. If what is seen of bands 2a and 2b are a continuation of an (as yet unobserved) AB crossing and the post backbend four-quasiparticle configurations of bands 4a and 4b are the FABA$_p$ and FABB$_p$ configurations, as indicated by the alignment and Routhian plots, then the initial rotational frequencies at which the four-quasiparticle structures of these bands begin would be expected to be close to one another. Yet there is a difference of $\sim$0.6 MeV.

If we recall from the discussion on bands 2a and 2b that e' for the EA$_p$ configuration at low rotational frequencies is predicted to continue to decrease up to the limit of $\gamma = 60°$ (Fig. 4.19), it is then of note that the FA$_p$(B$_p$) configuration possesses a shallow minimum around $\gamma \approx -20°$ at $\hbar\omega$ 0.1 MeV, which becomes deeper towards higher rotational frequencies.

It is possible that the predicted differences between the EA$_p$(B$_p$) and FA$_p$(B$_p$) configurations at low frequencies is resulting in a relative shifting of the specific rotational frequencies at which the AB crossing takes place. CSM calculations of the AB crossing frequencies when γ = -20° and 20° do indeed respectively line up well with the first observed crossing in bands 4a and 4b and the implied AB crossing preceding what is seen of bands 2a and 2b (see figures 4.34 and 4.20).

However, this does not shed any light on why the magnitude of gain in alignment for the AB crossing would be so greatly reduced relative to the same crossing in neighbouring odd-even isotopes ^{155}Ho and ^{157}Ho. A cross examination of previous work on nearby odd-odd nuclei in the mass $\approx$ 160 region has revealed similar such unusual crossings in ^{158}Ho [64][61], ^{160}Tm [62], ^{162}Tm [67] and ^{164}Lu [68], yet to date it appears that the strange nature of these analogous crossings has not been addressed. Plots of i_x against $\hbar\omega$ for ^{158}Ho and ^{160}Tm is presented alongside bands 1a(1b) and 4a(4b) of ^{156}Ho in Fig. 4.35.

For ^{158}Ho, Lu *et al* proposed that the bands that are similar to bands 4a and 4b

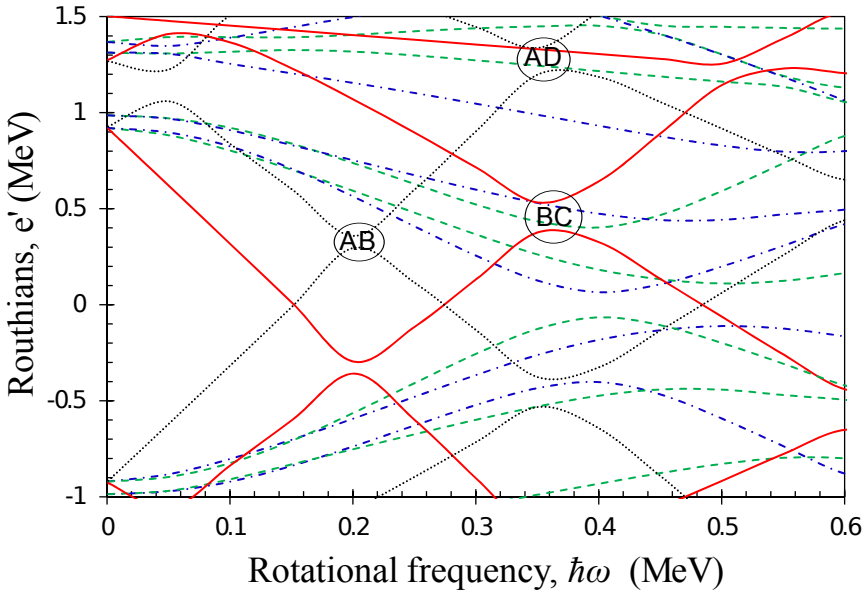

Figure 4.34: Routhians as a function of rotational frequency for neutron orbitals at $\gamma = 20°$.

of ^{156}Ho are built on the $E_p(F_p)$ signature partners coupled to an $i_{13/2}$ neutron [61], however they did not observe these bands to high enough spin to see the full backbend. A separate work by Yu *et al* observed these bands up to spins 41^+ and 42^+ however it has not been possible to obtain an interpretation of the systematics from this source.

The analogous bands in N = 91, ^{160}Tm has been interpreted by André *et al* [62] as being built on the $A_p(B_p)$ proton signature partners coupled to a $h_{9/2}$ neutron with the $\Delta i_x \approx 6\hbar$ gain attributed to the alignment of the first $i_{13/2}$ quasineutron pair, yet in neighbouring ^{159}Tm this same crossing is seen to involve a gain of $\Delta i_x \approx 10\hbar$ (see figure 4.35). Furthermore, besides bands 7a and 7b of ^{156}Ho no fully observed AB crossing possessing the typical $\Delta i_x \approx 10\hbar$ magnitude for this crossing was identified in any of the nearby odd-odd nuclei included in the cross examination. In ^{158}Ho [61] a paired structure built on the same configuration as bands 7a and 7b of ^{156}Ho has been identified however only the first few states preceding the expected AB neutron crossing were seen in that work.

In light of these observations and the lack of transitions linking bands 7a and

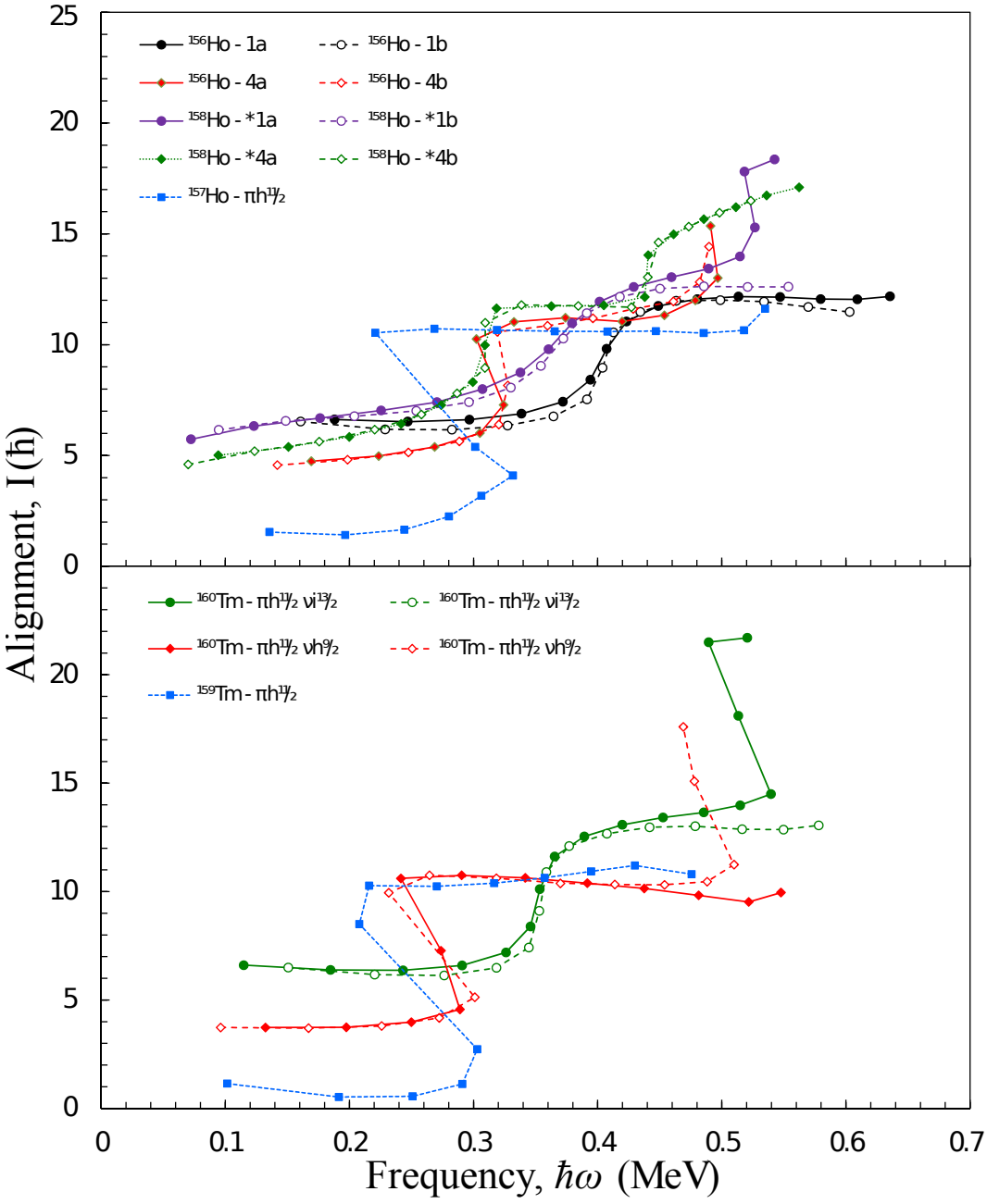

Figure 4.35: Alignment as a function of rotational frequency for ^{156}Ho (black) bands 1 (solid lines) and 4 (dashed lines) alongside counterpart bands found in ^{158}Ho (red) and ^{160}Tm (blue).

7b to the rest of the known decay scheme for ^{158}Ho, it is therefore questioned whether the anomalous backbend of bands 4a and 4b is in fact the AB crossing

but with a diminished magnitude of alignment gained relative to what is seen in neighbouring odd-even and even-even nuclei.
Another possible explanation for this band is that the unusual backbend is not actually the product of a simple alignment of a quasiparticle pair but instead arises from the low-spin configuration being crossed by a highly favoured four-quasiparticle configuration whereby the band effectively proceeds to higher spins through the exchange of one or more quasiparticles in addition to any alignment of a quasineutron or quasiproton pair. Such crossing configurations have been seen before in ^{127}Ce and ^{129}Ce [69].
In this case 4a and 4b could be the $\mathrm{AE}_p(\mathrm{F}_p)$ configurations at low-spin becoming the $\mathrm{FABA}_p(\mathrm{B}_p)$ configuration after the backbend. If we compare *S(I)* as a function of I for band 4 and the corresponding bands seen in ^{158}Ho and ^{160}Tm (Fig. 4.23) we see that there is little consistency between these bands other than at low spins. Two signature inversion points are seen for ^{156}Ho and ^{160}Tm. For ^{156}Ho the inversions occur at $I = 22$ and $I = 35$, and at $I = 19$ and $I = 24$ for ^{160}Tm. There were no inversion points seen for ^{158}Ho.
These inconsistencies may be expected if these bands are indeed examples of crossing configurations across multiple nuclei, whereas the strong similarities at low spin would suggest that all three nuclei possess the same low-spin signature partners for these bands. The fairly large signature splitting after the first inversion for ^{156}Ho supports the 4 quasiparticle configurations for bands 4a and 4b involving the $\mathrm{A}_p(\mathrm{B}_p)$ signature partners although it is noted that bands 4a and 4b exhibit a considerably smaller signature splitting than 2a and 2b.
Ultimately bands 4a and 4b represent an interesting signature pair that exhibit a number of unusual properties. A final conclusion has not been drawn with respect to the low-spin quasiparticle assignment of these bands and instead two possible interpretations are presented. It is felt that the nature of these structures in odd-odd nuclei in the mass 160 region merits further investigation.

Bands 5a and 5b

As with bands 2a and 2b, the large initial alignment of $i_x \approx 10\hbar$ suggests that bands 5a and 5b begin with a four-quasiparticle configuration. This alignment is

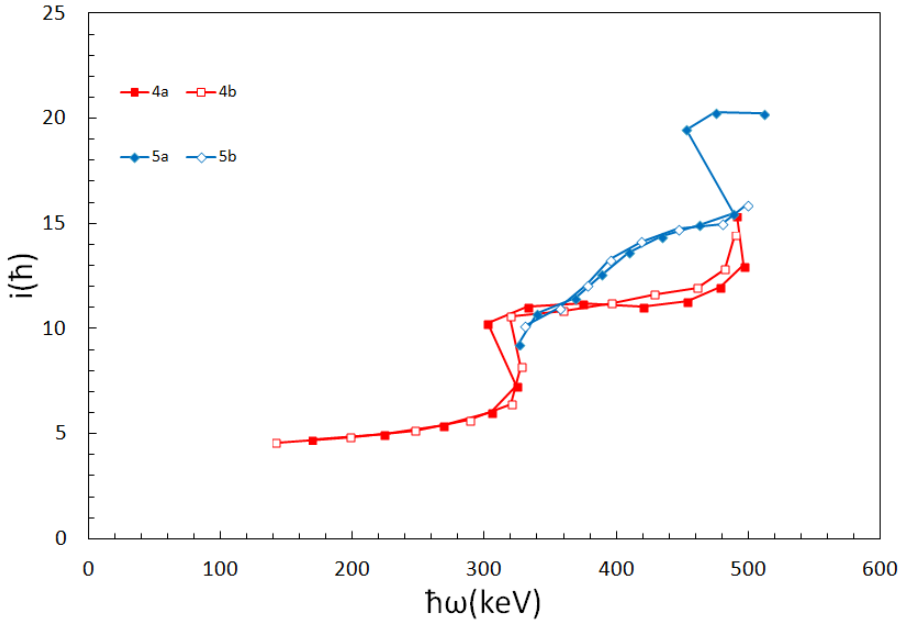

Figure 4.36: Alignment as a function of rotational frequency for bands 4a and 4b (red) alongside bands 5a and 5b (blue).

only slightly less than the initial alignment of bands 2a and 2b, as well as that of bands 4a and 4b after the first backbend, which would suggest that the low-spin configuration for these bands may be the EAB neutrons coupled to the E_p and F_p quasi-protons.

At the lowest observed rotational frequencies for bands 5a and 5b ($\hbar\omega \approx 0.32$ MeV) these bands seem to follow on from the first backbend in 4a and 4b (See Fig. 4.36). It is possible that bands 5a and 5b are continuing on from some unobserved AB crossing as is suggested for bands 2a and 2b. The frequency of this implied AB crossing matching the frequency of the first gain in alignment seen for 4a and 4b would be consistent if the predicted γ deformation for these bands match.

Total Routhians (E′) as a function of γ for the $EE_p(F_p)$ configurations and the $EABE_p(F_p)$ configurations are shown in Fig. 4.37. At low frequencies the $EE_p(F_p)$ configuration does not possess the continued downslope with increasing γ proposed to be responsible for an early AB crossing preceding what is seen in bands 2a and 2b. Instead there is a shallow minimum around $\gamma \approx -20°$, which is con-

sistent with the interpretation that what is seen for bands 5a and 5b is preceded by an AB crossing.

There is a gradual gain of $\Delta i_x \approx 7\hbar$ over the range $\hbar\omega \approx 0.35$ MeV to

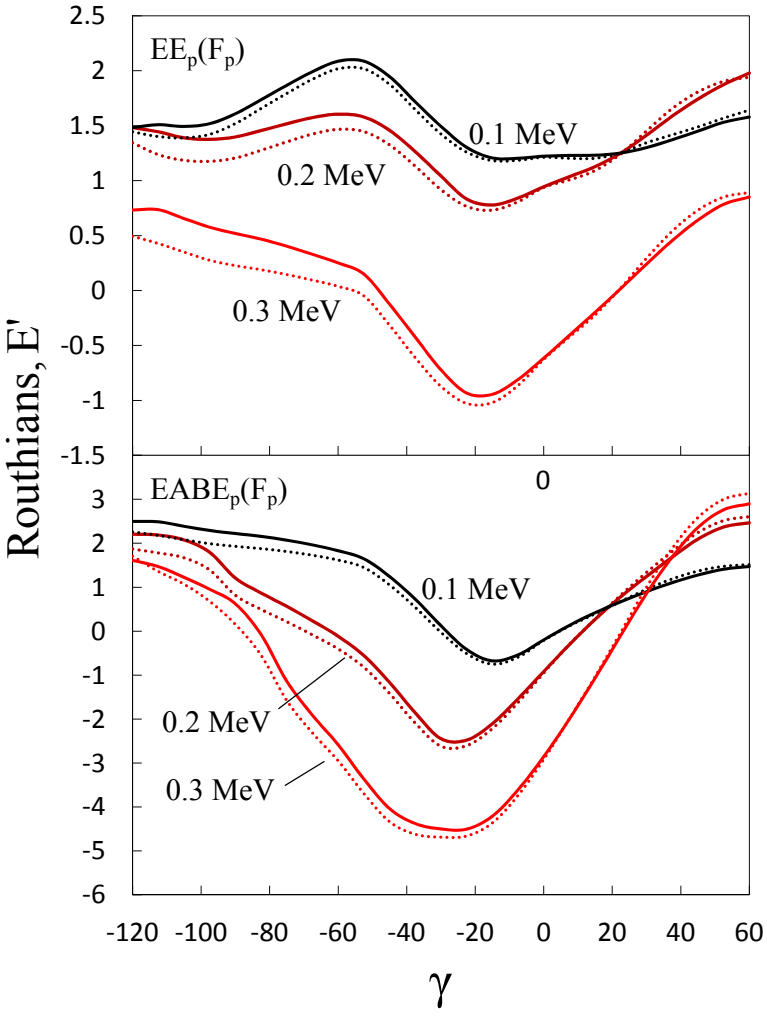

Figure 4.37: Routhians as a function of γ for the EE$_p$(F$_p$) (top) and EABE$_p$(F$_p$) configurations (bottom).

$\hbar\omega \approx 0.45$ MeV which fits well with the first proton A$_p$B$_p$ crossing. This thus implies that these proton orbits are not occupied and the next available proton orbit is instead involved in the low-spin configuration. This supports the interpretation of bands 5a and 5b as being built on a configuration that includes the the E$_p$ and F$_p$ protons.

The next gain in alignment takes place in 5a as a sharp $\Delta i_x \approx 5\hbar$ backbend at $\hbar\omega \approx 0.5$ MeV, close to the B_pC_p crossing seen in 2a and 3a however as both the proton A_p and B_p orbits are now occupied following the A_pB_p crossing, the B_pC_p crossing would be blocked. The second and third neutron crossings, BC and AD, would also be blocked by the occupied A and B neutrons, so it is considered probable that this is another example of the beginning of a shift from collective to non-collective rotation for this nucleus.

The values for the calculated ratios of reduced transition probabilities for the $EABE_p(F_p)$ configuration are quite low for a four-quasiparticle configuration, which compares fairly well with the low values of the experimentally extracted ratios for bands 5a and 5b (shown in Fig. 4.38). Furthermore, while signature splitting for these bands is fairly large compared to that of $E_p(F_p)$ signature partner bands found in nearby isotopes ^{157}Ho and ^{158}Ho it is still considerably less than that seen for those bands which involve the $A_p(B_p)$ signature partners.

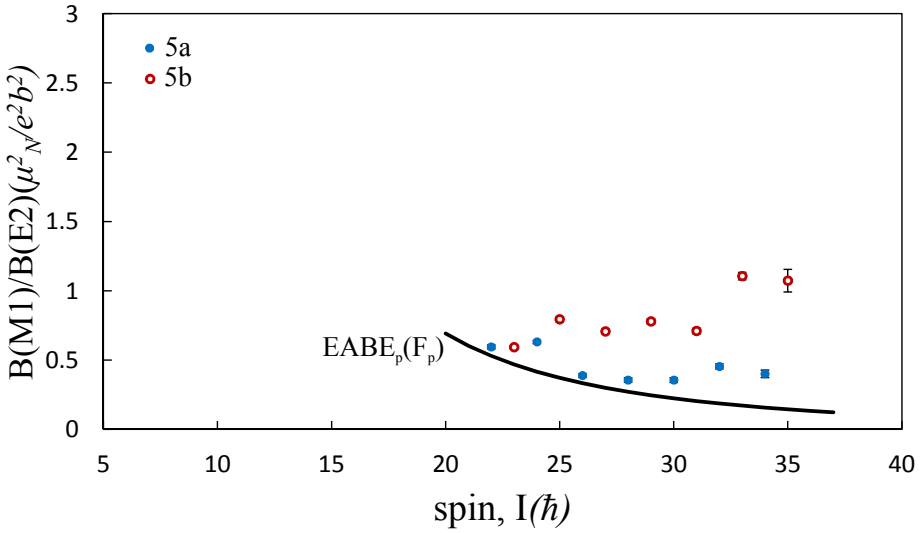

Figure 4.38: Extracted B(M1)/B(E2) ratios for bands 5a and 5b have been compared against calculated ratios for the $EABE_p(F_p)$ configurations. For the theoretical values Q_0 was set to 5.5 eb and g_R was set equal to Z/A.

Bands 7a and 7b

Bands 7a and 7b were originally identified and associated with ^{156}Ho by Waddington *et al* [70]. The initial alignment of $i_x \approx 4\hbar$ is the lowest alignment of all two-quasiparticle configurations identified in ^{156}Ho, making it unlikely that these bands involve either the A or B neutron orbitals. Indeed both bands are seen to undergo an alignment gain of $\Delta i_x \approx 10\hbar$ at $\hbar\omega \approx 0.28$ MeV mirroring the AB crossing seen in ^{157}Ho. The A_pB_p proton crossing is not observed for either band, therefore the low-spin configuration must involve either the A_p or B_p proton orbitals. However, as with bands 1a and 1b the second or third proton crossings are not seen here (see Fig. 4.16). Signature splitting for these bands is very

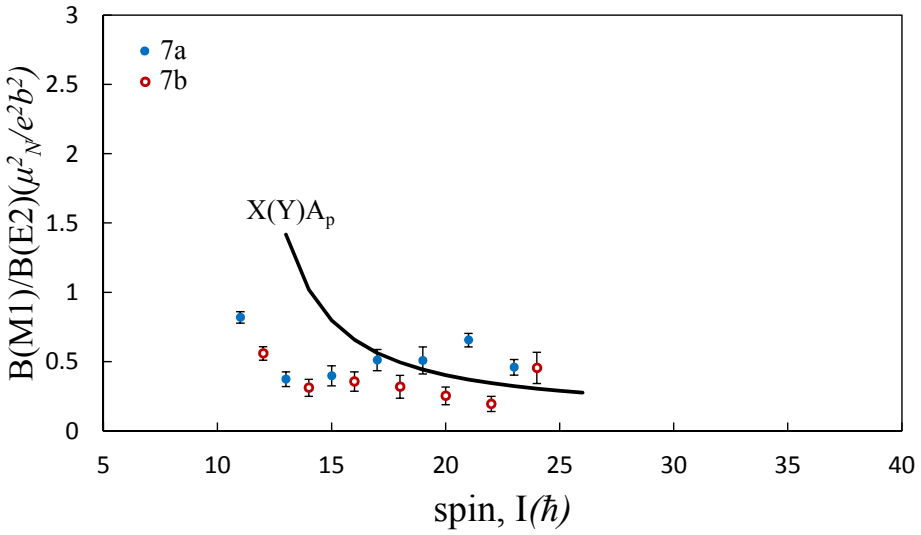

Figure 4.39: Extracted B(M1)/B(E2) ratios for bands 7a and 7b have been compared against calculated ratios for the X(Y)A_p configurations. For the theoretical values Q_0 was set to 5.5 eb and g_R was set equal to Z/A.

small, which is consistent with bands built on the $h_{11/2}$ [505] K = 11/2 X and Y neutron signature pair in ^{155}Dy [57] and ^{157}Ho [17]. In neighbouring odd-odd isotope ^{158}Ho another very similar paired structure is proposed to be built on the XA_p and YA_p configurations [61]. Comparing theoretical B(M1)/B(E2) ratios for these configurations with the extracted values for bands 7a and 7b, shown in Fig. 4.39 does show some consistency, however there is a notable exception seen in the point at which an upturn takes place at low spins, with the predicted

upturn taking place at higher spins than observed.
Another similarity to the bands built on these signature partners in ^{158}Ho lies in the non-observation of any transitions joining this band to the ground state. The cause for this absence of observed interband γ transitions is proposed by Lu *et al* [61] to be the existence of a long-lived low-lying isomeric state resulting from the X(Y)A$_p$ bands possessing a K value quite different to that of the other two-quasiparticle configurations present. This is possibly a consistent explanation for the lack of any transitions seen to link bands 7a and 7b to the rest of the ^{156}Ho decay scheme as all of the currently observed two-quasiparticle configurations possess a K of 4 whereas K for the X(Y)A$_p$ configuration is 9. This non-observation of interlinking transitions does mean that the spin assignments for bands 7a and 7b relative to the rest of ^{156}Ho are not known. This may explain the discrepancy between the predicted and experimentally extracted B(M1)/B(E2) ratios as the chosen spin values could simply be wrong. Still, given the behavioural consistencies with what is observed in nearby nuclei it is thought likely that bands 7a and 7b are the XA$_p$ and YA$_p$ configurations, respectively.

To return to the earlier discussion regarding bands 4a and 4b, as no transitions linking this band to the rest of the decay scheme have been identified, it may be that bands 7a and 7b do not belong to ^{156}Ho. If bands like 4a and 4b and the similar bands seen in other odd-odd nuclides within the mass $\sim$160 region do represent a systematic of relative reduction in the gain in alignment associated with AB neutron crossings, then the $\Delta i_x \approx 10\hbar$ AB crossing of bands 7a and 7b would potentially be the incongruity.
Indeed, the initial alignment of $i_x \approx 14\hbar$ for the four-quasiparticle X(Y)ABA$_p$ configurations are notably greater than any other four-quasiparticle configuration present, which would not be expected considering the low i_x of the X and Y neutron orbits relative to the A(B) or E(F) neutron orbits. The XABA$_p$ configuration should possess a lower alignment than the ABCA$_P$ configuration or the EABA$_p$ configuration. However without differentiating the populations of nuclides produced in the experiment via techniques such as mass spectroscopy the true source of the structures labelled bands 7a and 7b remains uncertain in this work.

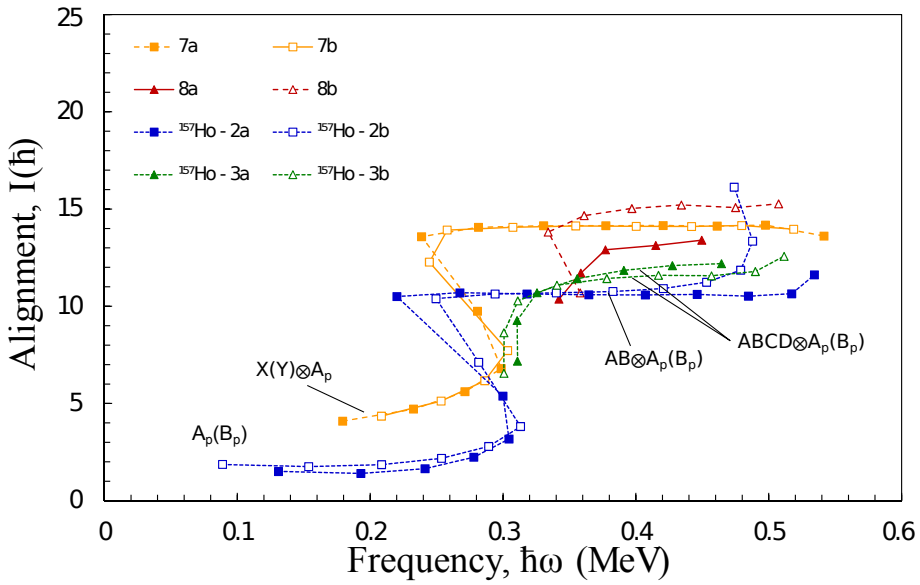

Figure 4.40: Alignment as a function of rotational frequency for bands 7a(7b) and 8a(8b). Bands from ^{157}Ho proposed to involve two-quasiparticle AB neutron crossings (dark blue squares) and four-quasiparticle ABCD neutron crossings (green triangle) in reference [17] are presented for comparison.

4.2.11.1 Bands 8a and 8b

Bands 8a and 8b feed into Bands 7a and 7b respectively, and it was suggested by Cullen *et al.* that these are continuations of the XA_p and YA_p configurations, which then undergo the BC crossing. In Fig. 4.41 excitation energies relative to a rigid rotor reference have been plotted against spin for bands 7a(7b) and 8a(8b). At $I^\pi = 20^+$ there is a sharp downwards slope for bands 7a and 7b, which indicates that spin is being gained with increaasing efficiency. This corresponds with the beginning of the AB crossing seen for these bands (Fig. 4.40). Bands 8a and 8b seem to continue onwards past this downslope until $I^\pi = 25^+$ at which point the slope of band 8b is seen to undergo a similar downturn. Band 8a on the other hand does not exhibit such a downslope. This continuation of from bands 7a and 7b is indeed suggestive that bands 8a and 8b are a continuation of the $X(Y)A_p$ configurations, however configurations based on these high-Ω orbitals are expect to be strongly coupled and no interlinking $M1$ transitions are observed for Bands 8a and 8b.

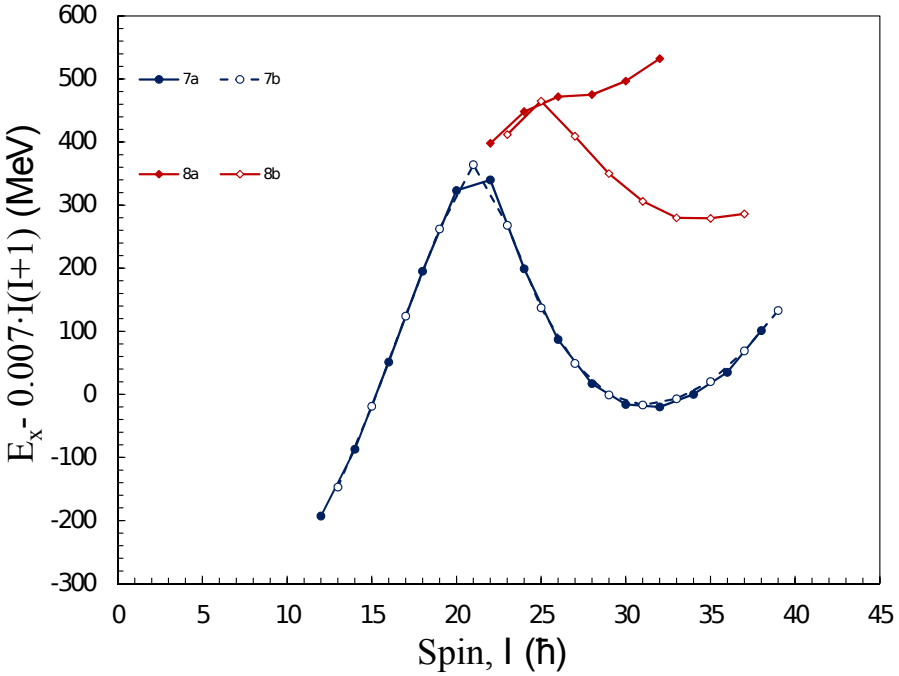

Figure 4.41: Excitation energies relative to a rigid rotor reference frame as a function of spin for bands 7a(7b) and bands 8a(8b).

Above $\hbar\omega \approx 0.35$ MeV, bands 8a and 8b have alignment of $i_x \approx 13\hbar$ and $i_x \approx 15\hbar$ respectively, implying that these bands must at the least include the high i_x AB neutrons. The only gain in alignment seen for bands 8a and 8b occur at the lowest-spin portion of these bands, which show the end of a band crossing for which the frequency is lower than that of the BC crossing seen in bands 1a and 1b. Furthermore the AB crossing is already seen to take place earlier at $\hbar\omega \approx 0.27$ MeV in bands 7a and 7b. It is therefore difficult to make judgements about the nature of this gain here.

A crossing with similar behaviour has been seen to take place in ^{157}Ho [17], and has been presented alongside bands 7a(7b) and 8a(8b) in Fig. 4.40. In this figure, bands 2a and 2b from ^{157}Ho involve an AB neutron crossing, as with the case of bands 7a and 7b, while bands 3a and 3b of ^{157}Ho both appear to involve a preceding alignment gain like that of band 8b. Radford *et al.* suggests that this gain seen for bands 3a and 3b in ^{157}Ho is a crossing which involves a combination of the second and third neutron crossings, producing a four-quasiparticle ABCD

neutron crossing. However, as bands 8a and 8b do not possess the same alignment it is not felt that the same crossing is responsible, and since band 8b is the only band to proceed to higher alignment than that of the four-quasiparticle X(Y)ABA$_p$ configurations of bands 7a and 7b following the backbend, the ABCD crossing argument would only be a possible solution for band 8b. Ultimately it is not felt that such a crossing is responsible for the systematics observed for this band and greater statistics are required to discern the true nature of what is taking place.

Table 4.2: Quasiparticle assignments for bands in ^{156}Ho from this work.

Band	Quasiparticle Configurations		
1	AA$_p$(B$_p$)	$\rightarrow$	ABCA$_p$(B$_p$)
2	EABA$_p$ (B$_p$)	$\rightarrow$	EABA$_p$B$_p$C$_p$(B$_p$A$_p$D$_p$)
3	BA$_p$(B$_p$)	$\rightarrow$	BADA$_p$(B$_p$) or BADA$_p$B$_p$C$_p$(B$_p$A$_p$D$_p$)
4 1st	FA$_p$(B$_p$)	$\rightarrow$	FABA$_p$(B$_p$)
4 2nd	AE$_p$(F$_p$)	$\rightarrow$	FABA$_p$(B$_p$)
5	EABE$_p$(F$_p$)	$\rightarrow$	EABE$_p$A$_p$B$_p$(F$_p$A$_p$B$_p$)
7	X(Y)A$_p$	$\rightarrow$	X(Y)ABA$_p$
9		Termination	

4.2.11.2 Band termination

Starting at spin $I^{\pi} = 28^{+}$ shape coexistence begins in the form of two of the newly identified bands, 9a and 9b, where the nucleus changes from the collective behaviour of bands 2a and 2b to the single-particle behaviour associated with particles in orbit about an axis of symmetry.

As discussed in section 3.1.10 of chapter 3, band termination takes place when a nucleus undergoes a shape change from that of a rotating prolate to a weakly oblate deformation, with the valence nucleons aligning with rotations of the nuclear core. Once all of the valence particles have fully aligned the band will terminate at a so-called *favoured state*. The process of this series of alignments may be observed by plotting the excitation energies for the bands relative to a rigid rotor (E - $E\_rigidrotor$) as a function of spin. A dramatic downturn in the slope of E - $E\_rigidrotor$ indicates the onset of band termination.
Such behaviour has been identified in new structures 9a and 9b, which feed to previously identified bands bands 2a and 2b respectively. Similar behaviour has also been identified in band 6. Excitation energies relative to a rigid rotor reference frame as a function of spin for sequences of γ-ray transitions corresponding to bands 2a and 2b alongside those of bands 9a and 9b have been plotted against similar structures from neighbouring nuclei in Fig. 4.42. It can be seen that above $I \approx 32^{+}$ the structures that feed to bands 2a and 2b see a down sloping trend culminating in termination at favoured states seen at 41^{+} and 42^{+}.
Total Routhian Surface (TRS) calculations performed using the EABAp configuration assigned to band 2a (Fig. 4.43) predict a shape change from collective to oblate to take place in a frequency range around $\hbar\omega \approx 0.45$ MeV, which coincides with the rotational frequencies of the second and third B_pC_p and A_pD_p proton crossings. Similar terminating states have been identified in the previously mentioned $ABCA_p(B_p)$ configurations of ^{155}Ho and ^{157}Ho following the B_pC_p and A_pD_p crossings. The terminating state of ^{155}Ho was observed at spin $79/2^{-}$ and has been described as a fully aligned

$$\pi[(h_{11/2})^3_{27/2}]_{27/2^-} \otimes \nu[(i_{13/2})^2_{12}(f_{7/2})^2_6(h_{9/2})^2_8]_{26^+}$$

configuration.

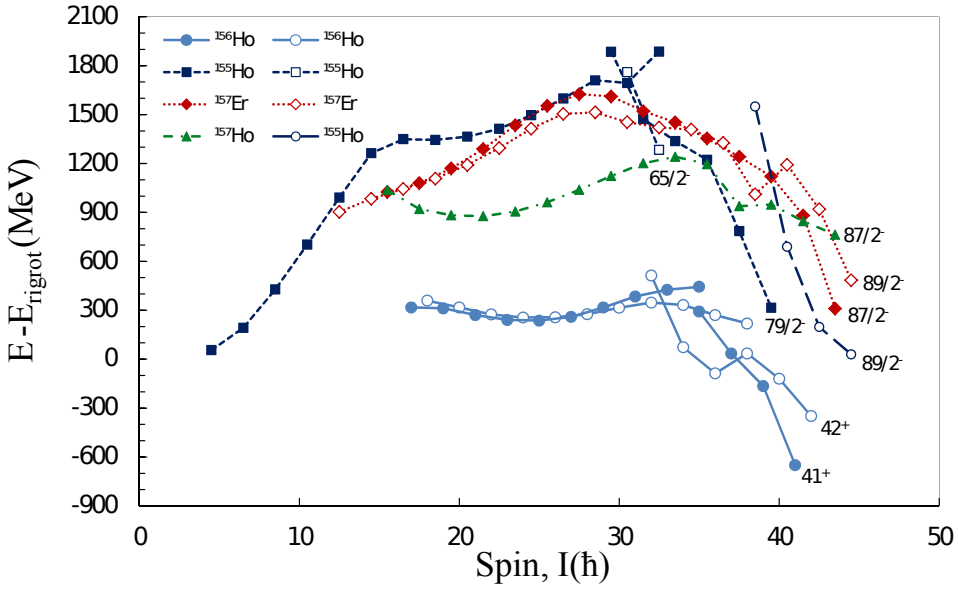

Figure 4.42: Observed excitation energy relative to a rigid rotor as a function of spin for terminating bands observed in ^{156}Ho, ^{155}Ho [9], ^{157}Ho [17] and ^{157}Er [18].

Building on this, the 41^+ and 42^+ favoured states seen in ^{156}Ho can be achieved through the addition of an $f_{7/2}$ or $h_{9/2}$ neutron respectively (See table 4.3), giving

$$\pi[(h_{11/2})^3_{27/2}]_{27/2^-} \otimes \nu[(i_{13/2})^2_{12}(f_{7/2})^3_{17/2}(h_{9/2})^2_8]_{55/2^+}$$

$$\pi[(h_{11/2})^3_{27/2}]_{27/2^-} \otimes \nu[(i_{13/2})^2_{12}(f_{7/2})^2_6(h_{9/2})^3_{21/2}]_{57/2^+}$$

These N = 89 configurations are consistent with terminating states observed at $87/2^-$ and $89/2^-$ in ^{157}Er [18] (Fig. 4.42).
There is an energetically favoured state at $I = 36^+$ preceding the terminating state at 42^+. Such states occur when one or more quasiparticle is yet to align, and analogous states have been observed in ^{155}Ho [9] and ^{157}Ho [17]. The $I = 36^+$ favoured state can be formed through shifting one anti-aligned $f_{7/2}/h_{9/2}$ neutron from an $m_i = 5/2$ to an $m_i = -7/2$ orbital, producing the

$$\pi[(h_{11/2})^3_{27/2}]_{27/2^-} \otimes \nu[(i_{13/2})^2_{12}(f_{7/2})^3_{5/2}(h_{9/2})^2_8]_{45/2^-}$$

configuration. A summary of the configurations assigned for bands 2a and 2b and the terminating configurations from neighbouring nuclei shown in Fig. 4.42 has

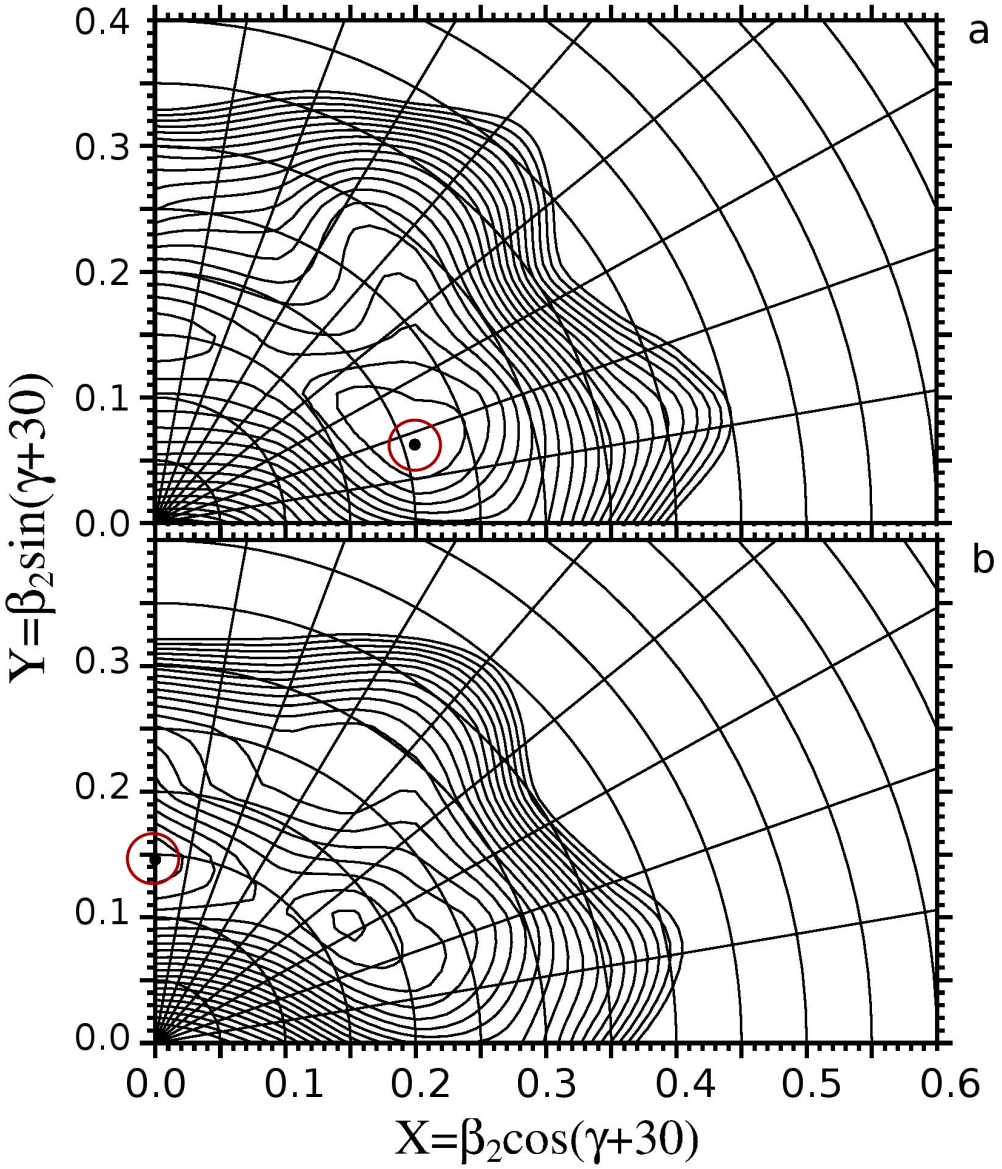

Figure 4.43: Total Routhian Surface calculations for quasiparticle configuration EABAp. Plots a and b correspond to rotational frequencies 0.432 MeV and 0.480 MeV respectively. The red circles highlight the Routhian minimums.

been presented in table 4.3. Similar behaviour to that seen for bands 2a and 2b prior to termination have also been observed in relation to band 3b. In Fig. 4.44 the characteristic downslope that precedes termination is readily apparent for

Table 4.3: Terminating configurations in ^{156}Ho and neighbouring nuclei.

Nucleus	I^π	Configuration
^{156}Ho	41^+	$\pi[(h_{11/2})^3_{27/2}]_{27/2^-} \otimes \nu[(i_{13/2})^2_{12}(f_{7/2})^3_{17/2}(h_{9/2})^2_8]_{55/2^-}$
^{156}Ho	42^+	$\pi[(h_{11/2})^3_{27/2}]_{27/2^-} \otimes \nu[(i_{13/2})^2_{12}(f_{7/2})^2_6(h_{9/2})^3_{21/2}]_{57/2^-}$
^{155}Ho	$65/2^-$	$\pi[(h_{11/2})^3_{27/2}]_{27/2^-} \otimes \nu[(i_{13/2})^2_{12}(f_{7/2})^3_{15/2}(h_{9/2})^1_{9/2}]_{19^+}$
^{155}Ho	$79/2^-$	$\pi[(h_{11/2})^3_{27/2}]_{27/2^-} \otimes \nu[(i_{13/2})^2_{12}(f_{7/2})^2_6(h_{9/2})^2_8]_{26^+}$
^{155}Ho	$89/2^-$	$\pi[(d_{5/2}/g_{7/2})^{-1}_{5/2}(h_{11/2})^4_{16}]_{35/2^+} \otimes \nu[(i_{13/2})^2_{12}(f_{7/2})^2_6(h_{9/2})^2_8]_{26^+}$
^{155}Ho	$89/2^-$	$\pi[(h_{11/2})^3_{27/2}]_{27/2^-} \otimes \nu[(i_{13/2})^2_{12}(f_{7/2})^2_6(h_{9/2})^2_8]_{26^+}$
^{157}Ho	$87/2^-$	$\pi[(h_{11/2})^3_{27/2}]_{27/2^-} \otimes \nu[(i_{13/2})^2_{12}(f_{7/2})^3_{17/2}(h_{9/2})^3_{21/2}]_{31^+}$
^{157}Er	$87/2^-$	$\pi[(h_{11/2})^4_{16}]_{16^+} \otimes \nu[(i_{13/2})^2_{12}(f_{7/2})^3_{17/2}(h_{9/2})^2_8]_{55/2^-}$
^{157}Er	$89/2^-$	$\pi[(h_{11/2})^4_{16}]_{16^+} \otimes \nu[(i_{13/2})^2_{12}(f_{7/2})^2_6(h_{9/2})^3_{21/2}]_{57/2^+}$

transitions from band 3b through band 6 and continues all the way to the 42^- state, the highest energy state observed for band 6 in this work. Furthermore, there is an energetically favoured state at $I^\pi = 32^-$ which is consistent with the existence of anti-aligned neutrons analogous to the state at $I^\pi = 36^+$ mentioned above.

It is likely that the terminating configuration for this band structure is the

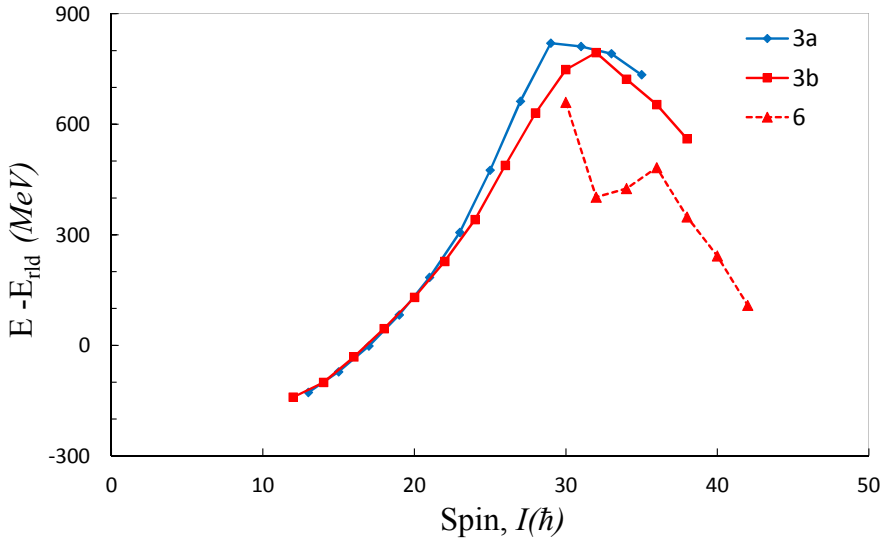

Figure 4.44: Excitation energy relative to a rigid rotor as a function of spin for bands 3a, 3b and 6.

$$\pi[(h_{11/2})^3_{27/2}]_{27/2^-} \otimes \nu[(i_{13/2})^3_{33/2}(f_{7/2})^2_6(h_{9/2})^2_8]_{61/2^+}$$

configuration, in which case band 6 would be expected to terminate at the 44^- state. Unfortunately the statistics were too low to discern any transitions above the 42^- state.

It is of note that band termination has been seen to take place immediately following the proton B_pC_p and A_pD_p crossings in bands primarily involving the proton A_p and B_p signature partners in both ^{155}Ho and ^{157}Ho, a trend that is continued in bands 2a and 2b of ^{156}Ho and perhaps bands 3a and 3b as well.

Chapter 5

Conclusion

In a testament to the advances in detection capabilities and analytical techniques, it has been possible to corroborate, revise and significantly expand upon previous work for ^{156}Ho following a high-spin experiment performed at the ATLAS facility of Argonne National Laboratory to study the spin structures of $^{155-157}$Ho.
Many newly identified transitions have been contributed to the decay scheme for this nucleus and each previously established band structure has been extended. Excepting bands 7a and 7b (and by extension bands 8a and 8b), which are proposed to be built on the X(Y) neutron signature partners, the band head energies, spins and parities relative to the low spin yrast bands are now known for all band structures.
Bands 3a and 3b, which were were formerly proposed to be built on the $E_p(F_p)$ proton signature partners coupled to the $\alpha = 1/2$ A neutron, have been reassigned as a coupling of the $A_p(B_p)$ proton signatures to the α = -1/2 B neutron in light of the decay pattern feeding from these bands to the yrast. Cranked shell model calculations were performed to determine the γ deformation for relevant quasi-particle configurations across a range of rotational frequencies. From these it was found that a number of favoured configurations are expected to exhibit a negative γ triaxial deformation even at low spins. Factoring this into the computed *B(M1)/B(E2)* ratios of reduced transition probabilities for the proposed configurations found good agreement with the new interpretation. Signature staggering observed in the *B(M1)/B(E2)* ratios support the treatement of this nucleus as possessing triaxial deformation.

Another two bands previously identified as distinct have been found to belong to the same structure, and the level scheme has been adjusted to reflect this. With this merge an anomalous gain in alignment was revealed for the new band structure which defied an easy explanation. Following a cross examination of nearby odd-odd nuclei where several similar structures were found to exist, two possible low spin quasiparticle configurations have been proposed. The first is that bands 4a and 4b are built on $A_P(B_p)$ proton signatures coupled to the α = -1/2, F neutron, with the backbend observed at $\hbar\omega \approx 0.32$ MeV explained as being the first AB neutron crossing, producing an $FABA_pB_p$ configuration. However the alignment gain is notably smaller than expected for the AB neutron crossing.
Alternatively, it is suggested that the low-spin configuration for these bands involves the $AE_p(F_p)$ configuration, which is then crossed by a more favoured $FABA_p(B_p)$ configuration. This interpretation is given credence by the existence of similar such crossing configurations in the mass = 130 region. Furthermore the analogous bands in nearby odd-odd nuclei exhibit very different signature splitting profiles to that of bands 4a and 4b.
A new signature partner band for band 5a has been identified and labelled 5b. These bands have been assigned the $EABE_p(F_p)$ configuration.
At $I^\pi = 28^+$ and $I^\pi = 35^+$ two new structures feeding into bands 2a and 2b have been identified and labelled bands 9a and 9b. Within these structures energetically favoured states typical of bands undergoing termination have been identified at $I^\pi = 41^+$ and 42^+. Relative to the ^{146}Gd core the valence particle configurations for these terminating states have been found to correspond to

$$\pi[(h_{11/2})^3_{27/2}]_{27/2^-} \otimes \nu[(i_{13/2})^2_{12}(f_{7/2})^3_{17/2}(h_{9/2})^2_8]_{55/2^+}$$

for the $I^\pi = 41^+$ state, and

$$\pi[(h_{11/2})^3_{27/2}]_{27/2^-} \otimes \nu[(i_{13/2})^2_{12}(f_{7/2})^2_6(h_{9/2})^3_{21/2}]_{57/2^+}$$

for the $I^\pi = 42^+$ state.
These terminating states are consistent with a shift to oblate deformation predicted in total routhian surface calculations. Another newly identified band labelled band 6 has been found to also exhibit behaviour typical of a band approaching termination and is predicted to terminate at the 44^- state with the following configuration:

$$\pi[(h_{11/2})^3_{27/2}]_{27/2^-} \otimes \nu[(i_{13/2})^3_{33/2}(f_{7/2})^2_6(h_{9/2})^2_8]_{61/2^+}$$

however the statistics were insufficient to observe any states above $I^\pi = 42^-$ and as of yet it is not known whether this band truly is approaching termination.

Appendix

Table 1: Energies, Intensities, angular-intensity ratios, and spin-parity assignments for the observed ^{156}Ho transitions. The band labels used in the final column correspond to those in the decay scheme. All spin/parity assignments are relative to an unknown groundstate and are therefore tentative.

E_γ (keV)	I	R	Multipolarity	Assignment	Band
47.1	10.8 ± 0.6	0.9 ± 0.01	M1/E2	$8^- \rightarrow 7^-$	1
54.1	12.5 ± 0.3	0.8 ± 0.01	M1/E2	$9^- \rightarrow 8^-$	1
80.6	5.3 ± 0.6			$9^+ \rightarrow 10^-$	4
90.5	19.6 ± 0.7			$9^- \rightarrow 8^-$	1
94.4	26 ± 1.2	0.77 ± 0.02	M1/E2	$10^- \rightarrow 9^-$	1
96.2	9.3 ± 0.9	0.79 ± 0.03	M1/E2	$10^- \rightarrow 9^-$	1
102.8	0.6 ± 1			$9^- \rightarrow 7^-$	1
129.5	48.4 ± 1.5	0.81 ± 0.01	M1/E2	$13^- \rightarrow 12^-$	1
131.7	1.6 ± 0.3			$36^+ \rightarrow 35^+$	9
133.3	20.1 ± 0.7			$11^- \rightarrow 10^-$	1
134.6	54.4 ± 1.8	0.78 ± 0.002	M1/E2	$11^- \rightarrow 10^-$	1
161.5	3.6 ± 0.2			$11^+ \rightarrow 10^+$	4
162.7	2.8 ± 0.2			$10^+ \rightarrow 9^+$	4
187.8	1.32 ± 0.04	0.76 ± 0.06	M1/E2	$12^- \rightarrow 11^-$	3
195	4.1 ± 0.1	0.75 ± 0.09	M1/E2	$13^- \rightarrow 12^-$	3
210.3	100 ± 2.4			$12^- \rightarrow 11^-$	1
212.4	27.3 ± 0.8			$15^- \rightarrow 14^-$	1
216.7	3 ± 0.1			$13^+ \rightarrow 12^+$	4
218.4	2.5 ± 0.1			$12^+ \rightarrow 11^+$	4
222.4	1.5 ± 0.2	0.90 ± 0.05	M1/E2	$19^+ \rightarrow 18^+$	3
223.3	2.8 ± 0.1			$14^- \rightarrow 13^-$	3
227.9	5.8 ± 0.5	0.63 ± 0.01	M1/E2	$13^+ \rightarrow 12^+$	7
228.8	5.9 ± 0.2			$11^- \rightarrow 9^-$	1
237.8	4.6 ± 0.2	0.77 ± 0.04	M1/E2	$15^- \rightarrow 14^-$	3
250	1.6 ± 0.1	1.01 ± 0.02	M1/E2	$23^+ \rightarrow 22^+$	7
251.7	10.2 ± 0.3			$21^+ \rightarrow 20^+$	2
255.9	4.2 ± 0.2	0.61 ± 0.01	M1/E2	$14^+ \rightarrow 13^+$	7
262.4	1.5 ± 0.01			$15^+ \rightarrow 14^+$	4
263.2	5.4 ± 0.2	0.85 ± 0.01	M1/E2	$16^- \rightarrow 15^-$	3
264.1	46 ± 1.4	0.84 ± 0.38	M1/E2	$14^- \rightarrow 13^-$	1
265.8	2.6 ± 0.2			$14^+ \rightarrow 13^+$	4
266.7	4.7 ± 0.2			$24^+ \rightarrow 23^+$	7
267	1.9 ± 0.1	1.05 ± 0.05	M1/E2	$17^- \rightarrow 16^-$	3
274.1	3.3 ± 0.6			$11^+ \rightarrow 11^-$	$4 \rightarrow 1$
277.8	2.9 ± 0.2			$15^+ \rightarrow 14^+$	7
283.4	14.9 ± 0.5	0.82 ± 0.01	M1/E2	$17^- \rightarrow 16^-$	1
284	1.7 ± 0.1	0.74 ± 0.02	M1/E2	$22^+ \rightarrow 21^+$	7
287.7	1.1 ± 0.1	0.98 ± 0.05	M1/E2	$25^+ \rightarrow 24^+$	7

Table 1 continued.

E_γ (keV)	I	R	Multipolarity	Assignment	Band
289.2	6.5 ± 0.2	0.66 ± 0.02	M1/E2	$20^+ \rightarrow 19^+$	2
291.5	1.4 ± 0.1	0.67 ± 0.03	M1/E2	$22^+ \rightarrow 21^+$	4
292.9	10.7 ± 0.4	0.67 ± 0.01	M1/E2	$23^+ \rightarrow 22^+$	2
295	0.9 ± 0.1	0.62 ± 0.02	M1/E2	$16^+ \rightarrow 15^+$	7
298.1	5.6 ± 0.2	0.82 ± 0.02	M1/E2	$18^- \rightarrow 17^-$	3
299.3	30.4 ± 0.9	0.92 ± 0.22	M1/E2	$16^- \rightarrow 15^-$	1
300.5	0.7 ± 0.1			$17^+ \rightarrow 16^+$	4
302.4	5.1 ± 0.2	0.86 ± 0.09	M1/E2	$19^- \rightarrow 18^-$	3
305.9	3.7 ± 0.2			$16^+ \rightarrow 15^+$	4
310.8	1.9 ± 0.2			$17^+ \rightarrow 16^+$	7
314.4	1 ± 0.1			$26^+ \rightarrow 25^+$	7
315.8	10.8 ± 0.4	0.70 ± 0.01	M1/E2	$22^+ \rightarrow 21^+$	2
317	3.1 ± 0.2	0.76 ± 0.01	M1/E2	$24^+ \rightarrow 23^+$	4
323.2	1.4 ± 0.1	0.79 ± 0.03	M1/E2	$18^+ \rightarrow 17^+$	7
324	0.5 ± 0.1	1.09 ± 0.09	E2	$11^+ \rightarrow 9^+$	4
326.5	16.8 ± 0.5	0.78 ± 0.01	M1/E2	$18^- \rightarrow 17^-$	1
328.5	6 ± 0.2	0.82 ± 0.03	M1/E2	$20^- \rightarrow 19^-$	3
329.5	1.9 ± 0.1			$19^+ \rightarrow 18^+$	4
333.4	1.3 ± 0.2			$19^+ \rightarrow 18^+$	4
333.8	2.6 ± 0.2			$21^+ \rightarrow 20^+$	7
335.2	2.2 ± 0.2	0.96 ± 0.01	M1/E2	$21^+ \rightarrow 20^+$	7
335.2	2.1 ± 0.2	0.81 ± 0.02	M1/E2	$18^+ \rightarrow 17^+$	2
336.1	8 ± 0.3			$25^+ \rightarrow 24^+$	4
336.4	0.1 ± 0.04	0.81 ± 0.03	M1/E2	$24^- \rightarrow 23^-$	5
339.6	50.6 ± 1.6	1.15 ± 0.06	E2	$13^- \rightarrow 11^-$	1
339.9	1.9 ± 0.2	1.10 ± 0.10	M1/E2	$27^+ \rightarrow 26^+$	7
340.8	1.8 ± 0.2	0.96 ± 0.01	M1/E2	$23^- \rightarrow 22^-$	5
341.2	1.7 ± 0.1			$20^+ \rightarrow 19^+$	7
343.1	1.3 ± 0.1			$20^+ \rightarrow 19^+$	4
344.2	8 ± 0.3	0.78 ± 0.01	M1/E2	$19^- \rightarrow 18^-$	1
345.9	3.5 ± 0.2			$26^+ \rightarrow 25^+$	4
346.5	1.7 ± 0.2	0.84 ± 0.05	M1/E2	$21^- \rightarrow 20^-$	3
348	0.4 ± 0.2			$39^+ \rightarrow 38^+$	9
348.2	10.4 ± 0.4	0.82 ± 0.06	M1/E2	$20^- \rightarrow 19^-$	1
351.4	4.2 ± 0.1			$22^- \rightarrow 21^-$	3
356	8.1 ± 0.3	0.76 ± 0.02	M1/E2	$24^+ \rightarrow 23^+$	2
358.8	1.9 ± 0.1			$28^- \rightarrow 27^-$	5
359.6	2.3 ± 0.2			$25^- \rightarrow 24^-$	3

Table 1 continued.

E_γ (keV)	I	R	Multipolarity	Assignment	Band
360.7	1.5 ± 0.1			$24^- \rightarrow 23^-$	5
360.8	0.4 ± 0.1			$28^+ \rightarrow 27^+$	7
361.9	4.7 ± 0.2	0.79 ± 0.01	M1/E2	$22^- \rightarrow 21^-$	1
363.7	2.7 ± 0.2			$23^+ \rightarrow 22^+$	4
366.7	2.6 ± 0.2			$24^- \rightarrow 23^-$	1
369.3	1.6 ± 0.1			$26^- \rightarrow 25^-$	5
370.5	0.3 ± 0.2	0.85 ± 0.12		$30^+ \rightarrow 30^+$	$9 \rightarrow 2$
371.3	4 ± 0.1	0.70 ± 0.07	M1/E2	$24^- \rightarrow 23^-$	3
373.9	2.8 ± 0.2			$26^- \rightarrow 25^-$	1
376.8	3.1 ± 0.4			$26^- \rightarrow 25^-$	3
377.1	7.8 ± 0.3	1.05 ± 0.01	E2	$12^+ \rightarrow 10^+$	4
381.4	4.4 ± 0.4	1.38 ± 0.06	E2	$13^- \rightarrow 11^-$	3
383.4	5.8 ± 1.5			$27^- \rightarrow 26^-$	5
385.4	1.6 ± 0.1			$28^- \rightarrow 27^-$	5
385.8	0.3 ± 0.1	0.78 ± 0.07	M1/E2	$27^+ \rightarrow 26^+$	2
389.2	3.9 ± 0.2	0.73 ± 0.02	M1/E2	$26^+ \rightarrow 25^+$	2
391.4	8 ± 0.3	0.78 ± 0.17	M1/E2	$28^+ \rightarrow 27^+$	4
392.3	2.6 ± 0.2			$28^- \rightarrow 27^-$	1
393.9	2.9 ± 0.2	1.19 ± 0.01	E2	$14^- \rightarrow 12^-$	1
394	16.2 ± 0.4			$23 \rightarrow 22^+$	$8 \rightarrow 7$
395.9	5.7 ± 0.3			$21^- \rightarrow 20^-$	1
397.4	1 ± 0.1			$30^- \rightarrow 29^-$	5
400.4	1.9 ± 0.1	0.82 ± 0.01	M1/E2	$23^- \rightarrow 22^-$	3
405.6	0.7 ± 0.01			$29^- \rightarrow 28^-$	5
413.8	5 ± 0.2			$28^+ \rightarrow 27^+$	2
415.3	0.3 ± 0.1			$32^- \rightarrow 31^-$	5
417	1.6 ± 0.2			$32^+ \rightarrow 31^+$	2
417.9	2.1 ± 0.2			$25^+ \rightarrow 24^+$	4
418.2	5.6 ± 0.2	1.02 ± 0.03	E2	$14^- \rightarrow 12^-$	3
418.8	0.5 ± 0.2			$39^- \rightarrow 38^-$	5
422.6	4.2 ± 0.2			$30^- \rightarrow 29^-$	1
424.5	2.7 ± 0.3			$30^+ \rightarrow 29^+$	2
433.1	1.3 ± 0.1			$23^- \rightarrow 22^-$	1
433.6	0.9 ± 0.2			$31^- \rightarrow 30^-$	5
434.3	3.1 ± 0.2	1.35 ± 0.08	E2	$13^+ \rightarrow 11^+$	4
441.6	3.5 ± 0.2			$34^- \rightarrow 33^-$	5
445.1	2.9 ± 0.4			$48^+ \rightarrow 46^+$	9
448.5	3 ± 0.2			$25^- \rightarrow 24^-$	1

Table 1 continued.

E_γ (keV)	I	R	Multipolarity	Assignment	Band
452.8	3.9 ± 0.2			$29^+ \rightarrow 28^+$	2
454.1	4.2 ± 0.2			$32^- \rightarrow 31^-$	1
461.5	8.7 ± 0.2	1.1 ± 0.02	E2	$15^- \rightarrow 13^-$	3
462.1	2.1 ± 0.2			$27^+ \rightarrow 26^+$	4
463.9	2.4 ± 0.2			$27^- \rightarrow 26^-$	1
464.6	3.3 ± 0.2			$33^- \rightarrow 32^-$	5
474.7	4.9 ± 1.6			$11^- \rightarrow 10^-$	$3 \rightarrow 1$
474.8	1.2 ± 0.2			$36^- \rightarrow 35^-$	5
476.4	55.3 ± 1.7	1.12 ± 0.05	E2	$15^- \rightarrow 13^-$	1
481.1	3.5 ± 0.2	1.20 ± 0.02	M1/E2	$29^- \rightarrow 28^-$	4
482.3	5.5 ± 0.3			$14^+ \rightarrow 12^+$	1
483.5	4.15 ± 0.23	1.19 ± 0.01	E2	$14^+ \rightarrow 12^+$	7
488.7	1.11 ± 0.18	0.96 ± 0.04	E1	$12^+ \rightarrow 11^-$	4
494.9	0.34 ± 0.21			$35^- \rightarrow 34^-$	5
495.6	2.1 ± 0.3			$38^- \rightarrow 37^-$	5
498.5	0.85 ± 0.22			$13^+ \rightarrow 12^-$	$4 \rightarrow 1$
500.8	8.7 ± 0.4			$16^- \rightarrow 14^-$	3
510.3	10 ± 0.5	1.12 ± 0.01	E2	$34^+ \rightarrow 32^+$	9
511.8	7.6 ± 0.3	1.24 ± 0.01	E2	$20^+ \rightarrow 18^+$	2
511.8	28.5 ± 1	1.21 ± 0.004	E2	$16^- \rightarrow 14^-$	1
512.6	1.7 ± 0.4			$37^- \rightarrow 36^-$	5
513.6	4.3 ± 0.4			$13^- \rightarrow 12^-$	$3 \rightarrow 1$
514.3	2.4 ± 0.24			$31^- \rightarrow 30^-$	1
517.1	5.15 ± 0.22			$24^+ \rightarrow 22^+$	7
520	3.26 ± 0.19			$19^+ \rightarrow 17^+$	2
527.3	2.93 ± 0.19	1.34 ± 0.08	E2	$15^+ \rightarrow 13^+$	4
527.4	5.17 ± 0.17			$12^- \rightarrow 11^-$	$3 \rightarrow 1$
531.6	12.1 ± 0.22	1.24 ± 0.03	E2	$17^- \rightarrow 15^-$	3
533.8	3.76 ± 0.23			$15^+ \rightarrow 13^+$	7
533.9	5.56 ± 0.2			$23^+ \rightarrow 21^+$	7
536.2	1.14 ± 0.17			$32^- \rightarrow 30^-$	$6 \rightarrow 3$
541.3	9.6 ± 0.4	1.34 ± 0.04	E2	$21^+ \rightarrow 19^+$	2
555	4.86 ± 0.23			$25^+ \rightarrow 23^+$	7
560.4	9.9 ± 0.4			$23^+ \rightarrow 22^-$	$2 \rightarrow 1$
567.2	10.1 ± 0.5	1.24 ± 0.02	E2	$18^- \rightarrow 16^-$	3
567.7	11.9 ± 0.4	1.29 ± 0.02	E2	$22^+ \rightarrow 20^+$	2
569	8.7 ± 0.3	1.14 ± 0.02	E2	$16^+ \rightarrow 14^+$	4
572.6	8.3 ± 0.4	1.25 ± 0.01	E2	$16^+ \rightarrow 14^+$	7

Table 1 continued.

E_γ (keV)	I	R	Multipolarity	Assignment	Band
580.3	3.46 ± 0.2			$15^- \rightarrow 14^-$	$3 \rightarrow 1$
583	43.6 ± 1.4	1.34 ± 0.08	E2	$17^- \rightarrow 15^-$	1
583	5 ± 17.8			$36^+ \rightarrow 34^+$	$9 \rightarrow 2$
588.5	1.3 ± 0.4			$32^+ \rightarrow 31^+$	$9 \rightarrow 2$
598.8	3.3 ± 0.3			$17^- \rightarrow 16^-$	$3 \rightarrow 1$
601.9	6 ± 0.3			$26^+ \rightarrow 24^+$	7
602.2	14.9 ± 0.7	1.22 ± 0.03	E2	$19^- \rightarrow 17^-$	3
605.2	6.4 ± 0.4			$17^+ \rightarrow 15^+$	7
605.7	6.4 ± 0.3	1.19 ± 0.03	E2	$17^+ \rightarrow 15^+$	4
607.5	4 ± 0.3	0.84 ± 0.06	M1/E2	$14^- \rightarrow 13^-$	$3 \rightarrow 1$
608.1	16.3 ± 0.6	1.25 ± 0.01	E2	$23^+ \rightarrow 21^+$	2
610.3	34.8 ± 1.1	1.19 ± 0.01	E2	$18^- \rightarrow 16^-$	1
619.3	6.7 ± 0.3			$22^+ \rightarrow 20^+$	7
622.5	7.8 ± 0.4			$22^+ \rightarrow 20^+$	4
625.3	4.3 ± 0.4	1.46 ± 0.10	E2	$32^- \rightarrow 30^-$	$6 \rightarrow 5$
629.2	5.4 ± 0.7	1.00 ± 0.07	E2	$32^- \rightarrow 30^-$	$6 \rightarrow 5$
630.2	3 ± 0.3	1.07 ± 0.01	E1	$15^+ \rightarrow 14^-$	$2 \rightarrow 1$
630.8	3.3 ± 0.3			$22^+ \rightarrow 21^-$	$4 \rightarrow 1$
631.5	10.6 ± 0.5	1.41 ± 0.10	E2	$20^- \rightarrow 18^-$	3
631.7	1.54 ± 0.24	1.02 ± 0.03	E1	$14^+ \rightarrow 13^-$	$4 \rightarrow 1$
633.5	7.4 ± 0.4			$18^+ \rightarrow 16^+$	7
636	2.15 ± 0.25			$16^- \rightarrow 15^-$	$3 \rightarrow 1$
637.9	9.5 ± 0.6	1.21 ± 0.02	E2	$18^+ \rightarrow 16^+$	4
643.5	5.5 ± 0.4	0.47 ± 0.02	M1/E2	$37^+ \rightarrow 36^+$	9
649.1	12.2 ± 0.4	1.15 ± 0.02	E2	$24^+ \rightarrow 22^+$	2
653.6	3.4 ± 0.22	1.32 ± 0.03	E2	$27^+ \rightarrow 25^+$	7
654.8	3.11 ± 0.25	1.45 ± 0.09	E2	$23^+ \rightarrow 21^+$	4
656.2	5.4 ± 0.3	1.30 ± 0.03	E2	$19^+ \rightarrow 17^+$	7
660	4.7 ± 0.3			$22^+ \rightarrow 21^-$	$4 \rightarrow 1$
662.2	1.22 ± 0.22			$23^+ \rightarrow 22^-$	$4 \rightarrow 1$
665.6	3.9 ± 0.4			$41^+ \rightarrow 39^+$	9
665.8	2.8 ± 0.3	1.35 ± 0.05	E2	$19^+ \rightarrow 17^+$	4
671	28.5 ± 0.9	1.30 ± 0.09	E2	$19^- \rightarrow 17^-$	5
671.4	3 ± 0.4			$23^- \rightarrow 21^-$	4
672.8	7.9 ± 0.4			$20^+ \rightarrow 18^+$	1
674	7.5 ± 0.5	1.55 ± 0.02	E2	$20^+ \rightarrow 18^+$	7
674.9	11.6 ± 0.4	1.26 ± 0.02	E2	$21^- \rightarrow 19^-$	3
676	3.8 ± 0.4	1.24 ± 0.01	E2	$21^+ \rightarrow 19^+$	7

Table 1 continued.

E_γ (keV)	I	R	Multipolarity	Assignment	Band
676.1	5 ± 0.4	1.30 ± 0.03	E2	$21^+ \rightarrow 19^+$	4
676.9	2.86 ± 0.12	1.31 ± 0.02	E2	$24^- \rightarrow 22^-$	5
677	1.6 ± 0.5			$22 \rightarrow 20^+$	$8 \rightarrow 7$
678	0.9 ± 0.3			$23 \rightarrow 21^+$	$9 \rightarrow 2$
678.2	4.09 ± 0.25			$34^+ \rightarrow 32^+$	$8 \rightarrow 7$
680.7	6.8 ± 0.3			$24^+ \rightarrow 22^+$	4
686	1.36 ± 0.2			$27 \rightarrow 25$	8
692	20.3 ± 0.7	1.32 ± 0.01	E2	$25^+ \rightarrow 23^+$	2
692.8	26.7 ± 0.6	1.3 ± 0.03	E2	$20^- \rightarrow 18^-$	1
696.2	5.5 ± 0.21			$25^- \rightarrow 23^-$	5
698.8	7 ± 0.25	1.17 ± 0.07	E2	$22^- \rightarrow 20^-$	3
699.5	2.9 ± 0.22	1.18 ± 0.03	E2	$28^+ \rightarrow 26^+$	7
703.5	0.9 ± 0.23			$24^- \rightarrow 23^+$	$5 \rightarrow 2$
708.3	2.25 ± 0.24			$24 \rightarrow 22$	8
709.3	6.8 ± 0.3	0.8 ± 0.04	E1	$21^+ \rightarrow 20^-$	$2 \rightarrow 1$
712.5	3 ± 9.2	1.16 ± 0.12	M1/E2	$35^+ \rightarrow 34^+$	9
720.4	1.83 ± 0.21			$25^- \rightarrow 23^-$	$5 \rightarrow 1$
722.4	5.1 ± 0.4			$32^+ \rightarrow 30^+$	$4 \rightarrow 1$
722.7	2.2 ± 0.3	1.05 ± 0.09	E1	$16^+ \rightarrow 15^-$	9
723	2.2 ± 0.3	0.83 ± 0.01	E1	$17^+ \rightarrow 16^-$	$4 \rightarrow 1$
725.4	13.6 ± 0.5	1.27 ± 0.02	E2	$26^+ \rightarrow 24^+$	2
729.1	6.7 ± 0.4	1.28 ± 0.03	E2	$26^- \rightarrow 24^-$	5
734.9	4 ± 0.3			$25^+ \rightarrow 23^+$	4
736.2	1.13 ± 0.13			$14^- \rightarrow 12^-$	$3 \rightarrow 1$
737.5	1.59 ± 0.23	1.37 ± 0.19	E2	$26 \rightarrow 24$	8
739	3.1 ± 0.3	1.24 ± 0.13	E2	$25 \rightarrow 23$	8
739	1 ± 0.4			$29 \rightarrow 27$	8
739	0.28 ± 0.23	1.31 ****	E2	$23^- \rightarrow 21^-$	$5 \rightarrow 1$
743.2	14.8 ± 0.5	1.03 ± 0.26	E2	$21^- \rightarrow 19^-$	1
747	4.34 ± 0.23			$29^+ \rightarrow 27^+$	7
752.3	9.4 ± 0.3	1.36 ± 0.06	E2	$23^- \rightarrow 21^-$	3
753.1	6.8 ± 0.3	1.24 ± 0.03	E2	$27^- \rightarrow 25^-$	5
757.4	16.9 ± 0.5	1.31 ± 0.03	E2	$22^- \rightarrow 20^-$	1
762.8	3.5 ± 0.4	1.08 ± 0.04	E2	$23^- \rightarrow 21^-$	$5 \rightarrow 1$
763.4	8.2 ± 0.4	1.64 ± 0.10	E2	$26^+ \rightarrow 24^+$	4
765.1	0.9 ± 0.3			$21^+ \rightarrow 20^-$	$4 \rightarrow 1$
768.8	7.1 ± 0.4	1.1 ± 0.05	E2	$28^- \rightarrow 26^-$	5
771.1	6.3 ± 0.3			$24^- \rightarrow 22^-$	3

Table 1 continued.

E_γ (keV)	I	R	Multipolarity	Assignment	Band
773.4	1.48 ± 0.18	1.51 ± 0.12	E2	$28 \rightarrow 26$	8
774	20.1 ± 0.7	1.41 ± 0.02	E2	$27^+ \rightarrow 25^+$	2
777	1 ± 0.4	0.94 ± 0.02	E1	$18^+ \rightarrow 17^-$	$4 \rightarrow 1$
779.6	4.5 ± 0.4			$37^+ \rightarrow 35^+$	9
780.5	1.5 ± 0.3			$19^+ \rightarrow 18^-$	$4 \rightarrow 1$
781.6	4 ± 0.4	0.92 ± 0.03	E1	$20^+ \rightarrow 19^-$	$4 \rightarrow 1$
790.8	6.6 ± 0.3	1.28 ± 0.03	E2	$29^- \rightarrow 27^-$	5
792.7	2.9 ± 2.3	1.26 ± 0.04	E2	$30^+ \rightarrow 28^+$	7
794.9	5.7 ± 0.3	1.35 ± 0.04	E2	$23^- \rightarrow 21^-$	1
799.3	14.5 ± 0.5	1.32 ± 0.03	E2	$28^+ \rightarrow 26^+$	2
801.2	5.2 ± 0.3	1.18 ± 0.02	E2	$24^- \rightarrow 22^-$	1
803.1	5.28 ± 0.22	1.30 ± 0.04	E2	$30^- \rightarrow 28^-$	5
806.1	8.1 ± 0.4	0.74 ± 0.03	E1	$20^+ \rightarrow 19^-$	$2 \rightarrow 1$
807.1	5 ± 0.3	1.14 ± 0.05	E2	$27^+ \rightarrow 25^+$	4
808.6	4.19 ± 0.23			$30^- \rightarrow 28^-$	$6 \rightarrow 5$
810	0.93 ± 0.15	1.64 ± 0.29	E2	$31 \rightarrow 29$	8
819	4.74 ± 0.24	1.62 ± 0.11	E2	$25^- \rightarrow 23^-$	1
825.1	5.5 ± 0.3	1.38 ± 0.09	E2	$26^- \rightarrow 24^-$	1
830.7	6.9 ± 0.4			$31^- \rightarrow 29^-$	5
831.8	3 ± 0.3			$38^+ \rightarrow 36^+$	$9 \rightarrow 2$
835.7	5.8 ± 0.4			$27^- \rightarrow 25^-$	1
838	4 ± 0.3			$31^+ \rightarrow 29^+$	7
843.1	2.8 ± 0.5			$32^- \rightarrow 30^-$	$5 \rightarrow 3$
845.1	0.2 ± 0.3			$16^- \rightarrow 14^-$	3
845.5	4 ± 0.4			$31^- \rightarrow 29^-$	$3 \rightarrow 1$
845.6	2.6 ± 0.4			$15^- \rightarrow 13^-$	$3 \rightarrow 1$
845.8	4.5 ± 0.3			$35^+ \rightarrow 33^+$	$9 \rightarrow 2$
847.6	8.6 ± 0.7			$30 \rightarrow 28$	8
848.1	1.25 ± 0.22	1.46 ± 0.05	E2	$36^+ \rightarrow 34^+$	9
849.2	4.8 ± 0.5			$32^- \rightarrow 30^-$	5
850.6	3 ± 0.3			$30^- \rightarrow 28^-$	$5 \rightarrow 3$
852	1.25 ± 0.22	1.32 ± 0.13	E2	$30^+ \rightarrow 28^+$	9
853.1	5.8 ± 0.4	1.24 ± 0.08	E2	$28^+ \rightarrow 26^+$	4
855.3	4.3 ± 0.24	1.54 ± 0.13	E2	$30^- \rightarrow 28^-$	3
855.7	8 ± 0.4			$25^- \rightarrow 23^-$	$5 \rightarrow 3$
856.8	5.1 ± 0.3	1.27 ± 0.04	E2	$28^- \rightarrow 26^-$	1
860.8	12.6 ± 0.6	1.42 ± 0.06	E1	$19^+ \rightarrow 18^-$	3

Table 1 continued.

E_γ (keV)	I	R	Multipolarity	Assignment	Band
861.5	6.2 ± 0.3	0.68 ± 0.01	E2	$26^- \rightarrow 24^-$	$2 \rightarrow 1$
866.4	4.2 ± 0.3			$34^- \rightarrow 32^-$	3
866.8	18.8 ± 0.7	1.27 ± 0.02	E2	$29^+ \rightarrow 27^+$	2
871.9	4.9 ± 0.3			$29^+ \rightarrow 27^+$	4
877.7	16 ± 0.6	1.18 ± 0.02	E2	$30^+ \rightarrow 28^+$	2
878.3	3.3 ± 0.3	1.29 ± 0.02	E2	$32^+ \rightarrow 30^+$	7
880	4.8 ± 0.3	1.21 ± 0.03	E2	$33^- \rightarrow 31^-$	1
880.3	3.5 ± 0.4	1.31 ± 0.03	E2	$29^- \rightarrow 27^-$	5
882.5	1.3 ± 0.5			$32^+ \rightarrow 33^+$	$9 \rightarrow 7$
884	0.47 ± 0.17			$33 \rightarrow 31$	8
890.5	4.6 ± 0.3			$33^- \rightarrow 31^-$	3
892.4	3.9 ± 0.5			$39^+ \rightarrow 37^+$	9
896	1.2 ± 0.4			$32^+ \rightarrow 30^+$	NC $\rightarrow$ 4
897.2	0.5 ± 0.3			$18^- \rightarrow 16^-$	$3 \rightarrow 1$
899.5	1.3 ± 0.3			$17^- \rightarrow 15^-$	$3 \rightarrow 1$
903.9	4.5 ± 0.4			$34^- \rightarrow 32^-$	5
904.5	3 ± 0.4			$23^- \rightarrow 22^-$	$5 \rightarrow 1$
906.7	1.9 ± 0.3	1.16 ± 0.05	E2	$35^- \rightarrow 33^-$	1
907.1	4.6 ± 0.4			$30^- \rightarrow 28^-$	3
911.1	7 ± 0.3	1.42 ± 0.16	E2	$28^- \rightarrow 26^-$	3
914	3.7 ± 0.3	1.31 ± 0.08	E2	$39^- \rightarrow 37^-$	5
915.7	2.7 ± 0.3			$38^- \rightarrow 36^-$	6
916	0.32 ± 0.16			$32 \rightarrow 30$	8
919.1	3.3 ± 0.4	1.22 ± 0.03	E2	$19^- \rightarrow 17^-$	7
920.2	3.72 ± 0.24			$33^+ \rightarrow 31^+$	$3 \rightarrow 1$
921.1	5.3 ± 0.4	1.24 ± 0.06	E2	$30^+ \rightarrow 28^+$	4
922	0.4 ± 0.3			$20^- \rightarrow 18^-$	$3 \rightarrow 1$
923	3.8 ± 0.6			$21^- \rightarrow 20^-$	$5 \rightarrow 1$
924.2	1.8 ± 0.3			$36^- \rightarrow 34^-$	3
926.1	1.52 ± 0.16			$21^- \rightarrow 19^-$	$3 \rightarrow 1$
926.7	14.2 ± 0.5	1.06 ± 0.05	E2	$32^+ \rightarrow 30^+$	2
928	3.6 ± 0.5			$32^- \rightarrow 30^-$	3
929	6 ± 0.5	1.13 ± 0.06	E2	$27^- \rightarrow 25^-$	3
931.3	3.1 ± 0.3	1.29 ± 0.02	E2	$31^- \rightarrow 29^-$	2
933.7	14.4 ± 0.6	1.20 ± 0.03	E2	$31^+ \rightarrow 29^+$	1
936	11.2 ± 0.5	1.59 ± 0.14	E2	$34^+ \rightarrow 32^+$	4
936.6	2.1 ± 0.3	1.25 ± 0.06	E2	$31^+ \rightarrow 29^+$	2
938	4.9 ± 0.3	1.16 ± 0.02	E2	$35^- \rightarrow 33^-$	5

Table 1 continued.

E_γ (keV)	I	R	Multipolarity	Assignment	Band
942.4	4.6 ± 0.3	1.24 ± 0.08	E2	$30^- \rightarrow 28^-$	3
945.3	5.4 ± 0.3	1.26 ± 0.10	E2	$36^+ \rightarrow 34^+$	2
949.3	3.31 ± 0.23	1.21 ± 0.09	E2	$42^+ \rightarrow 40^+$	9
950.1	2.5 ± 0.5	0.76 ± 0.10	M1/E2	$22^- \rightarrow 21^-$	$5 \rightarrow 1$
950.6	4.8 ± 0.6	0.73 ± 0.05	E1	$17^+ \rightarrow 16^-$	$2 \rightarrow 1$
956	1.3 ± 0.3	1.30 ± 0.1	E2	$38^- \rightarrow 36^-$	2
957	4 ± 0.4			$29^- \rightarrow 27^-$	3
957.2	2.2 ± 0.3			$37^+ \rightarrow 35^+$	3
957.3	3.6 ± 0.3	1.27 ± 0.05	E2	$41^- \rightarrow 39^-$	7
957.9	0.91 ± 0.12	1.37 ± 0.06	E2	$34^+ \rightarrow 32^+$	5
960.5	8.2 ± 0.4	1.17 ± 0.12	E2	$34^- \rightarrow 32^-$	6
963.4	8.5 ± 0.4	1.23 ± 0.03	E2	$33^+ \rightarrow 31^+$	2
964.1	9.3 ± 0.6			$18^+ \rightarrow 17^-$	$2 \rightarrow 1$
965	0.33 ± 0.18			$35 \rightarrow 33$	8
966.8	4 ± 0.3	1.27 ± 0.05	E2	$40^+ \rightarrow 38^+$	9
969	3.2 ± 0.4	1.2 ± 0.03	E2	$32^- \rightarrow 30^-$	1
969.8	4.5 ± 0.3			$32^+ \rightarrow 30^+$	4
970.1	2.9 ± 0.3	1.45 ± 0.06	E2	$36^- \rightarrow 34^-$	5
975.9	2.1 ± 0.3			$33^+ \rightarrow 31^+$	4
987.5	4.48 ± 0.23	1.28 ± 0.05	E2	$37^- \rightarrow 35^-$	5
993.4	0.98 ± 0.15			$36^+ \rightarrow 34^+$	4
993.5	1.07 ± 0.8			$35^+ \rightarrow 33^+$	7
994.2	1.33 ± 0.21			$40^+ \rightarrow 38^+$	$9 \rightarrow 2$
997.1	0.7 ± 0.3			$39^+ \rightarrow 37^+$	2
997.8	4.1 ± 0.4			$35^+ \rightarrow 33^+$	2
1000.4	2.7 ± 0.3	1.44 ± 0.16	E2	$40^- \rightarrow 38^-$	6
1004	2.8 ± 0.3	1.03 ± 0.10	E2	$46^+ \rightarrow 44^+$	9
1005.9	3.13 ± 0.2			$34^+ \rightarrow 32^+$	1
1006.8	1.7 ± 0.3			$33^- \rightarrow 31^-$	4
1008	2.8 ± 0.3			$38^- \rightarrow 36^-$	5
1014	3.2 ± 0.3			$38^+ \rightarrow 36^+$	2
1027.7	1.45 ± 0.22			$42^- \rightarrow 40^-$	6
1028.9	0.56 ± 0.1			$36^+ \rightarrow 34^+$	7
1029	0.19 ± 0.16			$37 \rightarrow 35$	8
1031	2.5 ± 0.13			$43^- \rightarrow 41^-$	5
1034.5	1.1 ± 0.3			$38^- \rightarrow 36^-$	6
1035	1.7 ± 0.3			$34^- \rightarrow 32^-$	1
1035.3	1.32 ± 0.24			$43^+ \rightarrow 41^+$	9

Table 1 continued.

E_γ (keV)	I	R	Multipolarity	Assignment	Band
1050.9	5.7 ± 0.4	1.17 ± 0.08	E2	$36^- \rightarrow 34^-$	6
1070.5	0.53 ± 0.07			$37^+ \rightarrow 35^+$	7
1073.1	1.83 ± 0.1			$45^+ \rightarrow 43^+$	9
1077.7	1.69 ± 0.23			$35^- \rightarrow 33^-$	1
1094.4	4 ± 0.3	1.58 ± 0.11	E2	$32^+ \rightarrow 30^+$	$9 \rightarrow 2$
1098.1	1.66 ± 0.22	1.32 ± 0.13	E2	$42^+ \rightarrow 40^+$	9
1100.9	1.35 ± 0.22			$36^- \rightarrow 34^-$	1
1114.6	0.95 ± 0.17			$41^+ \rightarrow 39^+$	2
1116	0.61 ± 0.09			$38^+ \rightarrow 36^+$	7
1127.8	2.41 ± 0.19	1.16 ± 0.17	E2	$44^+ \rightarrow 42^+$	9
1142	0.06 ± 0.06			$39^+ \rightarrow 37^+$	7
1145.9	0.76 ± 0.18			$37^- \rightarrow 35^-$	1
1165.7	0.34 ± 0.18			$38^- \rightarrow 36^-$	1
1177.5	1.3 ± 0.3			$40^+ \rightarrow 38^+$	9
1180	1 ± 0.3	1.03 ± 0.10	E2	$46^+ \rightarrow 44^+$	9
1187.3	6.8 ± 0.4	1.31 ± 0.06	E2	$38^+ \rightarrow 36^+$	9
1212.8	0.76 ± 0.18			$39^- \rightarrow 37^-$	1
1224.7	0.53 ± 0.17			$40^- \rightarrow 38^-$	1
1234.1	1.59 ± 0.18			$44^+ \rightarrow 43^+$	9
1251.5	0.98 ± 0.09			$47^+ \rightarrow 45^+$	9
1265	0.53 ± 0.03			$24^- \rightarrow 22^-$	$5 \rightarrow 1$
1277.4	0.56 ± 0.14			$42^- \rightarrow 40^-$	1
1310	1.75 ± 0.18	1.34 ± 0.31	E2	$42^+ \rightarrow 40^+$	9
1345.5	0.43 ± 0.16			$22^- \rightarrow 20^-$	$5 \rightarrow 1$
1359.1	1 ± 0.16			$45^+ \rightarrow 43^+$	9
1376	1.31 ± 0.19			$41^+ \rightarrow 39^+$	9
1397.1	0.76 ± 0.17			$43^+ \rightarrow 41^+$	9
1488.4	3.75 ± 0.16	1.07 ± 0.10	E2	$44^+ \rightarrow 42^+$	9
1501	0.95 ± 0.16			$43^+ \rightarrow 41^+$	9
1553	0.56 ± 0.13			$43^+ \rightarrow 41^+$	9
1744.8	1.9 ± 0.11			$43^+ \rightarrow 41^+$	9
1859	0.4 ± 0.47			$44^+ \rightarrow 41^+$	9
1891	0.06 ± 0.06			$45^+ \rightarrow 43^+$	9

Bibliography

[1] D. M. Cullen *et al. Phys. Rev. C*, 57(5), 1998. ii, xii, 70, 81, 90, 101

[2] National Nuclear Data Center, http://www.nndc.bnl.gov/, Accessed: 2014. ix, 3

[3] X. Wang. Properties of triaxial strongly deformed structures at ultra-high spin in light rare-earth nuclei: Collectivity beyond band termination in ^{157}Ho. *Proposal*, 2010. ix, 9

[4] G. Gilmore and J.D. Hemingway. *Practical Gamma-Ray Spectrometry*. John Wiley Sons, Inc., 1995. ix, 11, 13

[5] G. F. Knoll. *Radiation Detection and Measurement*. John Wiley Sons, Inc, 2000. ix, 12, 13, 16, 23, 24

[6] Soo Hyun Byun. Radioisotopes and Radiation Methodology: Lecture notes, https://www.science.mcmaster.ca/medphys/images/files/courses/4r06/note8.pdf, 2014. x, 21, 27

[7] D. Campbell. Phd Thesis. 2004. x, 22

[8] M. A. Riley *et al.* Gammasphere Online Booklet Homepages, Florida State University Physics Department, http://nucalf.physics.fsu.edu/ riley/gamma, 2014. x, 25

[9] J. Rees. Phd Thesis. 2013. xi, xviii, 29, 40, 68, 90, 123

[10] A. Aguilar. Phd Thesis. 2008. xi, 43

BIBLIOGRAPHY

[11] A. T. Semple. Phd Thesis. 1995. xi, 50

[12] Nilsson Diagrams, http://ie.lbl.gov/toipdf/nilsson.pdf, Accessed: 2014. xi, 51, 52

[13] K Heyde. *Basic Ideas and Concepts in Nuclear Physics*. Institute of Physics publishing, 1999. xi, 54

[14] Richard. F. Casten. *Nuclear Structure from a Simple Perspective, 2nd edition*. Oxford Science Publications, 2000. xii, 39, 44, 49, 54, 56, 61

[15] E. S. Paul *et al. Phys. Rev. Lett.*, 98(012501), 2007. xii, 67

[16] H. Gascon *et al. Nucl. Phys. A*, 513(344), 1990. xvi, 100

[17] D. C. Radford. *Nucl. Phys. A*, 545(665), 1992. xviii, 91, 103, 117, 119, 120, 123

[18] S. J. Gale *et al. J. Phys. G: Nucl. Part. Phys.*, 21(193), 1995. xviii, 123

[19] J. Dalton. On the absorption of gases by water and other liquids. *Memoirs of the Literary and Philosophical Society of Manchester*, 129(312), 1932. 1

[20] Aps news, http://www.aps.org/publications/apsnews/200803/physicshistory.cfm, Accessed: 2014. 1

[21] E. Rutherford. *Philosophical Magazine*, 21, 1911. 1

[22] J. Chadwick. *Nature*, 1:271–287, 1805. 1

[23] H. Ejiri and M. J. A. de Voigt. *Gamma-Ray and Electron Spectroscopy in Nuclear Physics*. Oxford University Press, 1989. 7

[24] A. Gavron *et al. Phys. Rev. C*, 21(1), 1980. 8

[25] John Lilley. *Nuclear Physics: Principles and Applications*. John Wiley Sons, Inc, 2001. 11

[26] Charles Kittel. *Introduction to Solid State Physics, 8^{th} edition*. John Wiley Sons, Inc, 2005. 16, 18

[27] J. Eberth, J. Simpson *et al.* *Progress in Particle and Nuclear Physics*, 60:283–337, 2008. 19, 26

[28] O. Klein *et al.* *Zeitschrift fr Physik*, 52:853–868, 1929. 24

[29] D. C. Radford. *Nucl. Instrum. and Methods Phys. Res. A*, 361(297), 1995. 29, 68

[30] D. C. Radford *et al.* *Proceedings of the Nuclear Structure 98 Conference, Gatlinburg, 1998, edited by C. Baktash (American Institute of Physics*, CP481:570, 1999. 29

[31] J. Cresswell. *Event Format [Sorting + Storage]*, EDOC073, 2001. 31

[32] J. Cresswell and J. Sampson. *MTsort Language*, EDOC033, 2009. 31

[33] E. S. Paul. Angular Correlation Analysis with Eurogam ii, http://ns.ph.liv.ac.uk/ esp/nuclear/eg2dco.ps, 1995. 31

[34] G. Gamow. *Proceedings of the Royal Society of London*, 126:632, 1930. 37

[35] C. F. von Weizsacker. *Zeitschrift für Physik A Hadrons and Nuclei*, 96:431–458, 1935. 37

[36] M. G. Mayer et al. *Phys. Rev.*, 75(1969), 1949. 42

[37] O. Haxel *et al.* *Phys. Rev.*, 75(1766), 1949. 42

[38] R. D. Woods, D.S. Saxon *et al.* *Physical Review*, 95:577–578, 1954. 44

[39] Jean-Louis Basdevant. *Fundamentals In Nuclear Physics.* Springer, 2004. 44

[40] A. Bohr and B.R. Mottelson. *Nuclear Structure, Vol. II.* World Scientific Publishing Co. Pte. Ltd, 1975. 45

[41] G. Andersson *et al.* *Nucl. Phys. A*, 268(205), 1976. 45

[42] S. G. Nilsson. *K. Dan Vidensk. Selsk. Mat. Fys. Medd.*, 29(16), 1955. 47

[43] Nilsson and Ragnarrson. *Shapes and Shells in Nuclear Structure.* Cambridge of University press, 2005. 49, 66

[44] W. Nazarewicz *et al. Nucl. Phys. A*, 435(397), 1985. 53

[45] S. Cwiok *et al. Comp. Phys. Comm.*, 46(379), 1987. 53

[46] J. Bardeen *et al. Phys. Rev.*, 108:11751204, 1957. 57

[47] A. Bohr *et al. Phys. Rev.*, 110:936938, 1958. 57

[48] S. Frauendorf and F. R. May *et al. Phys. Lett. B.*, 125(245), 1983. 61

[49] S. M. Harris *et al. Phys. Rev.*, 138(B509), 1965. 61

[50] J. Simpson *et al. J. Phys. G. Nucl. Phys.*, 12:L64–L74, 1986. 61

[51] R. Bengtsson, S. Frauendorf. *Nucl. Phys. A*, 327:139–171, 1979. 62

[52] F. Dönau and S. Frauendorf *et al. Nucl. Phys. A*, 471(469), 1987. 64

[53] I. Ragnarsson *et al. Physica Scripta*, 34:651–668, 1986. 65

[54] D. J. Hartley emphet al. *Phys. Rev.C*, 59(1171), 1999. 90, 95

[55] M. A. Riley *et al. Phys. Rev. C*, 39(1), 1989. 90, 95

[56] S. André *et al. Z. Phys. A*, 332:233–234, 1989. 90

[57] R. Vlastou *et al. Nucl. Phys. A*, 580:133–155, 1994. 90, 117

[58] A. O. Evans *et al. Phys. Rev.C*, 73(064303), 2006. 90

[59] M. A. Riley *et al. Nucl. Phys. A*, 486:456–492, 1988. 91, 92

[60] J. Simpson *et al. J. Phys. G*, 12(L67), 1986. 92

[61] Jingbin. Lu *et al. Phys. Rev.C*, 59(6), 1999. 95, 110, 111, 117, 118

[62] S. André *et al. Z. Phys. A*, 333(247), 1989. 95, 96, 110, 111

[63] M. A. Riley *et al. Phys. Lett.*, 135B(4), 1984. 95, 103

[64] C. H. Yu *et al.* Study of high spin states in odd-odd ^{156,158}ho. *Proceedings of the Workshop on Gammasphere Physics, edited by M.A. Deleplanque, I.Y. Lee, and A.O. Macchiavelli (World Scientific, Singapore*, 1996. 96, 110

[65] E. S. Paul *et al. J. Phys. G. Nucl.*, 17:605–617, 1991. 97

[66] J. Simpson *et al. Phys. Rev. Lett.*, 54(1132), 1985. 103

[67] J. M. Espino *et al. Nucl.Phys. A*, 640:163–195, 1998. 110

[68] P. Bringel *et al. Phys.Rev. C*, 75(044306), 2007. 110

[69] E. S. Paul *et al. Phys. Rev.C*, 80(054312), 2009. 113

[70] J.C. Waddington. *Scientific/technical report 147, University of Bergen*, 1984. 117